ROCK1 orchestrates B cell differentiation in response to PAMPs and heme by controlling the heme-regulated proteins Bach2 and HRI

Juan Rivera-Correa (riveracorreaj@HSS.EDU)
Hospital for Special Surgery https://orcid.org/0000-0003-4822-0005
Sanjay Gupta
Hospital for Special Surgery
Edd Ricker
Hospital for Special Surgery
Danny Flores-Castro
Hospital for Special Surgery
Daniel Jenkins
Hospital for Special Surgery
Stephen Vulcano
Hospital for Special Surgery
Tania Pannellini
Hospital for Special Surgery
Matthew Miele
Memorial Sloan Kettering Cancer Center
Zhuoning Li
Memorial Sloan Kettering Cancer Center
Nahuel Zamponi
Weill Cornell Medicine
Young Kim
Beth Israel Deaconess Medical Center
Eugenia Giannopoulou
Rosensweig Genomics Research Center
Leandro Cerchietti
Cornell University https://orcid.org/0000-0003-0608-1350
Alessandra Pernis
Hospital for Special Surgery https://orcid.org/0000-0001-8259-1446

Article

Keywords:

Posted Date: July 13th, 2023

DOI: https://doi.org/10.21203/rs.3.rs-3120870/v1

Additional Declarations: There is **NO** Competing Interest.

ROCK1 orchestrates B cell differentiation in response to PAMPs and heme by controlling the heme-regulated proteins Bach2 and HRI

Juan Rivera-Correa[1,2], Sanjay Gupta[1*], Edd Ricker[1*], Danny Flores-Castro[1], Daniel Jenkins[1], Stephen Vulcano[1], Tania Pannellini[3], Matthew Miele[4], Zhuoning Li[4], Nahuel Zamponi[5], Young-Bum Kim[6], Eugenia Giannopoulou[2,7], Leandro Cerchietti[5], and Alessandra B. Pernis[1,7,8]

[1]Autoimmunity and Inflammation Program, Hospital for Special Surgery, New York, NY, USA
[2]Biological Sciences Department, New York City College of Technology, City University of New York, Brooklyn, NY, United States
[3]Research Division and Precision Medicine Laboratory, Hospital for Special Surgery, New York, NY, USA
[4]Microchemistry & Proteomics core at Memorial Sloan Kettering Cancer Center
[5]Hematology and Oncology Division, Weill Cornell Medicine, New York, NY, USA.
[6]Beth Israel Deaconess Medical Center, Boston, MA
[7]David Z. Rosensweig Genomics Research Center, Hospital for Special Surgery, New York, NY, USA
[8]Department of Medicine, Weill Cornell Medicine, New York, NY, USA
* Authors contributed equally

Correspondence:
Alessandra B. Pernis
Autoimmunity and Inflammation Program, Hospital for Special Surgery, 535 East 70th Street, New York, NY 10021, USA. Tel: 212-206-1612. E-mail: pernisa@hss.edu

ABSTRACT

Protective humoral responses require that B cells successfully complete their differentiation programs even when exposed to hostile environments generated during severe infections, like the massive hemolysis triggered by malaria. The mechanisms utilized by differentiating B cells to withstand damaging conditions replete in PAMPs and DAMPs are poorly understood. Here we demonstrate that the serine-threonine kinase ROCK1 enables B cells to execute their differentiation programs upon exposure to PAMPs and high levels of heme, a critical DAMP, by controlling two key heme-regulated molecules, Bach2 and HRI. ROCK1 restrains plasma cell differentiation by phosphorylating Bach2. As B cells differentiate in the presence of PAMPs and heme, furthermore, ROCK1 limits the proinflammatory potential of B cells and restrains mTORC1 activity by controlling the assembly of multimolecular complexes that contain the adaptor p62, raptor, ripoptosome components, and molecules involved in RNA metabolism and proteostasis. ROCK1 regulates formation of these complexes by controlling the interplay between HSPs and the stress kinase HRI. Thus, ROCK1 helps B cells cope with intense pathogen-driven destruction by coordinating the activity and localization of key molecules that mediate cell-fate decisions, effector functions, and RNA and protein homeostasis. These ROCK1-dependent mechanisms may be widely employed by cells to handle severe environmental stresses and these findings may be broadly relevant for infections, vaccine development, and immune-mediated diseases marked by chronic tissue damage like autoimmune disorders.

INTRODUCTION

Precise orchestration of B cell differentiation is critical for protective immunity against pathogens [1, 2]. After repositioning to the T-B cell border, activated B cells can either migrate to extrafollicular (EF) areas and differentiate into short-lived plasmablasts (PB) or to the follicle where they form germinal centers (GC) eventually becoming high-affinity long-lived plasma cells (PC) or memory B cells (MBC). B cells differentiating via the EF route have recently been shown to include a distinctive B cell subset that expresses CD11c and/or T-bet, which has been alternatively termed Age-associated B-cells (ABCs), DN2 B cells, or, atypical memory B cells (atMBCs) [3, 4]. Disrupting the differentiation routes of activated B cells is a well-known strategy employed by pathogens to evade immune defenses as observed in *Plasmodium*-mediated malaria infections, which are accompanied by a complex array of disturbances ranging from exuberant polyclonal PB responses occurring at the expense of GC formation to enhanced accumulation of atMBCs [5, 6]. These alterations result in impaired long-lasting immunity allowing for repeated infections and representing a major challenge for the development of effective vaccines.

Pathogens employ several means to alter B-cell differentiation including leveraging the complex inflammatory environment elicited during severe infections to influence the decision-making of B cells ultimately affecting the establishment of protective immunity. Amongst the environmental stressors that can be faced by B cells are large amounts of free extracellular heme, a critical DAMP released during the hemolysis triggered by *Plasmodium* parasites and other pathogens. Interestingly, physiologic levels of heme have recently emerged as an important factor in the regulation of B cell differentiation [7, 8]. Critical to this role is the ability of heme to bind to and promote the degradation of Bach2, a guardian transcription factor that guides the cell-fate choices of activated B cells by controlling crucial gene regulatory networks (GRN) [9]. Bach2 drives GC formation and memory B-cell responses while preventing premature PC differentiation by repressing Blimp1 expression in cooperation with Bcl6. Besides heme binding, Bach2 is also regulated by PI3K/AKT and mTORC1, which phosphorylate Bach2 promoting its cytoplasmic accumulation and degradation [10]. The importance of tight control of Bach2 protein levels has been highlighted by the finding that mutations in human Bach2 promoting its instability result in a syndrome characterized by immunoglobulin deficiency and autoimmunity [11].

In addition to changes in Bach2-regulated GRNs, terminal differentiation of activated B cells also requires the coordinated execution of pathways aimed at handling the increased metabolic requirements and high rate of protein synthesis needed for robust and durable antibody secretion [12]. Implementation of this program has recently been shown to occur in distinct phases whereby an XBP1-independent “anticipatory” unfolded protein response (UPR) begins in activated B cells

and is followed by the classical IRE1α-XBP1-dependent UPR during the early stages of PC differentiation [13]. The "anticipatory" UPR is controlled by mTORC1 whose activity needs to be downregulated in PCs since persistent mTORC1 activation, as observed in the case of PI3Kδ gain of function mutations, results in impaired PC survival [13, 14]. In addition to PI3K, mTORC1 activation also requires the presence of amino acids, which enables the recruitment of mTORC1 to the lysosomes [15]. Repositioning of mTORC1 to the lysosome normally depends on the Rag-ragulator complex but can also occur via an alternative docking system that relies on SQSTM1/p62 (hereafter termed p62), an adaptor that binds raptor and positions mTOR near TRAF6 resulting in mTOR activation via K63-linked polyubiquitination [16, 17]. Recruitment and activation of mTORC1 by p62 is facilitated by the multidomain structure of p62, a feature that enables this protein to function as a central signaling hub positioned at the intersection of pathways regulating proteostasis, autophagy, and inflammation [18, 19]. Despite the pivotal role of p62 in coordinating stress responses, little is known about its involvement in B cell differentiation.

Severe pathogens often manipulate host defenses by targeting RhoA GTPases, which are molecular switches whose disarming in innate cells leads to inflammasome activation due to the inhibition of their downstream effectors, the PKN1/2 kinases [20, 21]. In addition to PKN1/2, RhoA signaling activates another key pair of serine-threonine kinases, ROCK1 and ROCK2, which are well-known controllers of cytoskeletal dynamics [22]. While intensely investigated in the non-hematopoietic system [23, 24, 25], only few studies, mostly focused on ROCK2, have assessed their role in B cells. In this compartment, ROCK2 is activated in response to adaptive signals such as the engagement of CD40 and regulates the proper positioning and cholesterol biosynthesis of GC B cells as well as PC differentiation [26]. These effects have been linked to the ability of ROCK2 to phosphorylate either IRF8 or IRF4 depending on the stage of B cell differentiation [26, 27]. While ROCK1 and ROCK2 share a highly homologous N-terminal kinase domain, they exhibit a lower degree of similarity in the remainder of the molecule and are encoded by different genes suggesting the existence of isoform-specific functions. Whether ROCK1 helps to coordinate B cell activation and differentiation is, however, unknown.

Here, we have employed a genetic approach coupled with transcriptomic, phospho-proteomic, and biochemical strategies to dissect the role of B-cell ROCK1 in humoral responses. Subjecting mice lacking B-cell ROCK1 to a malaria infection model and *in-vitro* stimulations reveals a unique role for ROCK1 in controlling B cell fate decisions when exposed to complex inflammatory environments. ROCK1 prevents premature PC differentiation when B cells are activated in the presence of both PAMPs and heme. B-cell ROCK1 is furthermore required to limit their acquisition

of a proinflammatory profile and to coordinate cell cycle pathways, mTORC1 activity, and the proper execution of stress responses. These effects are mediated by regulating the formation of p62 complexes enriched in mTORC1, PLK1, TBK1, and the RHIM-containing proteins, ZBP1, RIPK1, and RIPK3. Remarkably, these complexes also accumulate TDP-43, SOD1, and *C9orf72*, whose variants are known to be linked to neurodegenerative proteinopathies like Amyotrophic Lateral Sclerosis (ALS) [18]. ROCK1 regulates these processes by controlling the activity and stability of two key heme-regulated molecules, the transcription factor Bach2 and the eIF2α stress kinase HRI. These studies thus uncover a surprising role for ROCK1 in the coordination and implementation of pathways that enable B cells to efficiently cope with severe damaging conditions, maintain proteostasis, and navigate critical choices between proliferation, differentiation, and inflammation to establish durable humoral responses.

RESULTS

B-cell ROCK1 promotes GC responses and PC formation

Since ROCK1 and ROCK2 are both expressed in B cells, we employed a genetic approach to specifically investigate the role of B-cell ROCK1 in humoral responses. To this end, we generated CD23-Cre.*Rock1*$^{flox/flox}$ mice (termed CD23-*Rock1*) and compared them to *Rock1*$^{flox/flox}$ (WT) mice. B cells from CD23-*Rock1* mice efficiently deleted ROCK1 and *in vitro* kinase assays (IVKs) indicated that there was no compensatory increase in ROCK2 activity (Suppl. Fig 1A-D). CD23-*Rock1* mice displayed normal B cell populations in the BM and spleen at baseline except for a small decrease in marginal zone B (MZB) cells (Suppl. Fig. 1E-F). We initially examined the contribution of ROCK1 to T-cell dependent (TD) humoral responses. Compared to WT mice, both GC B cells and PB/PCs were decreased in CD23-*Rock1* mice post immunization with a TD antigen, NP-CGG (Suppl. Fig. 1G-H). To further confirm these results, we also generated *Rock1*$^{flox/flox}$ mice expressing Cγ1-*Cre* (termed Cγ1-*Rock1* mice) to induce deletion during the early stages of GC B cell differentiation. As we had observed in Cγ1-*Rock2* mice, immunization of Cγ1-*Rock1* mice with NP-CGG resulted in decreased total and antigen-specific GC B cells (Fig. 1A-D). Unlike mice lacking B-cell ROCK2 [26], however, the ratio of dark zone to light zone (DZ/LZ) GC B cells was not affected by the absence of ROCK1 (Suppl. Fig. 1I). Cγ1-*Rock1* mice also exhibited fewer total PB/PCs, decreased numbers of total and NP-specific IgG-producing ASCs in spleens and BM, and lower titers of NP-specific antibodies, although the ratio of high-affinity to total NP-specific antibodies was unchanged (Fig. 1E-G, Suppl. Fig. 1J). To assess whether ROCK1 is necessary for somatic hypermutation (SHM), we sorted GC B cells from immunized WT or Cγ1-*Rock1* mice and sequenced a portion of the JH4 intron of the heavy chain variable region. No significant differences in the mutation rate were observed between WT and Cγ1-*Rock1* GC B

cells (Fig 1H-I) suggesting that ROCK1 is not required for SHM. Lack of B-cell ROCK1 furthermore did not affect the T_{FH}/T_{FR} ratio or the frequencies of cytokine producing T-cells (Suppl. Fig. 1K-L). Taken all together, these data thus support the notion that, similarly to ROCK2 [26], B cell-ROCK1 functions in a cell-intrinsic manner to regulate optimal GC and PB/PC formation after immunization.

B-cell ROCK1 inhibits the acquisition of an inflammatory profile by GC B cells

To gain insights into the mechanisms employed by ROCK1 to control GC formation, we next sorted GC B cells from immunized WT and CD23-*Rock1* mice and employed bulk RNA-Seq to compare their transcriptomes. Sorted GC B cells from WT and CD23-*Rock1* mice expressed similar levels of key GC markers (Suppl. Fig. 2A). RNA-Seq analysis revealed 88 differentially expressed genes (DEGs) ($p<0.01$, LFC>0.58), with 3 downregulated genes in addition to ROCK1 and 85 upregulated genes in CD23-*Rock1* compared to WT GC B cells (Fig. 2A). Similar to the findings in CD23-*Rock2* GC B-cells [26], gene set enrichment analysis (GSEA) revealed that the only downregulated pathway (FDR $Q < 0.25$) in CD23-*Rock1* GC B cells was cholesterol biosynthesis (Fig. 2B-C) indicating that both ROCK kinases participate in the control of this critical metabolic pathway in GC B cells.

In contrast to the selective downregulation of only one major pathway, lack of ROCK1 led to the upregulation of several gene sets in GC B cells (Fig. 2D). Some of these gene sets, such as HALLMARK-Epithelial Mesenchymal Transition, were related to adhesion and polarity, consistent with the known cytoskeletal role of the ROCK kinases (Fig 2D-E). p53 signaling pathways were also upregulated in CD23-*Rock1* GC B cells and included classic p53 targets like Cdkn1a (Fig. 2D, 2F-G). Notably, CD23-*Rock1* GC B cells also upregulated several DEGs related to inflammation (e.g. *Ccl5*, *Ccl22*, *Csf1*, *Il18r1*, and *Il18rap*) and a number of pro-inflammatory gene sets including HALLMARK-TNFα signaling via NFκB and HALLMARK-Inflammatory response (Fig. 2D, Fig. 2H-I, Suppl. Fig. 2B). A comparison of the DEGs in CD23-*Rock1* GC B cells with those in CD23-*Rock2* GC B cells [26] furthermore revealed that whereas ROCK2 preferentially repressed genes related to GC B cell positioning, such as *Ccr6* and *Ebi2* (G Protein-Coupled Receptor 183 (*GPR183*)), ROCK1 primarily repressed the expression of proinflammatory cytokine receptors such as *Il18r1* and *Il18rap*. Thus, surprisingly, ROCK1 limits the proinflammatory profile of GC B cells.

B-cell ROCK1 restrains systemic inflammation and pathology during malaria infection

The unexpected gene expression profile of ROCK1-deficient B cells in response to immunization led us to assess the role of B-cell ROCK1 in a complex infectious setting. We opted to employ *Plasmodium yoelii 17XNL (P. yoelii),* a non-lethal self-healing malaria infection model, which, in C57BL/6 mice, leads to RBC destruction and hemolysis, severe anemia, and parasitemia mimicking features observed in malaria-naïve individuals infected with human *Plasmodium* species [28, 29, 30]. Notably, we found that WT B cells increase ROCK1, but not ROCK2, activation as a physiologic response to this parasite at Day 9 post-infection (pi) (Fig. 3A, Suppl. Fig. 3A). We next infected WT and CD23-*Rock1* mice with *P. yoelii* and performed a detailed analysis at acute Day 9 pi and at late Day 21 pi when mice are normally in a convalescent phase. While parasitemia levels were similar at acute Day 9, lack of B-cell ROCK1 impaired resolution of the infection at late Day 21 (Fig. 3B). Flow cytometry of splenic populations demonstrated that total B cells decreased to a greater extent in CD23-*Rock1* than in WT mice at Day 9 pi and did not recover as readily at Day 21 pi and that GC B cells were significantly reduced at both time points (Fig. 3C-E, Suppl. Fig. 3B-C). Expansion of ABCs was primarily observed at Day 21 pi and was unaffected by the lack of B-cell ROCK1, resulting in a relative increase in ABCs over GC B cells at this late time point (Fig. 3F-G, Suppl. Fig. 3D). Only minor decreases in total $CD4^+$ and follicular T helper (T_{fh}) cells were observed (Suppl. Fig. 3F-H). Interestingly, despite a comparable expansion of PB/PCs at Day 9 pi in WT and CD23-*Rock1* mice, lack of B-cell ROCK1 markedly impacted the robust polyclonal antibody responses known to accompany this infection [29, 30], with decreases in total IgG1 and IgG2c observed at both Day 9 and Day 21, and in total IgM at Day 21 (Fig. 3H-I, Suppl. Fig. 3E). Absence of B-cell ROCK1 also resulted in lower titers of anti-malaria IgG1 antibodies but not of anti-malaria IgG2c antibodies, an isotype classically produced by ABCs (Fig. 3J). CD23-*Rock1* mice also produced higher levels of the potentially self-reactive anti-phosphatidylserine (PS) and anti-cardiolipin antibodies (Fig. 3K). Thus, B-cell ROCK1 is important for infection resolution and its absence alters B cell differentiation and antibody production during *P. yoelii* infection.

Given the increased expression of inflammatory mediators like C*cl5* and *Ccl22* in CD23-*Rock1* B cells upon immunization, we also assessed the production of these chemokines. Serum levels of CCL5 and CCL22 were significantly higher in CD23-*Rock1* than in WT mice at both Day 9 and Day 21 pi (Fig. 3L). The development of a heightened inflammatory environment and more severe pathogenesis in CD23-*Rock1* mice was also supported by increases in IFN-γ producing $CD4^+$ T-cells, persistent anemia, thrombocytopenia, increased spleen weight, and higher red pulp erythropoiesis at Day 21 pi and required early euthanasia (Fig. 3M, Suppl. 3I-J). A histological analysis demonstrated that CD23-*Rock1* mice also displayed increased hepatonecrosis and sinusoidal enlargement in the liver and increased tubulointerstitial damage in the kidneys despite

similar levels of malaria pigment (hemozoin) and parasitized RBC deposition (Fig. 3N-O and Suppl. Fig, 3K-L). Thus, B-cell ROCK1 is important in restraining systemic inflammation and limiting pathological responses during *P. yoelii* malaria.

Rock1 regulates the transcriptional profile of activated B cells and PB/PCs during malaria infection

To further investigate how the absence of ROCK1 during malaria infection could lead to such distinctive B cell abnormalities, we employed a recently described strategy [29] to sort B cells representing distinct stages of differentiation from day 9 *P.yoelii*-infected WT and CD23-*Rock1* mice (Fig. 4A) and performed bulk RNA-seq. In addition to naïve and activated B cells, the robust PB response observed in this infection also enabled us to examine the role of ROCK1 in this population. B cell subsets from WT and CD23-*Rock1* mice exhibited similar proliferative capabilities and key markers (Suppl. Fig. 4A-B). Although only few DEGs ($p<0.01$, LFC>0.58) distinguished naïve B cell populations from WT and CD23-*Rock1* mice, GSEA demonstrated that absence of ROCK1 resulted in a significant upregulation (FDR $Q < 0.25$) of transcriptional signatures encompassing cytoskeletal processes, inflammatory responses, KRAS signaling, and heme metabolism (Fig. 4C-D). As B cells became activated, an increasing number of DEGs could be observed between CD23-*Rock1* and WT B cells and GSEA revealed that lack of ROCK1 again led to the upregulation of several signatures related to cytoskeletal processes, inflammatory responses, KRAS signaling pathways, and heme metabolism (Fig. 4E-G, Suppl. Fig. 4C). Absence of ROCK1 in activated B cells also resulted in an enrichment in cell cycle pathways related to mitotic spindle assembly and the G2/M checkpoint (Fig. 4F-G). Enrichment in these pathways as well as in E2F targets was also detected in PB/PCs lacking ROCK1 (Fig. 4J-K, Suppl. Fig. 4E). Only few downregulated pathways were observed in the absence of ROCK1. They were largely related to oxidative phosphorylation and translation and were primarily confined to activated B cells and PB/PCs (Fig. 4H, 4L, Suppl. Fig. 4D, F). Thus, in addition to the alterations in cytoskeletal and proinflammatory signatures, the complex inflammatory environment of *P. yoelii* malaria revealed that B-cell ROCK1 regulates pathways related to heme metabolism, cell cycle control, and programs important for coping with the increased metabolic and protein synthesis demands of PB/PCs.

ROCK1 regulates the heme-sensing transcription factor Bach2

The malaria infections had revealed an important role for ROCK1 in regulating the ability of B cells to respond to heme and upregulate a heme metabolism signature, a pathway recently recognized to be important in controlling B cell fate outcomes [7, 8]. This led us to explore whether ROCK1 could regulate Bach2, a heme-regulated transcription factor that not only controls key

heme metabolic enzymes like Hmox1 but also promotes the GC program and prevents premature PC differentiation by repressing Blimp1 expression [9]. To investigate this possibility, we set-up an *in vitro* system where we employed combinations of signals, which, in the setting of malaria infection, might influence the decision of activated B cells to differentiate into PCs at the expense of forming GCs. These included adaptive signals provided by αIgM and αCD40, as well as key cues released during the *P. yoelii* malaria infection, the CpG PAMP recognized by TLR9 and heme, the critical DAMP released during the hemolysis that the infection triggers. B cells purified from CD23-*Rock1* mice exhibited similar viability to WT B cells under all these conditions except for a slight increase in apoptosis when cultured with αIgM+αCD40+heme (Suppl. Fig. 5A-B). Stimulation with αIgM+αCD40 for 3 days, even in the presence of heme, did not upregulate Blimp1 expression in either WT or CD23-*Rock1* B cells (Fig. 5A). Compared to WT B cells, however, B cells lacking ROCK1 expressed higher levels of Blimp1 when CpG was added to the cultures and this effect was greatly augmented by the presence of heme (Fig. 5A). Upregulation of Blimp1 expression was not accompanied by significant changes in Bach2 transcript levels (Suppl. Fig. 5C). CD23-*Rock1* B cells, however, exhibited lower levels of Bach2 protein than WT B cells when stimulated with CpG+heme, an effect that was confirmed by adding cycloheximide to block new protein synthesis (Fig. 5B, Suppl. Fig. 5D). Thus, ROCK1 helps maintain adequate Bach2 protein levels and prevents accelerated PC differentiation when B cells differentiate in the presence of pathogen-associated cues like TLR9 ligands and DAMPs like heme.

Activation of B cells leads to the phosphorylation of Bach2 on several serine and threonine (S/T) residues many of which are located within its naturally disordered region (aa331-520) that is involved in heme binding and protein-protein interactions [10]. To assess whether ROCK1 could control Bach2 by directly phosphorylating it, we immunoprecipitated FLAG-tagged Bach2 and performed IVKs with constitutively active ROCK1 (CA-ROCK1). Incubation with CA-ROCK1 resulted in the phosphorylation of Bach2 as assessed by immunoblotting with a phosphoserine antibody (Fig. 5C). To confirm these findings, the immunoprecipitated *in vitro* phosphorylated Bach2 protein was subjected to mass spec analysis, which revealed that ROCK1 could phosphorylate Bach2 at two different sites: S376 located in the heme-binding domain just downstream of the first CP motif, and S718 just downstream of the bZIP region, which mediates heterodimer formation and DNA binding [10] (Fig. 5D). To assess the functional effects of the ROCK1-mediated phosphorylation of Bach2, we generated Bach2 mutants in which S376 and S718 were mutated to alanine either individually or in combination (Bach2A376, Bach2A718, and Bach2A376A718) and assessed their stability in 293T cells exposed to heme (Fig. 5E). Addition of heme in the presence of cycloheximide to block new protein synthesis did not affect the protein

levels of WT Bach2 or of the single mutants (Bach2A376 and Bach2A718) but resulted in decreased abundance of Bach2A376A718. Thus, phosphorylation of Bach2 by ROCK1 prevents its degradation in response to heme.

To further evaluate the effects of the ROCK1-mediated regulation of Bach2, we performed RNAseq on WT and CD23-*Rock1* B cells stimulated *in vitro* under the various conditions (Suppl Fig. 5E-H). When stimulated with a TLR9 ligand, particularly in the presence of heme, CD23-*Rock1* B cells demonstrated increased expression of markers associated with PC differentiation, in line with the strong effects exerted by the absence of ROCK1 on Bach2 stability and the robust Blimp1 upregulation observed under those conditions (Fig. 5F). Interestingly, lack of ROCK1, also affected the expression of genes normally inhibited by Bach2 such as HMOX1 and various DUSPs even when the TLR9 ligand was omitted from the cultures (Fig. 5G). A comparison with a recently published dataset [31] furthermore confirmed that, under these conditions, absence of B-cell ROCK1 resulted in an enrichment in Bach2 repressed targets (Fig. 5H). Given that one of the sites phosphorylated by ROCK1 is located near the bZIP region of Bach2, these data suggest that, in addition to controlling its stability, ROCK1 may also exert selective effects on the Bach2-controlled transcriptional program by regulating its DNA binding ability and/or protein-protein interactions and that the functional outcome of the ROCK1-mediated control of Bach2 can be influenced by the specific combination of signals to which B cells are exposed.

Absence of ROCK1 leads to dysregulated mTORC1-related signatures

In addition to affecting cell fate decisions, the lack of ROCK1 also leads B cells to exhibit an enhanced proinflammatory profile, an altered cell cycle program, and an inability to meet the heightened demands of vigorous antibody secretion, especially when faced with the stressful environment triggered by the *P.yoelii* malaria infection. Since these effects would not be expected if ROCK1 only controlled Bach2, we reasoned that the *in vitro* system, with its carefully controlled kinetics, could also provide insights into the mechanisms leading to these abnormalities. To identify additional ROCK1-regulated B cell pathways, we thus performed GSEA analysis on the RNAseq experiments performed on the *in vitro* stimulated WT and CD23-*Rock1* B cells. As had been observed *in vivo*, CD23-*Rock1* B cells upregulated pathways related to cytoskeletal processes and cell cycle control including pathways related to the G2/M checkpoint, E2F targets, and mitotic spindle (Fig. 6A-D). B cells lacking ROCK1 were furthermore enriched for inflammatory pathways like TNFα signaling via NFκB and upregulated the expression of immediate early genes like Fos, JunB, and EGR1 and of proinflammatory mediators like TNFα (Fig. 6A-E). In agreement with this profile, ROCK1-deficient B cells produced higher levels of

CCL5 compared to WT B cells (Fig. 6F). Thus, key features exhibited by ROCK1-deficient B cells upon *P. yoelii* infection, such as the cell cycle disturbances and the enhanced proinflammatory capabilities, were replicated under these *in vitro* stimulatory conditions. While some of these alterations could already be detected in cells stimulated with αIgM+αCD40 alone, presence of pathogen- and damage-associated cues, like TLR9 ligands and heme, greatly augmented several of these abnormalities.

Interestingly, the GSEA also revealed that, relative to WT B cells, absence of B-cell ROCK1 resulted in an enrichment in pathways related to mTORC1 signaling and the unfolded protein response (UPR). Upregulation of mTORC1 signaling in CD23-*Rock1* B cells was observed upon stimulation with αIgM+αCD40 alone but, surprisingly, also upon addition of a TLR9 ligand (Fig. 6G), although these cells were already exhibiting substantial PC differentiation, a stage during which mTORC1 activity should be waning. Given that mTORC1 controls a preparative UPR in activated B cells that precedes the classical UPR associated with PC differentiation [13], we employed GSEA to compare our dataset with signatures for the two distinct phases of this stress response to better assess how absence of ROCK1 might affect the relationship between mTORC1 and the UPR. CD23-*Rock1* B cells stimulated with αIgM and αCD40 alone showed a greater enrichment for the B-cell activating UPR signature than WT B cells but did not exhibit upregulation of a PC inductive signature (Fig. 6H-I). Addition of heme or a TLR9 ligand to the cultures resulted in the enrichment of both B-cell activating and PC-inductive UPR while only upregulation of a PC-inductive UPR was observed in CD23-*Rock1* B cells upon addition of both TLR9 ligands and heme consistent with the greatly accelerated PC differentiation of these cultures (Fig. 6H-I). These data thus suggest that absence of ROCK1 leads to dysregulated mTORC1 activity and predisposes activated B cells to inappropriately implement biochemical programs whose orderly execution is necessary for the transition to PCs.

Phospho-proteomic analysis reveals increased activity of mTORC1 and other major kinases in the absence of ROCK1

To better delineate how ROCK1 controls the biochemical state of B cells and guides their activation and differentiation, we next conducted a phospho-proteomic analysis. The initial experiments were performed with CD23-*Rock1* B cells stimulated with αIgM+αCD40. After harvesting, cells were subjected to pS/pT TMT and total proteome TMT and results analyzed by Proteome Discoverer. A total of 49 phosphorylated peptides were found to be significantly altered in CD23-*Rock1* B cells as compared to WT B cells (Fig. 7A). Phosphorylation of 4 peptides was significantly downregulated (Log2FC>1, p-val < 0.05) in the absence of ROCK1 (Fig. 7B). Two of

the downregulated phosphorylation sites were in two distinct regulatory subunits of myosin phosphatase (ppp1r12a=MYPT1 and ppp1r12c=MBS85), which are well-known ROCK substrates. Lack of ROCK1 also decreased the phosphorylation status of two different sites within AKAP13, an X-linked RhoA GEF [32], suggesting a potential feedback loop between ROCK1 and its activators. Interestingly, the phosphorylation site most significantly downregulated in the absence of ROCK1 was contained within the active site of tissue-nonspecific alkaline phosphatase (TNAP/ALPL) [33], which, in addition to its known role in phosphate metabolism, has been shown to possess anti-inflammatory properties [34]. In line with these findings, a PSEA analysis demonstrated enrichment in phosphatase regulator activity as the most downregulated pathway (log2FC>0.06) (Fig. 7C). Thus, B-cell ROCK1 phosphorylates key phosphatases, which include not only known targets involved in cytoskeletal dynamics like myosin phosphatase, but also novel targets like ALPL.

Surprisingly, absence of B-cell ROCK1 also resulted in significant increases in the phosphorylation of several peptides (Suppl. Fig. 7A). Most of the phosphorylated sites affected by the lack of ROCK1 were in well-known proteins like 53bp1, Hdac1, Numa1, TFEB, Trim28, 4EBP1, and p62. Employment of less stringent criteria (log2FC>0.6) revealed additional peptides whose phosphorylation status was upregulated in the absence of ROCK1 including TDP-43 (S292). Several of the targets were functionally connected as demonstrated by STRING analysis (Fig. 7D). PSEA pathway analysis ran against GO Molecular function, Biological Process and Cellular Component database and furthermore demonstrated enrichment for pathways involved in chromatin regulation, RNA handling, and translation (Fig. 7E). Consistent with these results, many of the processes coordinated by proteins whose phosphorylation is altered in CD23-*Rock1* B cells normally take place in the nucleus, spliceosome, and RNA processing structures like P-bodies (Suppl. Fig. 7B-C). Stimulation with a TLR9 ligand in addition to αIgM+αCD40 resulted in a smaller number of changes in the pS/pT TMT analysis (Suppl. Fig. 7D). Many of the peptides whose phosphorylation was significantly affected by the lack of ROCK1 upon TLR9 costimulation were similar to those detected in CD23-*Rock1* B cells activated with αIgM+αCD40 alone except for six proteins whose phosphorylation was significantly increased specifically in CpG-stimulated cells (Suppl. Fig. 7E). These hyperphosphorylated proteins included components of cytoplasmic granules and PML-nuclear bodies, the ubiquitin ligase Cbl, and aspartate carbamoyltransferase, a rate-limiting enzyme in de novo pyrimidine synthesis. Thus, the ROCK1-regulated phosphoproteome in B cells extends beyond the predicted involvement of this kinase in cytoskeletal dynamics and encompasses several proteins that regulate processes involved in DNA damage, RNA processing and handling, and translational regulation.

Given the unexpected increase in the phosphorylation of several targets in the absence of ROCK1, we employed Enrichr pathway analysis and KEA PTMsigDB to gain insights into the kinases that might phosphorylate these sites. The top kinase substrate interaction predicted by these algorithms implicated mTOR as the kinase most likely responsible for these phosphorylation events (Fig. 7F-G). This finding was corroborated by a survey of PhosphoSitePlus [35], which revealed that many of these phosphorylation events were occurring at sites, which had been previously identified in proteomic analyses linked to mTOR signaling and particularly to mTORC1 (Fig. 7H). Interestingly, some of the sites uncovered by this analysis had also been reported in phosphoproteomic studies of TBK1, RIPK3, and PLK1, kinases that play key roles in inflammatory responses and G2/M cell cycle progression (Fig. 7H). These results thus suggest that the dysregulated transcriptional profiles of B cells lacking ROCK1 is coupled with aberrant activity of mTORC1 and may also encompass effects on the activation of other key kinases.

ROCK1 limits formation of p62 complexes enriched in mTORC1 and ripoptosome components

The surprising finding that absence of ROCK1 might increase the activity of mTORC1 prompted us to investigate the mechanisms underlying this cross-talk by assessing key steps in this signaling cascade. In agreement with the phosphoproteomic analysis, lack of ROCK1 resulted in higher levels of phosphorylated 4E-BP1, a key downstream effector of mTORC1 [15] (Fig. 8A). Phosphorylation of S6 (S240/244), p70S6K (T389), and ULK1 (S757) was instead unchanged (Suppl. Fig. 8A-C) indicating that the increased mTORC1 activity detected in the absence of ROCK1 is restricted to a subset of targets. An analysis of upstream regulators of mTORC1 activation [15] demonstrated that phosphorylation of AKT (T308 or S473) and AMPK (T172) was similar in WT and CD23-*Rock1* B cells (Suppl. Fig. 8D-F) suggesting that ROCK1 does not affect mTORC1 activity by regulating growth factor-mediated or energy-dependent pathways. Activation of mTORC1 in response to nutrients requires its recruitment to the lysosomes, which can be mediated by the interaction of raptor with p62 and the subsequent activation of mTOR by TRAF6 [16, 17]. An assessment of this complex revealed that p62 did not associate with TRAF6 in WT B cells regardless of the stimulation conditions (Fig. 8B). In contrast, p62 strongly interacted with both raptor and TRAF6 in CD23-*Rock1* B cells upon costimulation with a TLR9 ligand ± heme (Fig. 8B). Under these conditions, furthermore, the immunoprecipitated p62 was phosphorylated at S349 (Fig. 8B), a site whose phosphorylation is mTORC1-dependent [18], indicating that the raptor–p62–TRAF6 complex formed under these conditions contains active mTORC1. As predicted, phosphorylation of p62 at S349 was furthermore accompanied by an increased ability

of p62 to interact with Keap1 (Fig. 8B). Thus, ROCK1 restrains the assembly of a p62-raptor-TRAF6 complex and fine-tunes mTORC1 activation.

p62 acts as a signaling hub coordinating the activity of several pathways via its multidomain structure [18, 19]. Importantly, p62 can interact with TBK1 and RIPK1, which, together with RIPK3 and ZBP1, are critical components of ripoptosome complexes involved in regulating TNFα signaling and inflammatory cell death in innate cells [36, 37]. In view of the enrichment in TNF-α NFκB signaling signatures in CD23-*Rock1* B cells and the increased phosphorylation of TBK1 and RIPK3 targets detected in the phospho-proteomic analysis, we thus investigated the presence of these molecules in the p62 precipitates. p62 strongly interacted with TBK1, RIPK1, RIPK3, and ZBP1 in CD23-*Rock1* B cells costimulated with a TLR9 agonist ± heme (Fig. 8C-D, Suppl. Fig. 8G-H). TBK1 in those p62 precipitates was furthermore phosphorylated at S172 suggesting that TBK1 in these complexes is active [37] (Fig. 8C). Although MLKL could not be reliably identified in the p62 complexes due to the overlap with the Ig heavy chain, no significant differences in its cleavage were observed between WT and CD23-*Rock1* B cells (Suppl. Fig. 8I). Furthermore, LDH levels in the supernatants of CD23-*Rock1* B cells were lower than in those of WT B cells (Suppl. Fig. 8J). Given that dysregulation in cell cycle and PLK1 targets could also be observed in CD23-*Rock1* B cells and that PLK1 can assemble in "mitotic ripoptosomes" with RIPK1 and RIPK3 [38, 39], we also assessed for the presence of this kinase and found that ROCK1 deficiency led to the accumulation of PLK1 in the p62 precipitates upon stimulation with a TLR9 agonist ± heme (Fig. 8E, Suppl Fig. 8 K). Interestingly, addition of heme resulted in the formation of high molecular weight p62 complexes as reported [40] but, by itself, was unable to recruit any of the molecules to p62 (Fig. 8B-F, Suppl. Fig. 8G-H, K). Addition of heme to the TLR9-L, however, altered the composition of the p62 aggregates formed in CD23-*Rock1* B cells as shown in the case of ZBP1 (Fig. 8B-E, Suppl. Fig. 8G-H, K). Thus, when B cells differentiate in the presence of pathogen-associated signals, ROCK1 limits the formation of p62 multimolecular complexes that contain major kinases and signaling components that control proliferation and inflammation.

p62 aggregates are a well-known feature of neurodegenerative disorders like ALS and, in these patients, p62 often colocalizes with other ALS-linked genes such as TDP-43, SOD1, and *C9orf72* [18]. Intriguingly, the phospho-proteomic analysis had suggested that the absence of ROCK1 could affect the phosphorylation of TDP-43 at S292, a site known to be phosphorylated in the brains of ALS patients, leading us to investigate the presence of TDP-43 and other key ALS targets in the p62 complexes formed in the absence of ROCK1. Both TDP-43 and SOD1 strongly interacted with p62 in CD23-*Rock1* B cells, a finding that was again primarily restricted to cells stimulated

with a TLR9 agonist ± heme (Fig. 8G, Suppl. Fig. 8L). Presence of *C9orf72* was also detected in the p62 precipitates and followed a pattern similar to that of TDP-43 and SOD1 (Fig. 8H, Suppl. Fig. 8M). Molecules known to be recruited to cytoplasmic granules and P-bodies under stress, such as DEF6 [41], as well as its homologue SWAP-70, could also be detected in the p62 complexes (Suppl. Fig. 8N). An assessment of autophagic flux as evaluated by formation of lipidated LC3 (LC3-II) furthermore did not reveal any substantial differences between WT and CD23-*Rock1* B cells (Fig. 8I). Thus, in the presence of pathogen-driven stressors, absence of ROCK1 leads to the formation of distinctive p62 complexes, which, in addition to major kinases, also contain several proteins involved in RNA metabolism, proteostasis, and oxidative stress, many of which have been linked to ALS pathogenesis.

ROCK1 controls the heme-regulated kinase HRI, a key sensor of stress and protein aggregation

The unexpected assembly of distinctive p62 complexes in CD23-*Rock1* B cells upon exposure to pathogen-driven stressors led us to investigate the mechanisms by which ROCK1 could regulate their formation. Since p62 is known to undergo phase separation and form condensates upon binding ubiquitin chains [42], we first investigated whether the p62 aggregates formed in CD23-*Rock1* B cells contained ubiquitinated proteins. Probing of p62 immunoprecipitates with an antibody that recognizes K63 ubiquitin chains revealed the presence of several K63-ubiquitinated proteins in p62 precipitates from CD23-*Rock1* B cells costimulated with TLR9-L±heme (Fig. 9A, Suppl. Fig. 9A). Given recent work demonstrating that the ER chaperone BiP (also known as HSPA5/GRP78) can accumulate in the cytoplasm under stress in the presence of foreign DNA and promote the oligomerization of p62 [43], we also probed the p62 aggregates formed in WT and CD23-*Rock1* B cells for BiP. Presence of BiP was strongly detected in the p62 complexes formed in CD23-*Rock1* B cells co-stimulated with TLR9-L±heme but not in CD23-*Rock1* B cells stimulated only with αIgM+αCD40 or in WT B cells (Fig. 9A, Suppl. Fig. 9A). Consistent with the ability of distinct heat shock proteins (HSPs) to extensively interact and assemble in higher-order structures that have been termed “epichaperomes” [44, 45], furthermore, the p62 aggregates in CD23-*Rock1* B cells co-stimulated with TLR9-L±heme also contained Hsp90 (Fig. 9A, Suppl. Fig. 9A). Thus, in the presence of pathogen-associated cues, absence of ROCK1 results in the formation of p62 complexes that contain ubiquitinated proteins and components like HSPs that can promote its oligomerization and phase separation.

Under homeostasis, the specialized UPR of PCs is primarily controlled by the IRE1α-XBP1 axis [12]. We, however, reasoned that exposure to pathogens and severe damaging conditions such as

high levels of extracellular heme may require differentiating B cells to employ additional machinery to handle the increased stress. EIF2AK1/HRI (hereafter termed HRI), one of the four eIF2α kinases, regulates the integrated stress response (ISR) in response to heme deprivation and several other stressors [46, 47]. In addition to its role in orchestrating the ISR, HRI has also been shown to regulate mTORC1 activity and to restrain the accumulation of protein aggregates [48, 49, 50]. We thus explored the possibility that ROCK1 might control HRI. Notably, HRI is known to interact with HSPs and dissociation of HRI from HSPs is critical for its role in proteostasis. We first investigated whether the presence of HSPs within the p62 aggregates in CD23-*Rock1* B cells was accompanied by aberrant recruitment of HRI to the p62 complexes. Immunoblotting of p62 precipitates with an HRI antibody indeed demonstrated that these complexes contained HRI only when CD23-*Rock1* B cells were stimulated under conditions that also resulted in the recruitment of HSPs (Fig. 9B, Suppl. Fig. 9B). Besides association with HSPs, HRI activity can be controlled by heme binding, which can inhibit the ability of HRI to engage the ISR [46, 47]. To examine whether ROCK1 could regulate the ability of B cells to activate the ISR upon exposure to heme, we thus assessed eIF2α phosphorylation and ATF4 expression (Fig. 9C-D). As compared to WT B cells, both the levels of peIF2α and the upregulation of ATF4 were markedly diminished in CD23-*Rock1* B cells stimulated with a TLR9 ligand and heme (Fig. 9C-D). The levels of the active/spliced form of XBP1 (XBP1s) were instead similar between WT and CD23-*Rock1* B cells (Suppl. Fig. 9C). Taken together, these results suggest that lack of B-cell ROCK1 leads to the inappropriate recruitment of HRI to p62 aggregates and modifies the ability of HRI to respond to heme and engage the ISR.

HRI undergoes extensive phosphorylation, which alters its intramolecular interactions and regulate its activity as well as its sensitivity to heme [51]. We thus explored the possibility that ROCK1 might directly regulate HRI and modulate its activity by phosphorylating it. To this end, we transfected FLAG-tagged HRI in 293T cells, immunoprecipitated it, and performed IVKs with constitutively active ROCK1 (CA-ROCK1). As shown in Fig. 9E, immunoblotting with a FLAG antibody revealed that incubation with CA-ROCK1 resulted in the appearance of a slower mobility form of HRI consistent with previous studies showing changes in HRI mobility upon its phosphorylation [51]. To further assess whether the ROCK1-mediated phosphorylation of HRI could affect its interaction with HSPs and response to heme, we transfected FLAG-tagged HRI in 293T cells, stimulated the cells in the presence or absence of heme, and assessed the ability of immunoprecipitated FLAG-tagged HRI to interact with HSP90 after performing IVKs with constitutively active ROCK1 (CA-ROCK1) (Fig. 9F). IVKs with CA-ROCK1 resulted in a marked decrease in the association of HRI with HSP90 in the presence of heme. A TMT mass spec

analysis performed on immunoprecipitated FLAG-tagged HRI in the presence or absence of CA-ROCK1 furthermore demonstrated decreased interaction of HRI with HSPs in the presence of CA-ROCK1 (Suppl. Fig. 9D). Consistent with these findings, addition of PU-H71, an HSP90 inhibitor that preferentially targets HSP90 incorporated in "epichaperome" complexes [45], decreased the dysregulated phosphorylation of 4EBP1 observed in the absence of ROCK1 (Fig. 9G). Thus, ROCK1 regulates the activity of HRI by controlling its interplay with HSPs and heme and enables differentiating B cells to engage the ISR in order to minimize the potentially damaging consequences of toxic levels of heme.

DISCUSSION

Development of protective humoral immunity to infectious challenges requires that B cells successfully execute their differentiation programs under a wide range of potentially damaging conditions. Here, we demonstrate that B-cell ROCK1 acts as a critical regulatory hub that controls the ability of B cells to implement molecular and biochemical programs necessary for their optimal activation and differentiation when faced with hostile conditions, such as the combination of PAMPs and high-levels of heme encountered during malaria infection. We show that, in these settings, B-cell ROCK1 plays a multifaceted role. ROCK1 not only ensures proper B cell differentiation but, unexpectedly, also restrains the proinflammatory capabilities of B cells and helps coordinate their stress responses. Notably, ROCK1 regulates these processes by directly modulating the activity and stability of two heme-regulated proteins that exert fundamental roles in cell-fate decisions and stress responses, Bach2 and HRI.

Together with our previous work [26, 27], the present study shows that both ROCK1 and ROCK2 can be activated in response to BCR and CD40 engagement and that, in immunization models, the two ROCK isoforms partially complement each other in promoting cholesterol biosynthesis and GC formation. The *P. yoelii* malaria model, however, indicates that presence of pathogen-driven signals can skew the activation of the two ROCK isoforms. During this infection, ROCK1 becomes the primary ROCK isoform activated in B cells preventing ROCK1 and ROCK2 from compensating for each other and resulting in profound pathology in the absence of B-cell ROCK1 alone. The transcriptomic analysis and mechanistic studies, furthermore, demonstrate that, in pathogenic settings associated with excessive hemolysis such as malaria, ROCK1 is a key regulator of the heme-Bach axis uncovering a novel protective role for this kinase. Precise calibration of ROCK1 activation levels could thus represent a useful mechanism by which B cells can rapidly tailor their differentiation to the nature of a pathogenic challenge and withstand exposure to damaging environments to ensure efficient and long-lasting humoral responses.

One of the most surprising aspects of these studies was the finding that lack of ROCK1 endows B cells with increased proinflammatory capabilities, particularly as it relates to the production of chemokines like CCL5. While unexpected, such a response could be important against severe pathogens that disarm RhoA, the key upstream activator of ROCK1, since it could enable B cells to recruit and organize an inflammatory infiltrate and "jump-start" responses during these infections. Surprisingly, the enhanced proinflammatory capabilities of ROCK1-deficient B cells were accompanied by the dysregulated assembly of p62 complexes containing key ripoptosome components, ZBP1, RIPK1, and RIPK3, long implicated in the orchestration of inflammatory responses and necroptosis in innate cells [52] but whose role in B cells is largely unexplored. Formation of these complexes in ROCK1-deficient B cells was not accompanied by increased cleavage of MLKL or enhanced cell death suggesting that, under these conditions, they primarily mediate a proinflammatory rather than a necroptotic role. Presence of TBK1 in the complexes likely accounts for this shift given the known ability of TBK1 to suppress RIPK1-induced cell death [53, 54]. Assembly of ripoptosome-like complexes skewed toward inflammation rather than death could be advantageous in B cells since it could avoid the potential elimination of pathogen-specific B cells while enabling B cells to function, at least for the short-term, as additional effectors in response to severe infections. Lack of ROCK1 also resulted in the recruitment of PLK1 to these p62 complexes and the upregulation of signatures related to the G2/M phase and mitotic spindle, consistent with studies showing that PLK1 activity can be regulated by its sequestration into "mitotic ripoptosomes" [38, 39]. Presence of PLK1 in these complexes could thus allow B cells to tightly adjust PLK1 activity under highly inflammatory and stressful conditions and avoid the emergence of B cell progeny with damaging chromosomal alterations.

These studies also demonstrate the existence of a critical cross-talk between ROCK1 and mTORC1, a complex regulator of several phases of B cell differentiation [55, 56, 57, 58]. While mTORC1 activation can promote the transition of activated B cells toward the later stages of differentiation [13], it can prevent the successful completion of the PC program if its activity becomes dysregulated [14]. Our studies indicate that loss of B-cell ROCK1 disrupts the fine-tuning of mTORC1 activity required for the successful execution of this program by leading to the formation of a pool of mTORC1 whose activation persists inappropriately. Interestingly, the range of mTORC1 substrates whose phosphorylation status was altered by the lack of ROCK1 was limited to a selected set of proteins that included 4EBP1 suggesting that this pool of mTORC1 can selectively control eIF4E activity and thus the translation of eIF4E-sensitive transcripts, which have been shown to encompass key regulators such as AICDA and Bcl6 [59, 60]. The mTORC1 targets affected by the absence of ROCK1 also included a site in p62, S349, whose phosphorylation, as predicted, resulted in the increased association of p62 with Keap1, a step known to promote antioxidant

responses and the phase separation of p62 [42, 61]. Thus, B-cell ROCK1 controls a crucial feedback loop between mTORC1 and p62 where p62, by interacting with raptor and subsequently activating mTOR via TRAF6-induced ubiquitination, helps to generate a local pool of active mTORC1. This pool of active mTORC1 may then further fuel its own compartmentalization by phosphorylating p62 thus helping to maintain a limited but critical set of mTORC1 functional capabilities during stress such as the translation of eIF4E-sensitive transcripts.

Notably, this work uncovers a novel interplay between ROCK1 and HRI, an eIF2α kinase with an ever-expanding biological role. In addition to its ability to mediate the ISR, HRI can also inhibit mTORC1-mediated signaling and act as a key sensor of protein misfolding [46, 47, 50] limiting the formation of toxic protein aggregates such as self-assembling amyloid-like filaments and $p62^{+}$ perinuclear aggresomes [48, 49]. The ability of ROCK1 to control HRI activity can thus provide B cells with a central regulatory node to coordinately regulate mTORC1 signaling, maintain proteostasis, and engage additional stress responses, if warranted by the presence of damaging agents like heme within their surroundings. HRI undergoes an extensive and complex cross-talk with several HSPs and proper regulation of the association of HRI with HSPs is necessary for its full activation [62, 63]. Studies have indeed demonstrated that while interaction of HRI with Hsc70 can help promote a mature-competent conformation of this kinase, persistent association of HRI with Hsc70 can attenuate its kinase activity in response to heme [64]. Similarly, release of HSPB8 from HRI has been shown to be critical to prevent formation of misfolded NOD1 aggregates and for HRI activation and engagement of the ISR [48]. Thus, by phosphorylating HRI and regulating its interaction with HSPs and sensitivity to heme, ROCK1 can enable B cells to take advantage of the different functional outputs of HRI to boost their stress responses when differentiating in the presence of damaging conditions. Interestingly, sequential phosphorylation of two heme-regulated proteins, Bach2 and HRI, by ROCK1 could provide a coordinated defense strategy to minimize the potentially toxic effects of heme on B cell differentiation helping to counteract the ability of pathogens like malaria to exploit hemolysis to avoid protective humoral responses.

Our studies thus support a role for ROCK1 as a critical regulatory hub that enables activated B cells to integrate information provided by key B-cell activation signals with cues regarding the concomitant presence of a pathogen and the extent of the surrounding damage. Loss of ROCK1 activity, as might be seen with severe pathogens that disable RhoA [21], may be the ultimate signal to differentiating B cells of extreme stress leading them to acquire enhanced proinflammatory features, sequester and protect key decision-makers in unique p62 compartments, and implement a set of emergency responses. Assembly of such compartments could provide B cells

differentiating in highly hostile and stressful environments with several advantages including more efficient signaling via the proximity of critical decision-makers and formation of signaling platforms, tight coordination of mitotic entry, enhanced protective antioxidant/stress responses, and maintenance of selected functional capabilities. Interestingly, phosphoproteomic alterations in ROCK1-deficient B cells could be observed even under αIgM+αCD40 stimulatory conditions where only minimal, if any, formation of p62 aggregates could be detected biochemically. These findings suggest that these p62 aggregates also assemble under those conditions, but that they may be unstable and that presence of pathogen-associated stressors drives their further maturation and/or stabilization likely by promoting the assembly of epichaperomes as supported by the PU-H71 inhibitor studies. Employment of ROCK1, a kinase whose activity can be quickly turned on or off, to dynamically adapt the molecular machinery of B cells to withstand pathogen-associated and environmental stressors could thus have broad relevance to infections, vaccine development, autoimmunity, and even malignancies.

The surprising role of ROCK1 in limiting inflammatory responses and restraining the assembly of p62 aggregates, furthermore, highlights the challenges of therapeutically targeting this family of kinases, a feat that is being undertaken for several age-related disorders like cardiovascular and, more recently, neurodegenerative diseases including ALS [65, 66]. It is indeed likely that the inhibitory roles of ROCK1 that we have identified are not confined to the B cell compartment but may extend to other cell types such as myeloid cells where the combination of PAMPs and heme has recently been shown to drive panoptosis [67] and neurons, which have high bioenergetic demands rendering them more susceptible to environmental insults. This notion is indeed supported by the remarkable concentration of ALS-associated machinery [18] such as TDP-43 and SOD1 in the p62 complexes formed in the absence of ROCK1 suggesting that these aggregates represent a point of convergence for fundamental pathways involved in RNA handling, protein quality control, and oxidative stress. Given the ability of ROCK1 to be normally controlled by a molecular switch, pathophysiological consequences could furthermore arise from either too high or too low ROCK1 activity. Delineating these differing settings could have great therapeutic relevance for human diseases including neurodegenerative disorders like ALS. Thus, our studies identify a fundamental mechanistic framework where rapid changes in ROCK1 activity can help coordinate a broad range of critical cellular programs to ensure organized, efficient decision-making when faced with sudden and potentially lethal pathogenic and damaging challenges.

Methods

Mice. All mice were on a C57BL/6 background. The generation of $Rock1^{fl/fl}$ was previously described [68]. CD23-cre mice were provided by Jayanta Chaudhuri and were previously described [26]. B6.129P2(Cg)-$Ighg1^{tm1(Cre)Cgn}$/J (Cγ1-Cre) mice were purchased from Jackson laboratories. Female mice between 6 and 12 weeks of age were used in *in vivo* experiments, both males and females were used in *in vitro* experiments. All mice used in the experiments were kept under specific pathogen–free conditions. All animal experiments were approved by the Institutional Animal Care and Use Committee of the Hospital for Special Surgery and WCMC/MSKCC and the experiments were carried out following these established guidelines.

Antibodies and flow cytometry. The following monoclonal antibodies to mouse proteins were used for multi-parameter flow cytometry: B220-PB or B220-APC/ Cy7 (RA3-6B2; 1:400), CD3-PE (145-2C11; 1:800), CD4-APC (RM4-5; 1:400), CD8-A700 (53-6.7; 1:200), CD11b-PE/Cy7 or CD11b-FITC (M1/70; 1:400), CD11c-APC/Cy7 or CD11c-APC (N418; 1:400), CD19-PB or CD19-PE (HIB19; 1:400), CD21-APC (7E9; 1:200), CD23-PE or CD23-PerCP/Cy5.5 (B3B4; 1:200), CD44-PCP or CD44-A700 (IM7; 1:200), IFNγ-A488 (XMG1.2, 1:400), and Tbet-PE (4B10; 1:800) were obtained from BioLegend. Streptavidin-conjugated antibodies were also obtained from BioLegend. Antibodies to CD138-APC (281-2; 1:1200), CXCR5-Biotin (2G8; 1:200), Fas-Biotin (Jo2; 1:200),and GL7-FITC (1:600) were obtained from BD. Antibodies to Foxp3-APC (FJK-16s; 1:100), IgD-FITC (11-26; 1:500), IgM-PE/Cy7 (II/41; 1:1000), and PD1-FITC (J43; 1:200) were obtained from eBioscience. Recombinant Mouse IL-21R (1:200)Fc Chimera protein was obtained from R&D systems. For intracellular staining, cells were fixed after surface staining at 4 °C with the Transcription Factor Staining Kit (eBioscience; #00-5523-00) following the manufacturer's instructions. For intracellular cytokine staining, splenocytes were stimulated with 50μg/mL PMA and 1μM Ionomycin for 4 hr. Cells were incubated with Brefeldin A for the final 3 h of stimulation. After stimulation, cells were fixed and permeabilized with a Transcription Factor Staining Kit (eBioscience; #00-5523-00) and stained using anti-IFNγ-APC (BioLegend; XMG1.2; 1:200) and recombinant mouse IL21R Fc Chimera (R&D; 1:600) followed by PE-labeled affinity-purified F(ab')2 fragment of goat anti-human Fcγ (Jackson ImmunoResearch). All data were acquired on a BD FACS Canto and analyzed with FlowJo (TreeStar) software.

Immunizations and malarial infection. Mice were immunized with 100 μg NP30–40-CGG in alum 0 to 28 days before analysis. To start blood-stage infections (BSL1), mice were injected i.p. with 1×10^6 infected RBCs per mouse of the nonlethal strain *Plasmodium yoelii* 17XNL resuspended in RPMI 1640 medium (Corning) as previously described [28] and were euthanized at

the indicated days by CO_2 asphyxiation and a secondary method as recommended by the Panel on Euthanasia of the American Veterinary Medical Association. To evaluate parasitemia, thin blood smears were made by bleeding mice from a nick in the tail. Smears were stained with KaryoMAX Giemsa (Life Technologies, Norwalk, CT), and a minimum of 500 RBCs per smear were counted. To evaluate anemia and other hematologic parameters, blood samples were submitted to the Laboratory of Comparative Medicine at WCM/MSKCC.

Cell sorting. For cell sorting, single-cell suspensions from pooled spleens were pre-enriched for B cells with biotinylated anti-B220 and streptavidin microbeads and B cells stained with B220, CD23, CD38, and GL7 (for the immunization experiments) or whole splenocytes stained with B220, CD19, CD138, and IgD (for the malarial infection experiments). Samples were sorted on either a BD FACS Aria II or a BD Influx.

JH4 sequencing. JH4 sequencing was performed as described previously [26]. In brief, an intronic region 3′ to the JH4 exon of IgH was PCR amplified from genomic DNA extracted from sorted GC B cells and follicular B cells from WT and Cγ1-*Rock1* mice. PCR products were cloned into the pCR4-Bunt-TOPO vector and sequenced with GeneWiz. The obtained JH4 intronic sequences were aligned to the mm9 assembly of the mouse genomic sequence. The following murine primers were used for JH4 sequencing: JH4 forward: 5'-GGA ATT CGC CTG ACA TCT GAG GAC TCT GC-3', JH4 reverse: 5'-GAC TAG TCC TCT CCA GTT TCG GCT GAA TCC-3'.

***ELISAs and ELISPOTs*.** For the total Ig ELISA, plates were coated with 10 μg/mL goat anti–mouse Ig at 4°C overnight and blocked in 1% BSA in PBS at RT for 1 hour. For the NP-specific Ig ELISA, plates were coated with 50 μg/mL NP-BSA conjugated at the appropriate ratio at 4°C overnight and blocked in 2% BSA in PBS at RT for 1 hour. Sera were diluted at various ratios and incubated on coated plates at 25°C for 2 hours. Plates were then incubated with either alkaline phosphate–labeled or HRP-labeled goat anti–mouse IgM, IgG1, IgG2c, or IgA Fc antibody for 1 hour before development. For anti-malaria antibody ELISAs, NUNC Immuno Microwell 96-wellplates (Thermo) were coated with 1:400 LD-column (Miltenyi) purified *P. yoelii*-infected lysates at 10^6 parasites/ μL at 37ºC overnight and blocked in 2% BSA in PBS at room temperature for 2 h. For anti-cardiolipin and anti-phosphatidylserine ELISA, Immulon 2HB plates (Thermo) were coated with 75μg/mL of cardiolipin or with 30 μg/mL phosphatidylserine dissolved in 100% ethanol overnight. Sera were diluted 1:200 and incubated on coated plates at 25 ºC for 2 hrs. Plates were then incubated with HRP-labeled goat anti-mouse IgM, IgG, IgG1, or IgG2c Fc

antibody for 1 h (eBioscience). After washing, TMB solution 1X (Thermo) was added and allowed to develop until desired color is obtained. Reaction was stopped with Stop solution (Invitrogen) and OD450 was measured on a microplate reader. For ELISPOT assays, plates were coated overnight at 4°C with 100 μg/mL goat anti–mouse Ig for detection of total Ig ASCs or 50 μg/mL NP-BSA conjugated at the appropriate ratio (NP>30 and NP<8) for detection of NP-specific Ig ASCs. Nonspecific binding was blocked with 3% BSA and 5% FBS in PBS, and samples were incubated at 37°C for 2 hours. Antibodies conjugated to biotin (goat anti–mouse IgG or goat anti–mouse IgM) were added and incubated overnight at 37°C followed by streptavidin-alkaline-phosphate and detection using 5-bromo-4- chloro-3-indolyl phosphate (BCIP).

Histology. Tissue specimens were fixed in 10% neutral buffered formalin and embedded in paraffin. Tissue sections were stained with periodic acid-Schiff (PAS) or with hematoxylin and eosin (H&E) and analyzed by light microscopy. The histological scoring system was adapted from published studies [69, 70] on malaria-associated pathology in patients infected with *Plasmodium falciparum*. Specimens were captured by Q capture software on a Nikon Eclipse microscope and quantifications were calculated using ImageJ software.

***RT-qPCR and DNA constructs*.** Total RNA was isolated using the RNeasy Plus Mini Kit (QIAGEN). cDNAs were prepared using the iScript cDNA synthesis kit. RT-qPCR was performed using the iTaq Universal SYBR Green Supermix. Gene expression was calculated using the ΔΔCt method and normalized to Cyclophilin A (murine *Ppia* Forward: 5′-TTGCCATTCCTGGACCCAAA-3′, murine *Ppia* Reverse: 5′-ATGGCACTGGCGGCAGGTCC-3′). RT-qPCR primers for *Rock1*, *Rock2*, *Prdm1* (BLIMP1) and *Bach2* were obtained from Qiagen. FLAG-tagged mouse Bach2 expression construct in pcDNA expression vector was a kind gift from Ari Melnick (WCM). Point mutants of FLAG-Bach2 were generated by PCR and confirmed by DNA sequencing. FLAG-tagged mouse HRI expression construct in pMXs Retroviral expression vector was obtained from Addgene (Plasmid # 101791).

RNA sequencing. The quality of all RNA and library preparations was evaluated with BioAnalyzer 2100 (Agilent Technologies). Sequencing libraries were sequenced by the Epigenomics Core Facility at Weill Cornell Medicine using a HiSeq 2500, 50-bp paired-end reads at a depth of approximately 22 to 30 million reads per sample. Read quality was assessed and adaptors trimmed using FASTP (58). Reads were then mapped to the mouse genome (mm10) and reads in exons were counted against Gencode v27 with STAR2.6 Aligner (59). Differential gene expression analysis was performed in R using edgeR 3.24.3. Genes with low expression levels (<2 counts per million in at least 1 group) were filtered from all downstream analyses. Replica-

associated batch correction was performed by directly incorporating a batch-specific term into a linear model. Differential expression was estimated using a quasi-likelihood framework. The Benhamini-Hochberg FDR procedure was used to correct for multiple testing. Genes with an unadjusted *P* value of less than 0.01 were considered differentially expressed. Downstream analyses were performed in R using a visualization platform build with Shiny developed by bioinformaticians at the David Z. Rosensweig Genomics Research Center at the HSS. GSEA was performed using GSEA software (Broad Institute)[59]. Genes were ranked by the difference of log-transformed counts per million for contrasted conditions. The Molecular Signatures Data-Base, version 62 (Broad Institute) was used as a source of gene sets with defined functional relevance. Gene sets ranging between 15 and 1000 genes were included in the analysis. Nominal *P* values were FDR corrected, and gene sets with an FDR below 0.05 were used to create GSEA enrichment plots.

Cell cultures and transfections. $CD23^+$ B cells were purified from single cell suspensions of splenocytes with biotinylated anti-CD23 (BD Bioscience; #553137) and streptavidin microbeads (Miltenyi Biotec; #130-048-101) as described [71]. Cells were cultured for 3 d in RPMI 1640 medium (Corning) supplemented with 10% FBS, 100 U/mL Penicillin, 100μg/mL Streptomycin, non-essential amino acids (Corning), 2 mM L-Glutamine (Corning), 25 mM HEPES (pH 7.2–7.6), and 50 μM β-Mercaptoethanol and stimulated with 5 μg/mL F(ab')2 anti-mouse IgM (Jackson ImmunoResearch), 5 μg/mL purified anti-mouse CD40 (BioXcell), a TLR9 ligand (TLR9-L, CpG ODN 1668, 1μg/ml) (Invivogen, Cat# tlrl-1668-1) and hemin (heme, 60μM) in various combinations. For autophagy assays BafilomycinA1 (50-100 nM, Sigma-Aldrich, Cat#B1793) was added for the last 4 hrs of culture. In selected experiment cycloheximide (100 μg/ml, Sigma-Aldrich, Cat# C4859) was added for the last 3-6 hrs of culture. 293T cells (CRL-3216; ATCC) were grown in DMEM with 10% FBS and 100 U/mL penicillin/streptomycin and transfected using the Mirus Transfection Kit with expression constructs for Flag-Bach2 (WT), or Flag-Bach2 mutants, or FLAG-HRI (WT).

Immunoblot analysis, kinase activity assays, and immunoprecipitations. Nuclear and cytoplasmic extracts were prepared with NE-PER Nuclear and Cytoplasmic Extraction Reagents (Pierce). Whole cell extracts were prepared as previously described [26]. Extracts were immunoprecipitated with anti-p62 (Cell Signaling Technology Cat #39749) antibody. Anti-Flag monoclonal antibody M2 conjugated with horseradish peroxidase (HRP) was obtained from Sigma-Aldrich, (Cat# A8592). For ROCK kinase activity assays, ROCK1 or ROCK2 was immunoprecipitated from whole cell extracts using anti-ROCK1 or anti-ROCK2 antibodies as

described previously [26] and quantifications were calculated using ImageJ software. ROCK1-mediated phosphorylation of Bach2 and HRI was assessed by *in vitro* ROCK1 kinase assays using active recombinant ROCK1 protein (Abcam, Cat# ab51415) and immunoprecipitated Flag-tagged Bach2 protein or FLAG-tagged HRI protein. Briefly, immunoprecipitated Bach2 was incubated with 400 ng purified active ROCK1 in kinase buffer (25 mM Tris, pH 7.5, 10 mM $MgCl_2$, 5 mM β-glycerolphosphate, 0.1 mM Na_3VO_4, and 2 mM DTT) containing 0.2mM ATP for 60 minutes at 30°C. The kinase reactions were terminated by washing the beads with 25 mM Tris, pH7.5 and then heating in SDS-PAGE sample buffer. The reactions products were resolved on a 8% SDS-PAGE gel followed by detection of phosphorylated Bach2 products using a Phospho-Ser/Thr (PKA Substrate) Ab (CST# 9621), which recognizes a consensus site similar to that of ROCK1. Since Phospho-HRI and Phospho-active ROCK1 have the same mobility on SDS-PAGE gel, ROCK1-mediated phosphorylation of FLAG-HRI was detected by mobility shift by immunoblotting with anti-FLAG mAb (M2)-HRPO. Noncontiguous lanes run on the same gel are separated by gray lines in the figures.

LC-MS/MS and proteomic data analysis.

Primary B cells phospho-proteomics: Cell pellets were lysed with buffer containing 8 M urea and 200 mM EPPS (pH at 8.5) with protease inhibitor (Roche) and phosphatase inhibitor cocktails 2 and 3 (Sigma). Benzonase (Millipore) was added to a concentration of 50u/mL and incubated (RT, 15 min) followed by water bath sonication. Samples were centrifuged at 4°C, 14,000 g's for 10 min and supernatant extracted. The Pierce bicinchoninic acid (BCA) protein concentration assay was used for determining protein concentration. Protein disulfide bonds were reduced with 5 mM tris (2-carboxyethyl) phosphine (room temperature, 15 min), then alkylated with 10 mM iodoacetamide (RT, 30 min, dark). The reaction was quenched with 10 mM dithiothreitol (RT, 15 min). Aliquots of 100 ug were taken for each sample and diluted to approximately 100 µL with lysis buffer. Samples were subject to chloroform/methanol precipitation as previously described[1]. Pellets were reconstituted in 200mM EPPS buffer and digested with Lys-C (1:50 enzyme-to-protein ratio) and trypsin (1:50 enzyme-to-protein ratio) digested at 37°C overnight. Peptides were TMT-labeled as described [72]. Briefly, peptides were TMT-tagged by addition of anhydrous ACN and TMTPro reagents (16plex) for each respective sample and incubated for 1 hr (RT). A ratio check was performed by taking a 1 µL aliquot from each sample and desalted by StageTip method [73]. TMT-tags were then quenched with hydroxylamine to a final concentration of 0.3% for 15 min (RT). Samples were pooled 1:1 based on the ratio check and vacuum-centrifuged to dryness. Dried peptides were reconstituted in 1mL of 3% ACN/1% TFA, desalted using a 100mg tC18 SepPak (Waters), and vacuum-centrifuged overnight. Phosphopeptides were enriched using the

Thermo High-Select Fe-NTA Phosphopeptide Enrichment Kit (Cat. No.: A32992). The phosphopeptide elute was vacuum centrifuged to dryness and reconstituted in 100 µL of 1% ACN/25mM ammonium bicarbonate (ABC). A StageTip was constructed by placing two plugs with a narrow bore syringe of a C18 disk (3M Empore Solid Phase Extraction Disk, #2315) into a 200 µL tip (VWR, Cat. No.: 89079-458). StageTips were conditioned with 100 µL of 100% ACN, 70% ACN/25mM ABC, then 1% ACN/25mM ABC. Phospho-enriched sample was loaded onto the StageTip and eluted into 6 fractions of 3, 5, 8, 10, 12, and 70% ACN/25mM ABC with 100 µL each. Fractions were immediately dried down by vacuum-centrifugation and reconstituted in 0.1% formic acid (FA) for LC-MS/MS.

Phospho-depleted peptides were centrifuged to dryness and reconstituted in 1 mL of 1% ACN/25mM ABC. Peptides were fractionated into 48 fractions. Briefly, an Ultimate 3000 HPLC (Dionex) coupled to an Ultimate 3000 Fraction Collector using a Waters XBridge BEH130 C18 column (3.5 um 4.6 x 250 mm) was operated at 1 mL/min. Buffer A, B, and C consisted of 100% water, 100% ACN, and 25mM ABC, respectively. The fractionation gradient operated as follows: 1% B to 5% B in 1 min, 5% B to 35% B in 61 min, 35% B to 60% B in 5 min, 60% B to 70% B in 3 min, 70% B to 1% B in 10min, with 10% C the entire gradient to maintain pH. The 48 fractions were then concatenated to 12 fractions, (i.e. fractions 1, 13, 25, 37 were pooled, followed by fractions 2, 14, 26, 38, etc.) so that every 12th fraction was used to pool. Pooled fractions were vacuum-centrifuged then reconstituted in 1% ACN/0.1% FA for LC-MS/MS.

Phosphopeptide-enriched and phospho-depleted peptide fractions were analyzed by LC-MS/MS using a Thermo Easy-nLC 1200 (Thermo Fisher Scientific) with a 50 cm (inner diameter 75µm) EASY-Spray Column (PepMap RSLC, C18, 2µm, 100Å) heated to 60°C coupled to a Orbitrap Fusion Lumos Tribrid Mass Spectrometer (Thermo Fisher Scientific). Peptides were separated at a flow rate of 300nL/min using a linear gradient of 1 to 35% acetonitrile (0.1% FA) in water (0.1% FA) over 4 hours and analyzed by SPS-MS3. MS1 scans were acquired over a range of m/z 375-1500, 120 K resolution, AGC target (standard), and maximum IT of 50 ms. MS2 scans were acquired on MS1 scans of charge 2-7 using an isolation of 0.7 m/z, collision induced dissociation with activation of 32%, turbo scan and max IT of 50 ms. MS3 scans were acquired using specific precursor selection (SPS) of 10 isolation notches, m/z range 100-1000, 50K resolution, AGC target (custom, 200%), HCD activation of 45%, and max IT of 150ms. The dynamic exclusion was set at 60s.

In vitro Bach2 phosphorylation: Samples were washed with 50mM EPPS (pH 8.5). Supernatant was removed and trypsin/Lys-C in 50mM EPPS was added (1:100 ratio) and digested overnight

at 37°C. An additional equal amount of trypsin/LysC was added and digested for 4 hours at 37°C. Samples were spun down, transferred to fresh Eppendorf tubes, and anhydrous acetonitrile (ACN) was added to each. Samples were TMT-labeled as described [72]. Briefly, samples were TMT-tagged by adding 4µL (28ug/µL) TMTPro reagents for each respective sample and incubated for 1hr (RT). TMT-tags were then quenched with hydroxylamine to a final concentration of 0.3% for 15 min (RT). Samples were pooled in their entirety then vacuum-centrifuged to dryness. Dried sample was reconstituted in 300µL 0.1% TFA and pH confirmed (adjusted when needed to acidic condition). The Pierce™ High pH Reversed-Phase Peptide Fractionation Kit (Cat. No.: 84868) was used to fractionate the pooled TMT sample into 8 fractions following manufacturer's instructions. The 8 fractions were concatenated to 4 fractions (i.e. fractions 1 and 5 pooled, 2 and 6, etc.) and vacuum-centrifuged to dryness. Fractions were reconstituted in 0.1% formic acid (FA) for LC-MS.

Statistics. All plots show datapoints from independent mice pooled across multiple experiments, unless otherwise noted. p-values were calculated with two-tailed t-tests or ANOVA followed by multi-group comparisons, as indicated in the figure legends. Statistical analysis was performed with Graphpad Prism 8.

ACKNOWLEDGEMENTS

We thank members of the HSS Research Institute for thoughtful discussions and reagents. This work was supported by the US National Institutes of Health (AR078766, AI58579 to ABP); T32 Rheumatology Research Training Grant to JRC and ER (T32 AR071302); the Lupus Research Alliance; the Peter Jay Sharp Foundation, the Tow Foundation which provided support for the David Z. Rosensweig Genomics Research Center, Giammaria Giuliani and the Ambrose Monell Foundation, and Marina Kellen French and the Anna-Maria and Stephen Kellen Foundation (DJ). Technical support was provided the Flow Cytometry Core Facility of Weill Cornell Medicine, by the Laboratory of Comparative Pathology and by the Microchemistry & Proteomics core at Memorial Sloan Kettering Cancer Center, and from the Office of the Director of the National Institutes of Health under Award Number S10OD019986 to Hospital for Special Surgery.

AUTHOR CONTRIBUTIONS

JRC designed and performed the experiments, interpreted the experiments, and wrote the manuscript; ER, SG, DFC, DJ and SV performed the experiments; TP assisted with the histological analyses; YBK provided the ROCK1$^{fl/fl}$ mice; MM and ZL performed and analyzed all the mass spectrometry and proteomics; EG analyzed the RNA-seq experiments; NZ and LC

helped write the manuscript; ABP designed and supervised the study, interpreted the experiments, and wrote the manuscript.

REFERENCES

1. Elsner, R.A. & Shlomchik, M.J. Germinal Center and Extrafollicular B Cell Responses in Vaccination, Immunity, and Autoimmunity. *Immunity* **53**, 1136-1150 (2020).

2. Akkaya, M., Kwak, K. & Pierce, S.K. B cell memory: building two walls of protection against pathogens. *Nat Rev Immunol* **20**, 229-238 (2020).

3. Myles, A., Sanz, I. & Cancro, M.P. T-bet(+) B cells: A common denominator in protective and autoreactive antibody responses? *Curr Opin Immunol* **57**, 40-45 (2019).

4. Ambegaonkar, A.A., Holla, P., Dizon, B.L., Sohn, H. & Pierce, S.K. Atypical B cells in chronic infectious diseases and systemic autoimmunity: puzzles with many missing pieces. *Curr Opin Immunol* **77**, 102227 (2022).

5. Rogers, K.J., Vijay, R. & Butler, N.S. Anti-malarial humoral immunity: the long and short of it. *Microbes Infect* **23**, 104807 (2021).

6. Perez-Mazliah, D., Ndungu, F.M., Aye, R. & Langhorne, J. B-cell memory in malaria: Myths and realities. *Immunol Rev* **293**, 57-69 (2020).

7. Price, M.J., Scharer, C.D., Kania, A.K., Randall, T.D. & Boss, J.M. Conserved Epigenetic Programming and Enhanced Heme Metabolism Drive Memory B Cell Reactivation. *J Immunol* **206**, 1493-1504 (2021).

8. Patterson, D.G., Kania, A.K., Zuo, Z., Scharer, C.D. & Boss, J.M. Epigenetic gene regulation in plasma cells. *Immunol Rev* **303**, 8-22 (2021).

9. Shinnakasu, R. & Kurosaki, T. Regulation of memory B and plasma cell differentiation. *Curr Opin Immunol* **45**, 126-131 (2017).

10. Ando, R. *et al.* The Transcription Factor Bach2 Is Phosphorylated at Multiple Sites in Murine B Cells but a Single Site Prevents Its Nuclear Localization. *J Biol Chem* **291**, 1826-1840 (2016).

11. Afzali, B. *et al.* BACH2 immunodeficiency illustrates an association between super-enhancers and haploinsufficiency. *Nat Immunol* **18**, 813-823 (2017).

12. Gaudette, B.T. & Allman, D. Biochemical coordination of plasma cell genesis. *Immunol Rev* **303**, 52-61 (2021).

13. Gaudette, B.T., Jones, D.D., Bortnick, A., Argon, Y. & Allman, D. mTORC1 coordinates an immediate unfolded protein response-related transcriptome in activated B cells preceding antibody secretion. *Nat Commun* **11**, 723 (2020).

14. Al Qureshah, F. *et al.* Activated PI3Kdelta signals compromise plasma cell survival via limiting autophagy and increasing ER stress. *J Exp Med* **218** (2021).

15. Battaglioni, S., Benjamin, D., Walchli, M., Maier, T. & Hall, M.N. mTOR substrate phosphorylation in growth control. *Cell* **185**, 1814-1836 (2022).

16. Duran, A. *et al.* p62 is a key regulator of nutrient sensing in the mTORC1 pathway. *Mol Cell* **44**, 134-146 (2011).

17. Linares, J.F. *et al.* K63 polyubiquitination and activation of mTOR by the p62-TRAF6 complex in nutrient-activated cells. *Mol Cell* **51**, 283-296 (2013).

18. Davidson, J.M., Chung, R.S. & Lee, A. The converging roles of sequestosome-1/p62 in the molecular pathways of amyotrophic lateral sclerosis (ALS) and frontotemporal dementia (FTD). *Neurobiol Dis* **166**, 105653 (2022).

19. Kumar, A.V., Mills, J. & Lapierre, L.R. Selective Autophagy Receptor p62/SQSTM1, a Pivotal Player in Stress and Aging. *Front Cell Dev Biol* **10**, 793328 (2022).

20. Loeven, N.A., Medici, N.P. & Bliska, J.B. The pyrin inflammasome in host-microbe interactions. *Curr Opin Microbiol* **54**, 77-86 (2020).

21. Lemichez, E. & Aktories, K. Hijacking of Rho GTPases during bacterial infection. *Exp Cell Res* **319**, 2329-2336 (2013).

22. Guan, G., Cannon, R.D., Coates, D.E. & Mei, L. Effect of the Rho-Kinase/ROCK Signaling Pathway on Cytoskeleton Components. *Genes (Basel)* **14** (2023).

23. Hartmann, S., Ridley, A.J. & Lutz, S. The Function of Rho-Associated Kinases ROCK1 and ROCK2 in the Pathogenesis of Cardiovascular Disease. *Front Pharmacol* **6**, 276 (2015).

24. Schmidt, S.I., Blaabjerg, M., Freude, K. & Meyer, M. RhoA Signaling in Neurodegenerative Diseases. *Cells* **11** (2022).

25. Sousa-Lima, I., Kim, H.J., Jones, J. & Kim, Y.B. Rho-Kinase as a Therapeutic Target for Nonalcoholic Fatty Liver Diseases. *Diabetes Metab J* **45**, 655-674 (2021).

26. Ricker, E. *et al.* Serine-threonine kinase ROCK2 regulates germinal center B cell positioning and cholesterol biosynthesis. *J Clin Invest* **130**, 3654-3670 (2020).

27. Ricker, E. *et al.* Selective dysregulation of ROCK2 activity promotes aberrant transcriptional networks in ABC diffuse large B-cell lymphoma. *Sci Rep* **10**, 13094 (2020).

28. Rivera-Correa, J. *et al.* Plasmodium DNA-mediated TLR9 activation of T-bet(+) B cells contributes to autoimmune anaemia during malaria. *Nat Commun* **8**, 1282 (2017).

29. Vijay, R. *et al.* Hemolysis-associated phosphatidylserine exposure promotes polyclonal plasmablast differentiation. *J Exp Med* **218** (2021).

30. Vijay, R. *et al.* Infection-induced plasmablasts are a nutrient sink that impairs humoral immunity to malaria. *Nat Immunol* **21**, 790-801 (2020).

31. Hipp, N. *et al.* IL-2 imprints human naive B cell fate towards plasma cell through ERK/ELK1-mediated BACH2 repression. *Nat Commun* **8**, 1443 (2017).

32. Dutt, P., Nguyen, N. & Toksoz, D. Role of Lbc RhoGEF in Galpha12/13-induced signals to Rho GTPase. *Cell Signal* **16**, 201-209 (2004).

33. Silvent, J., Gasse, B., Mornet, E. & Sire, J.Y. Molecular evolution of the tissue-nonspecific alkaline phosphatase allows prediction and validation of missense mutations responsible for hypophosphatasia. *J Biol Chem* **289**, 24168-24179 (2014).

34. Graser, S., Liedtke, D. & Jakob, F. TNAP as a New Player in Chronic Inflammatory Conditions and Metabolism. *Int J Mol Sci* **22** (2021).

35. Hornbeck, P.V. *et al.* PhosphoSitePlus, 2014: mutations, PTMs and recalibrations. *Nucleic Acids Res* **43**, D512-520 (2015).

36. Pandian, N. & Kanneganti, T.D. PANoptosis: A Unique Innate Immune Inflammatory Cell Death Modality. *J Immunol* **209**, 1625-1633 (2022).

37. Runde, A.P., Mack, R., S, J.P. & Zhang, J. The role of TBK1 in cancer pathogenesis and anticancer immunity. *J Exp Clin Cancer Res* **41**, 135 (2022).

38. Liccardi, G. *et al.* RIPK1 and Caspase-8 Ensure Chromosome Stability Independently of Their Role in Cell Death and Inflammation. *Mol Cell* **73**, 413-428 e417 (2019).

39. Gupta, K. & Liu, B. PLK1-mediated S369 phosphorylation of RIPK3 during G2 and M phases enables its ripoptosome incorporation and activity. *iScience* **24**, 102320 (2021).

40. Vasconcellos, L.R. *et al.* Protein aggregation as a cellular response to oxidative stress induced by heme and iron. *Proc Natl Acad Sci U S A* **113**, E7474-E7482 (2016).

41. Hey, F., Czyzewicz, N., Jones, P. & Sablitzky, F. DEF6, a novel substrate for the Tec kinase ITK, contains a glutamine-rich aggregation-prone region and forms cytoplasmic granules that co-localize with P-bodies. *J Biol Chem* **287**, 31073-31084 (2012).

42. Komatsu, M. p62 bodies: Phase separation, NRF2 activation, and selective autophagic degradation. *IUBMB Life* **74**, 1200-1208 (2022).

43. Cha-Molstad, H. *et al.* Amino-terminal arginylation targets endoplasmic reticulum chaperone BiP for autophagy through p62 binding. *Nat Cell Biol* **17**, 917-929 (2015).

44. Ginsberg, S.D., Sharma, S., Norton, L. & Chiosis, G. Targeting stressor-induced dysfunctions in protein-protein interaction networks via epichaperomes. *Trends Pharmacol Sci* **44**, 20-33 (2023).

45. Calvo-Vidal, M.N. *et al.* Oncogenic HSP90 Facilitates Metabolic Alterations in Aggressive B-cell Lymphomas. *Cancer Res* **81**, 5202-5216 (2021).

46. Chen, J.J. & Zhang, S. Heme-regulated eIF2alpha kinase in erythropoiesis and hemoglobinopathies. *Blood* **134**, 1697-1707 (2019).

47. Girardin, S.E., Cuziol, C., Philpott, D.J. & Arnoult, D. The eIF2alpha kinase HRI in innate immunity, proteostasis, and mitochondrial stress. *FEBS J* **288**, 3094-3107 (2021).

48. Abdel-Nour, M. *et al.* The heme-regulated inhibitor is a cytosolic sensor of protein misfolding that controls innate immune signaling. *Science* **365** (2019).

49. Mukherjee, T. *et al.* The eIF2alpha kinase HRI triggers the autophagic clearance of cytosolic protein aggregates. *J Biol Chem* **296**, 100050 (2021).

50. Zhang, S. *et al.* HRI coordinates translation by eIF2alphaP and mTORC1 to mitigate ineffective erythropoiesis in mice during iron deficiency. *Blood* **131**, 450-461 (2018).

51. Igarashi, J. *et al.* Autophosphorylation of heme-regulated eukaryotic initiation factor 2alpha kinase and the role of the modification in catalysis. *FEBS J* **278**, 918-928 (2011).

52. Tummers, B. & Green, D.R. Mechanisms of TNF-independent RIPK3-mediated cell death. *Biochem J* **479**, 2049-2062 (2022).

53. Xu, D. *et al.* TBK1 Suppresses RIPK1-Driven Apoptosis and Inflammation during Development and in Aging. *Cell* **174**, 1477-1491 e1419 (2018).

54. Taft, J. *et al.* Human TBK1 deficiency leads to autoinflammation driven by TNF-induced cell death. *Cell* **184**, 4447-4463 e4420 (2021).

55. Farmer, J.R. *et al.* Induction of metabolic quiescence defines the transitional to follicular B cell switch. *Sci Signal* **12** (2019).

56. Ersching, J. *et al.* Germinal Center Selection and Affinity Maturation Require Dynamic Regulation of mTORC1 Kinase. *Immunity* **46**, 1045-1058 e1046 (2017).

57. Cho, S.H. *et al.* Germinal centre hypoxia and regulation of antibody qualities by a hypoxia response system. *Nature* **537**, 234-238 (2016).

58. Gaudette, B.T. *et al.* Resting innate-like B cells leverage sustained Notch2/mTORC1 signaling to achieve rapid and mitosis-independent plasma cell differentiation. *J Clin Invest* **131** (2021).

59. Chiu, H. *et al.* The mTORC1/4E-BP/eIF4E Axis Promotes Antibody Class Switching in B Lymphocytes. *J Immunol* **202**, 579-590 (2019).

60. Yi, W. *et al.* The mTORC1-4E-BP-eIF4E axis controls de novo Bcl6 protein synthesis in T cells and systemic autoimmunity. *Nat Commun* **8**, 254 (2017).

61. Kageyama, S. *et al.* p62/SQSTM1-droplet serves as a platform for autophagosome formation and anti-oxidative stress response. *Nat Commun* **12**, 16 (2021).

62. Berwal, S.K. *et al.* Activation of HRI is mediated by Hsp90 during stress through modulation of the HRI-Hsp90 complex. *Int J Biol Macromol* **118**, 1604-1613 (2018).

63. Uma, S., Hartson, S.D., Chen, J.J. & Matts, R.L. Hsp90 is obligatory for the heme-regulated eIF-2alpha kinase to acquire and maintain an activable conformation. *J Biol Chem* **272**, 11648-11656 (1997).

64. Uma, S., Thulasiraman, V. & Matts, R.L. Dual role for Hsc70 in the biogenesis and regulation of the heme-regulated kinase of the alpha subunit of eukaryotic translation initiation factor 2. *Mol Cell Biol* **19**, 5861-5871 (1999).

65. Yu, B., Sladojevic, N., Blair, J.E. & Liao, J.K. Targeting Rho-associated coiled-coil forming protein kinase (ROCK) in cardiovascular fibrosis and stiffening. *Expert Opin Ther Targets* **24**, 47-62 (2020).

66. Mead, R.J., Shan, N., Reiser, H.J., Marshall, F. & Shaw, P.J. Amyotrophic lateral sclerosis: a neurodegenerative disorder poised for successful therapeutic translation. *Nat Rev Drug Discov* **22**, 185-212 (2023).

67. Sundaram, B. *et al.* NLRP12-PANoptosome activates PANoptosis and pathology in response to heme and PAMPs. *Cell* **186**, 2783-2801 e2720 (2023).

68. Huang, H. *et al.* Rho-kinase regulates energy balance by targeting hypothalamic leptin receptor signaling. *Nat Neurosci* **15**, 1391-1398 (2012).

69. Klinkhamhom, A. *et al.* M1 macrophage features in severe Plasmodium falciparum malaria patients with pulmonary oedema. *Malar J* **19**, 182 (2020).

70. Viriyavejakul, P., Khachonsaksumet, V. & Punsawad, C. Liver changes in severe Plasmodium falciparum malaria: histopathology, apoptosis and nuclear factor kappa B expression. *Malar J* **13**, 106 (2014).

71. Manni, M. *et al.* Regulation of age-associated B cells by IRF5 in systemic autoimmunity. *Nat Immunol* **19**, 407-419 (2018).

72. Navarrete-Perea, J., Yu, Q., Gygi, S.P. & Paulo, J.A. Streamlined Tandem Mass Tag (SL-TMT) Protocol: An Efficient Strategy for Quantitative (Phospho)proteome Profiling Using Tandem Mass Tag-Synchronous Precursor Selection-MS3. *J Proteome Res* **17**, 2226-2236 (2018).

73. Rappsilber, J., Mann, M. & Ishihama, Y. Protocol for micro-purification, enrichment, pre-fractionation and storage of peptides for proteomics using StageTips. *Nat Protoc* **2**, 1896-1906 (2007).

Figure 1

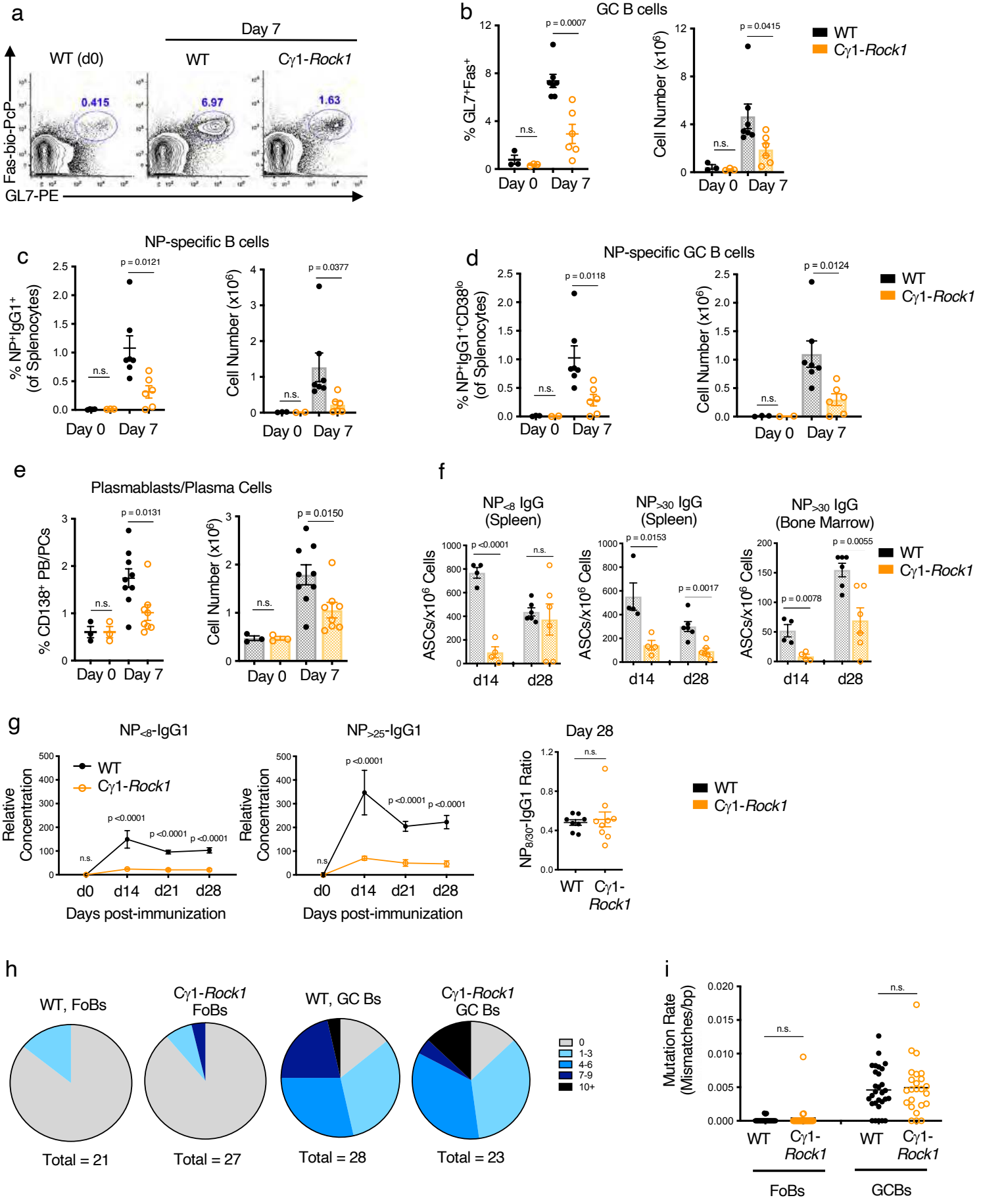
a
Day 7
WT (d0)
WT
Cγ1-Rock1
0.415
6.97
1.63
Fas-bio-PcP
GL7-PE
b
GC B cells
% GL7+Fas+
Cell Number (x10^6)
p = 0.0007
p = 0.0415
n.s.
Day 0
Day 7
WT
Cγ1-Rock1
c
NP-specific B cells
% NP+IgG1+ (of Splenocytes)
Cell Number (x10^6)
p = 0.0121
p = 0.0377
d
NP-specific GC B cells
% NP+IgG1+CD38lo (of Splenocytes)
p = 0.0118
p = 0.0124
e
Plasmablasts/Plasma Cells
% CD138+ PB/PCs
p = 0.0131
p = 0.0150
f
NP<8 IgG (Spleen)
NP>30 IgG (Spleen)
NP>30 IgG (Bone Marrow)
ASCs/x10^6 Cells
p <0.0001
p = 0.0153
p = 0.0017
p = 0.0078
p = 0.0055
d14
d28
g
NP<8-IgG1
NP>25-IgG1
Day 28
Relative Concentration
p <0.0001
d0
d14
d21
d28
Days post-immunization
NP8/30-IgG1 Ratio
WT
Cγ1-Rock1
h
WT, FoBs
Cγ1-Rock1 FoBs
WT, GC Bs
Cγ1-Rock1 GC Bs
0
1-3
4-6
7-9
10+
Total = 21
Total = 27
Total = 28
Total = 23
i
Mutation Rate (Mismatches/bp)
FoBs
GCBs

Suppl. Fig. 1

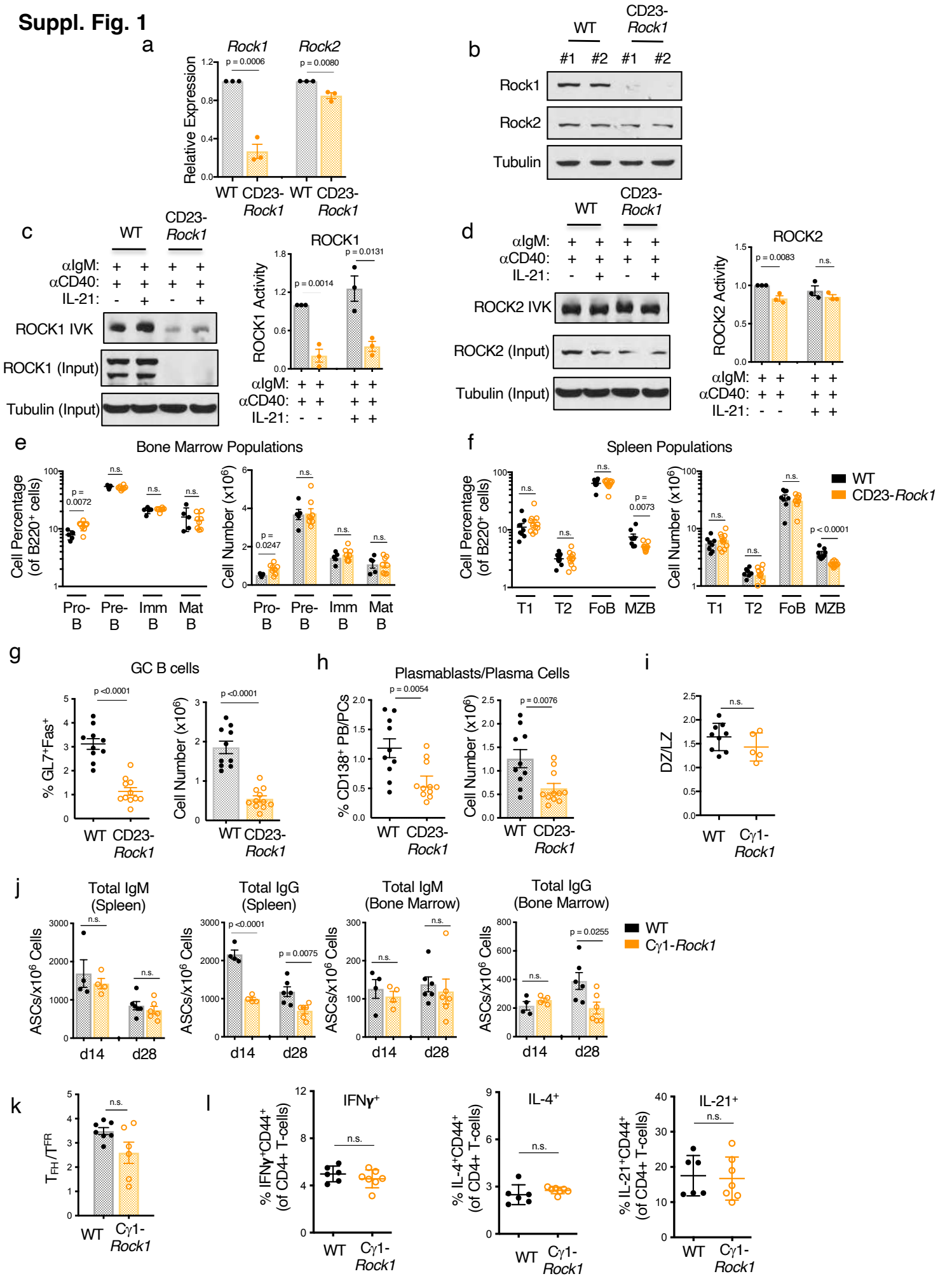
a
Rock1
Rock2
p = 0.0006
p = 0.0080
Relative Expression
WT
CD23-Rock1
b
WT
CD23-Rock1
#1 #2 #1 #2
Rock1
Rock2
Tubulin
c
αIgM:
αCD40:
IL-21:
ROCK1 IVK
ROCK1 (Input)
Tubulin (Input)
ROCK1
ROCK1 Activity
p = 0.0014
p = 0.0131
d
ROCK2 IVK
ROCK2 (Input)
Tubulin (Input)
ROCK2
ROCK2 Activity
p = 0.0083
n.s.
e
Bone Marrow Populations
Cell Percentage (of B220+ cells)
Cell Number (x10^6)
p = 0.0072
p = 0.0247
Pro-B
Pre-B
Imm B
Mat B
f
Spleen Populations
p = 0.0073
p < 0.0001
T1
T2
FoB
MZB
WT
CD23-Rock1
g
GC B cells
% GL7+Fas+
p <0.0001
Cell Number (x10^6)
h
Plasmablasts/Plasma Cells
% CD138+ PB/PCs
p = 0.0054
Cell Number (x10^6)
p = 0.0076
i
DZ/LZ
Cγ1-Rock1
j
Total IgM (Spleen)
Total IgG (Spleen)
Total IgM (Bone Marrow)
Total IgG (Bone Marrow)
ASCs/x10^6 Cells
p = 0.0075
p = 0.0255
d14
d28
WT
Cγ1-Rock1
k
TFH/TFR
l
IFNγ+
% IFNγ+CD44+ (of CD4+ T-cells)
IL-4+
% IL-4+CD44+ (of CD4+ T-cells)
IL-21+
% IL-21+CD44+ (of CD4+ T-cells)
n.s.

LEGENDS

Figure 1. B cell-ROCK1 promotes GC responses and ASC formation. (A-I) WT *(black)* and Cγ1-*Rock1 (orange)* mice were immunized with 100 μg NP-CGG for 7-28 days as indicated. Representative FACS plots (A) and pooled quantifications of Germinal Center (GC) B cells (B; $B220^+GL7^+Fas^+$), NP-specific B cells (C; $B220^+IgM^-IgD^-Gr1^-IgG1^+NP^+$), NP-specific GC B cells (D; $B220^+IgM^-IgD^-Gr1^-IgG1^+NP^+CD38^{lo}$), and plasmablasts/plasma cells (E, $B220^{lo}CD138^+$) from WT and Cγ1-*Rock1* mice as assessed by flow cytometry. Data representative of and/or pooled from 7 WT and 6 Cγ1-*Rock1* mice (A-D) or from 9 WT and 8 Cγ1-*Rock1* mice (E) across 2 (A-D) or 3 (E) independent experiments and show mean +/- SEM; p-value by unpaired two-tailed t-tests. (F) Quantifications of ELISPOTs performed on cell suspensions from spleens and bone marrow from WT and Cγ1-*Rock1* mice at d14 or d28 after immunization. Data pooled from 4 mice per genotype at day 14 or from 6 mice per genotype at day 28 across 2 independent experiments and show mean +/- SEM; p-value by unpaired two-tailed t-tests. (G) ELISA data showing relative concentrations of $NP_{<8}$-IgG1 and $NP_{>25}$-IgG1 in the serum of the indicated mice at d0-28 after immunization. Data pooled from 4 mice at day 14 and 8 mice from days 0, 21, and 28 per genotype across 2 independent experiments and show mean +/- SEM; p-value by 2-way ANOVA followed by Sidak's test for multiple comparisons. (H-I) Pie charts (H) and plots (I**)** showing the mutation frequency of the 470-bp JH4 region in sorted FoBs ($B220^+GL7^-CD38^{hi}CD23^+$) as control and GC B cells ($B220^+GL7^+CD38^{lo}$) on day 14 after immunization. *n*>36 clones from 4 mice per genotype. Data pooled from at least 23 clones per cell type per genotype across 2 independent experiments and show mean +/- SEM; p-value by Mann-Whitney test.

Supplementary Figure 1. (A) RT-qPCR data showing the expression of *Rock1* and *Rock2* in purified $CD23^+$ B cells from WT or CD23-*Rock1* mice. Data pooled from 3 independent experiments and show mean +/- SEM; p-value by unpaired two-tailed t-tests. (B) Representative immunoblot of ROCK1 and ROCK2 protein expression. (C-D) $CD23^+$ B cells from WT *(black)* and CD23-*Rock1 (orange)* mice were cultured with combinations of αIgM (5μg/mL), αCD40 (5μg/mL), and IL-21 (50ng/mL) for 3d. ROCK1 (C) and ROCK2 (D) *in vitro* kinase activity assays (IVKs) were performed on extracts obtained from the B cell cultures. Quantifications show densitometry ratio of pMYPT1 to ROCK input levels. Data representative of and/or pooled from 3 independent experiments and show mean +/- SEM; p-value by unpaired two-tailed t-tests. (E-F) Quantifications of pro-B cells (*pro-B;* $B220^+IgM^-CD43^+$), pre-B cells (*pre-B;* $B220^+IgM^-CD43^-$), immature B cells (*Imm B;* $B220^+IgM^{lo}$), and mature B cells (*Mat B;* $B220^+IgM^{hi}$) from the bone marrow (E) and of transitional T1 B cells (*T1;* $B220^+CD23^-CD21^{lo}IgM^{hi}$), transitional T2 B cells (*T2;* $B220^+CD23^+CD21^+IgM^{hi}$), follicular B cells (*FoB;* $B220^+CD23^+CD21^{mid/lo}IgM^{mid/lo}$), and marginal

zone B cells (*MZB;* $B220^{+}CD23^{-}CD21^{hi}IgM^{hi}$) from the spleens (F) of the indicated mice. Data pooled from 5 WT and 9 CD23-*Rock1* mice (E) or 8 WT and 11 CD23-*Rock1* mice (F) across 2 (E) or 4 (F) independent experiments and show mean +/- SEM; p-value by unpaired two-tailed t-tests. (G-H) WT *(black)* and CD23-*Rock1 (orange)* mice were immunized with 100μg NP-CGG and were assessed for spleen germinal center (GC) B-cells (G; $B220^{+}GL7^{+}$ Fas^{+}) and plasmablasts/plasma cells (H, $B220^{lo}$ $CD138^{+}$) by flow cytometry at day 7. Data pooled from 10 WT and 11 CD23-*Rock1* mice across 5 independent experiments and show mean +/- SEM; p-value by unpaired two-tailed t-tests. (I) Ratio of dark ($CXCR4^{hi}$ $CD86^{lo}$)/light ($CXCR4^{lo}$ $CD86^{hi}$) (DZ/LZ) zone GC B cells from WT and Cγ1-*Rock1* immunized mice at day 7. Data pooled from 9 WT and 5 Cγ1-*Rock1* mice across 4 independent experiments and show mean +/- SEM; p-value by unpaired two-tailed t-test. (J) Quantifications of ELISPOTs performed on suspensions from spleens and bone marrow from WT and Cγ1-*Rock1* mice at d14 or d28 after immunization as indicated. Data pooled from 4 mice per genotype at d14 and from 6 mice per genotype at d28 and show mean +/- SEM; p-value by unpaired two-tailed t-tests. (K-L) Ratio of T-follicular helper cells/T-regulatory cells (T_{fh}/T_{fr}) and frequencies of cytokine producing T-cells (IFN-γ, IL-4 and IL-21) from WT and Cγ1-*Rock1* immunized mice at day 10. Data pooled from 7 WT and 6 Cγ1-*Rock1* mice (K) or from 6 WT and 7 Cγ1-*Rock1* mice (L) across 2 independent experiments and show mean +/- SEM; p-value by unpaired two-tailed t-tests.

Figure 2

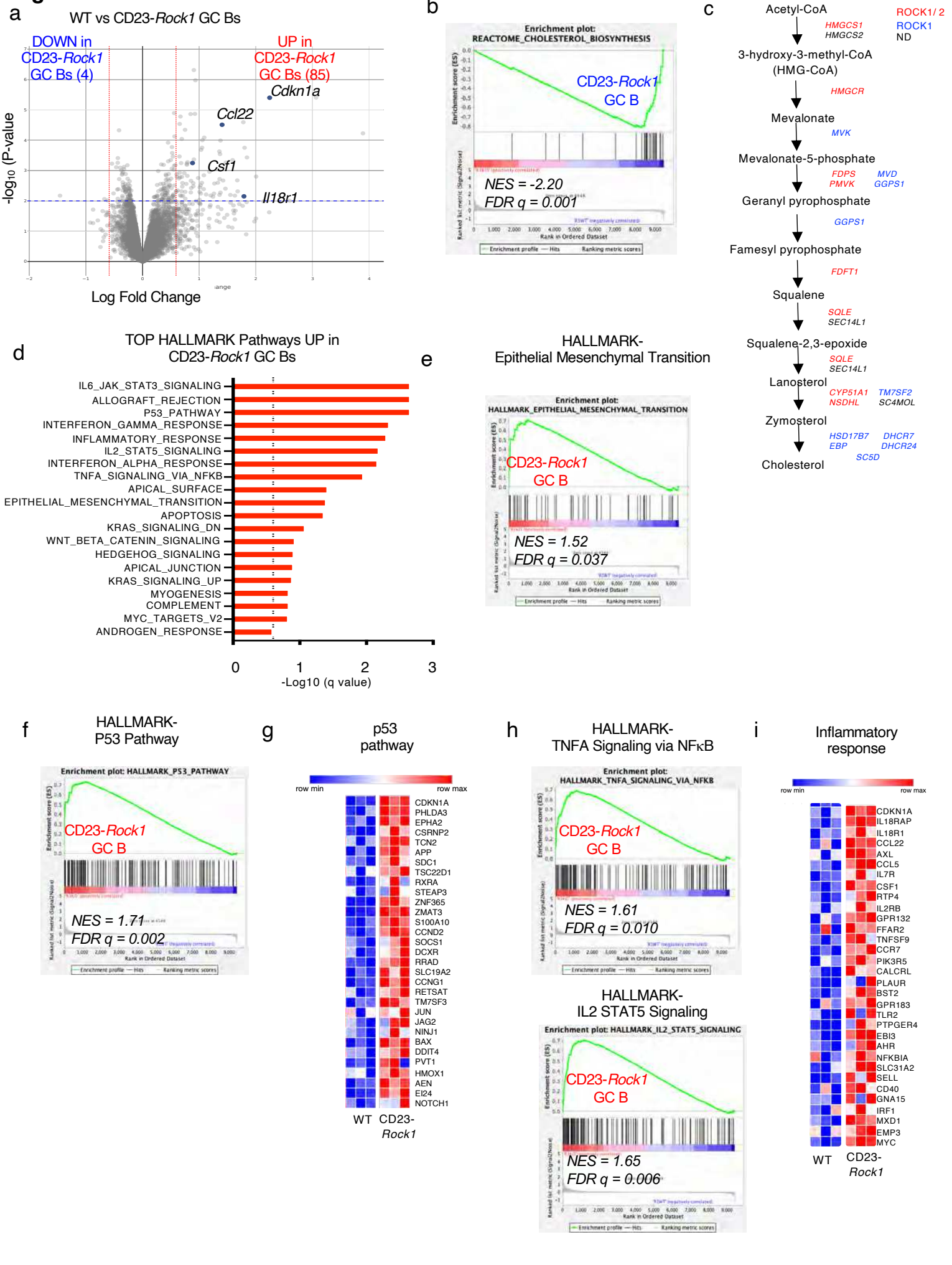
a
WT vs CD23-Rock1 GC Bs
DOWN in CD23-Rock1 GC Bs (4)
UP in CD23-Rock1 GC Bs (85)
Cdkn1a
Ccl22
Csf1
Il18r1
-log10 (P-value
Log Fold Change
b
Enrichment plot: REACTOME_CHOLESTEROL_BIOSYNTHESIS
CD23-Rock1 GC B
NES = -2.20
FDR q = 0.001
c
Acetyl-CoA
HMGCS1
HMGCS2
ROCK1/ 2
ROCK1
ND
3-hydroxy-3-methyl-CoA (HMG-CoA)
HMGCR
Mevalonate
MVK
Mevalonate-5-phosphate
FDPS
PMVK
MVD
GGPS1
Geranyl pyrophosphate
GGPS1
Famesyl pyrophosphate
FDFT1
Squalene
SQLE
SEC14L1
Squalene-2,3-epoxide
SQLE
SEC14L1
Lanosterol
CYP51A1
NSDHL
TM7SF2
SC4MOL
Zymosterol
HSD17B7
EBP
DHCR7
DHCR24
SC5D
Cholesterol
d
TOP HALLMARK Pathways UP in CD23-Rock1 GC Bs
IL6_JAK_STAT3_SIGNALING
ALLOGRAFT_REJECTION
P53_PATHWAY
INTERFERON_GAMMA_RESPONSE
INFLAMMATORY_RESPONSE
IL2_STAT5_SIGNALING
INTERFERON_ALPHA_RESPONSE
TNFA_SIGNALING_VIA_NFKB
APICAL_SURFACE
EPITHELIAL_MESENCHYMAL_TRANSITION
APOPTOSIS
KRAS_SIGNALING_DN
WNT_BETA_CATENIN_SIGNALING
HEDGEHOG_SIGNALING
APICAL_JUNCTION
KRAS_SIGNALING_UP
MYOGENESIS
COMPLEMENT
MYC_TARGETS_V2
ANDROGEN_RESPONSE
0
1
2
3
-Log10 (q value)
e
HALLMARK- Epithelial Mesenchymal Transition
Enrichment plot: HALLMARK_EPITHELIAL_MESENCHYMAL_TRANSITION
CD23-Rock1 GC B
NES = 1.52
FDR q = 0.037
f
HALLMARK- P53 Pathway
Enrichment plot: HALLMARK_P53_PATHWAY
CD23-Rock1 GC B
NES = 1.71
FDR q = 0.002
g
p53 pathway
row min
row max
CDKN1A
PHLDA3
EPHA2
CSRNP2
TCN2
APP
SDC1
TSC22D1
RXRA
STEAP3
ZNF365
ZMAT3
S100A10
CCND2
SOCS1
DCXR
RRAD
SLC19A2
CCNG1
RETSAT
TM7SF3
JUN
JAG2
NINJ1
BAX
DDIT4
PVT1
HMOX1
AEN
EI24
NOTCH1
WT
CD23-Rock1
h
HALLMARK- TNFA Signaling via NFκB
Enrichment plot: HALLMARK_TNFA_SIGNALING_VIA_NFKB
CD23-Rock1 GC B
NES = 1.61
FDR q = 0.010
HALLMARK- IL2 STAT5 Signaling
Enrichment plot: HALLMARK_IL2_STAT5_SIGNALING
CD23-Rock1 GC B
NES = 1.65
FDR q = 0.006
i
Inflammatory response
row min
row max
CDKN1A
IL18RAP
IL18R1
CCL22
AXL
CCL5
IL7R
CSF1
RTP4
IL2RB
GPR132
FFAR2
TNFSF9
CCR7
PIK3R5
CALCRL
PLAUR
BST2
GPR183
TLR2
PTPGER4
EBI3
AHR
NFKBIA
SLC31A2
SELL
CD40
GNA15
IRF1
MXD1
EMP3
MYC
WT
CD23-Rock1

Suppl. Fig. 2

a

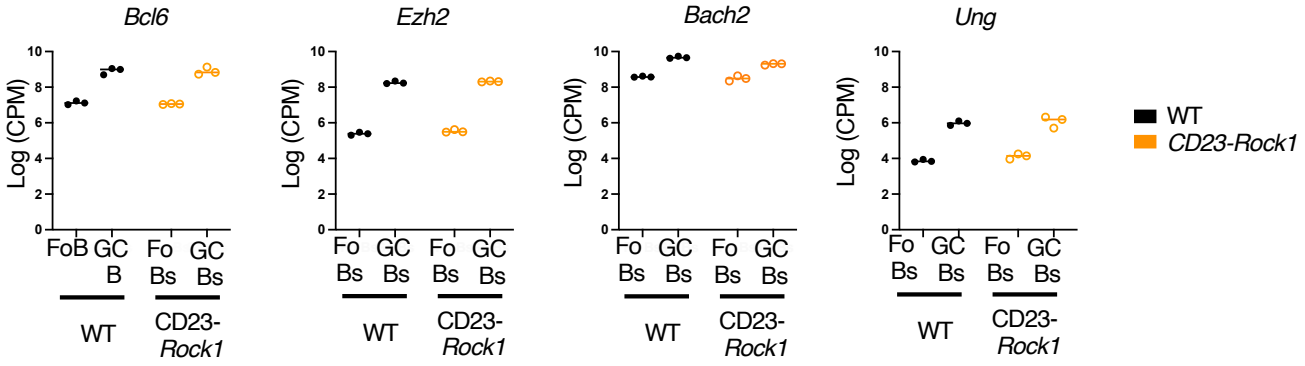

b

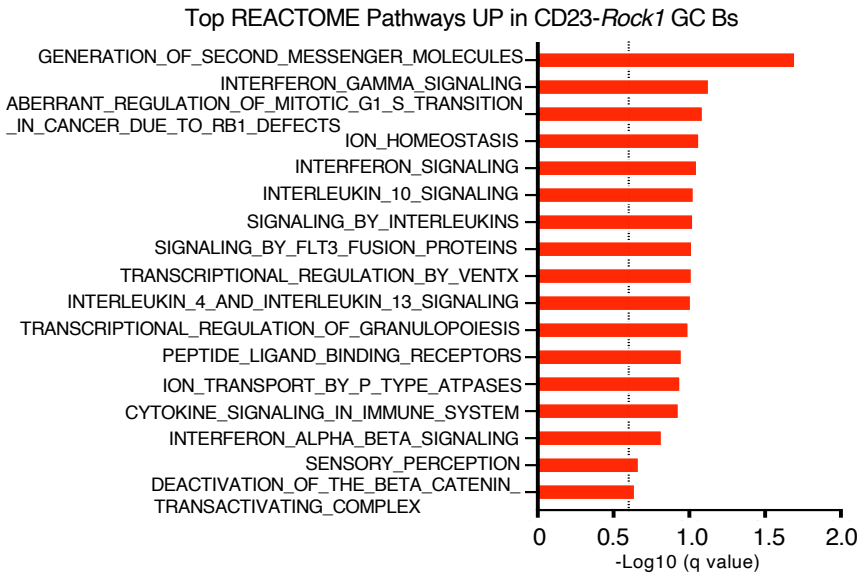

Figure 2. ROCK1 regulates a distinctive transcriptional program in GC B cells. WT or CD23-*Rock1* mice were immunized with 100 μg NP-CGG and at day 7 GC B cells ($B220^{+}GL7^{+}CD38^{lo}$) were sorted for bulk RNA-Seq analysis. (A) Volcano plot shows the genes differentially expressed (unadjusted $P < 0.01$, Log Fold change > 0.58) between WT and CD23-*Rock1* GC B cells. (B) GSEA plot shows the downregulation of the REACTOME_CHOLESTEROL_BIOSYNTHESIS pathway in CD23-*Rock1* GC B cells. (C) Schematic diagram of the cholesterol biosynthesis pathway. Enzymes highlighted in blue are encoded by genes that contribute to the downregulation of the REACTOME_CHOLESTEROL_BIOSYNTHESIS gene set in CD23-*Rock1* GC B cells only, those highlighted in red are the ones that also contribute to the downregulation of the GO_STEROL_BIO- SYNTHETIC_PROCESS gene set in CD23-*Rock2* GC B cells and those in black are not affected in either ROCK1 or ROCK2-deficient GC B cells. (D) Plot shows the top enriched HALLMARK pathways upregulated in CD23-Rock1 GC B cells as compared with WT GC B cells. Dotted line indicates significance cutoff at FDR Q = 0.25. (E, F, H) GSEA plots shows the enrichment of the HALLMARK_EPITHELIAL_MESENCHYMAL_TRANSITION (E), HALLMARK_P53_PATHWAY (F), HALLMARK_TNFA_SIGNALING_VIA_NFKB and HALLMARK_IL2_STAT5_SIGNALING (H) gene sets in CD23-*Rock1* GC B cells. (G, I) Heatmaps of the scaled expression of genes enriching the HALLMARK p53 pathway (G) and Inflammatory response pathway (I) in CD23-*Rock1* GC B cells.

Supplementary Figure 2. (A) Plots showing the normalized log- transformed counts per millions for the indicated genes from the RNA-seq analysis in Figure 2. (B) Plot shows the top enriched REACTOME pathways upregulated in CD23-Rock1 GC B cells compared with WT GC B cells. Dotted line indicates significance cutoff at FDR Q = 0.25.

Figure 3

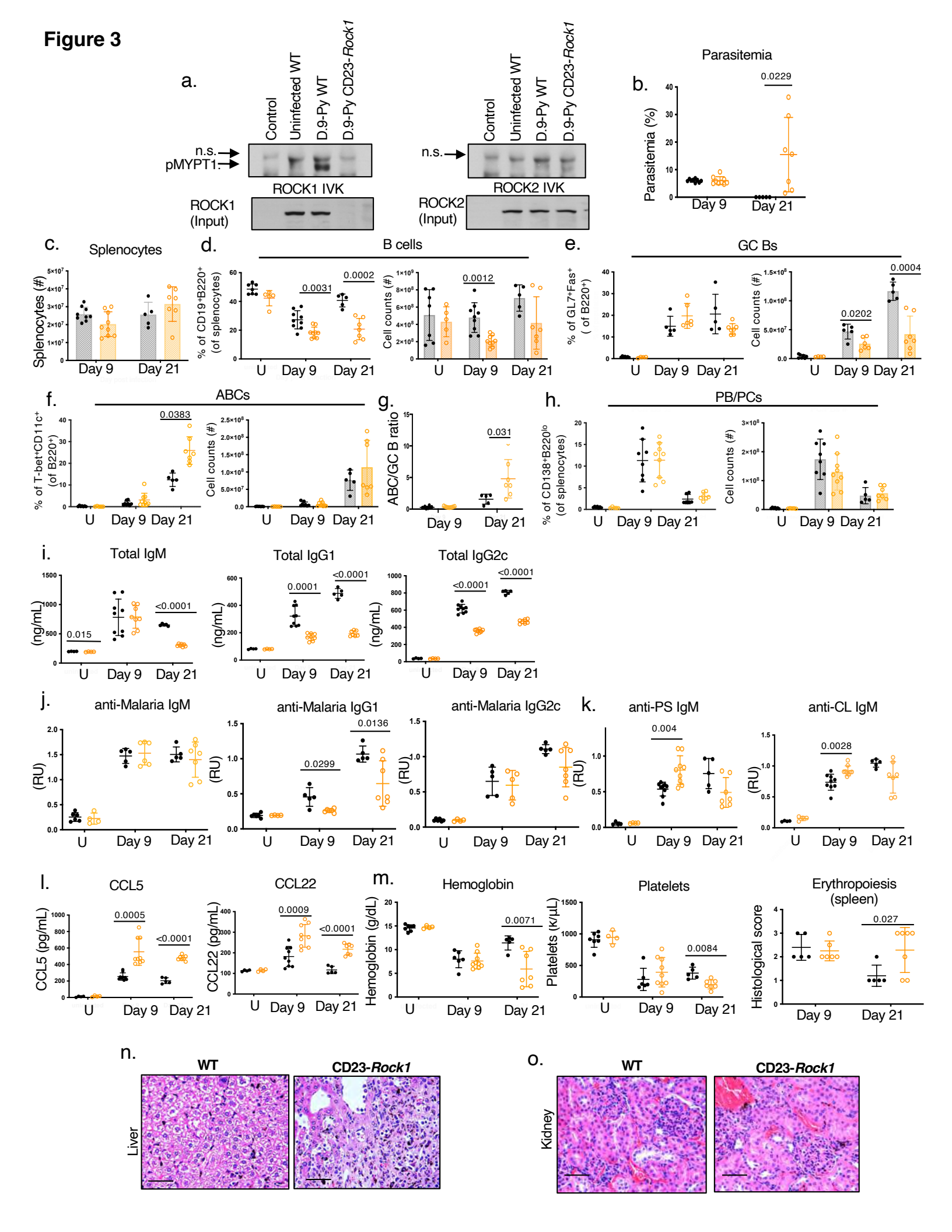
a.
Control
Uninfected WT
D.9-Py WT
D.9-Py CD23-Rock1
n.s.
pMYPT1
ROCK1 IVK
ROCK1 (Input)
n.s.
ROCK2 IVK
ROCK2 (Input)
b.
Parasitemia
Parasitemia (%)
0.0229
Day 9
Day 21
c.
Splenocytes
Splenocytes (#)
d.
B cells
% of CD19+B220+ (of splenocytes)
0.0031
0.0002
Cell counts (#)
0.0012
e.
GC Bs
% of GL7+Fas+ (of B220+)
0.0202
0.0004
f.
ABCs
% of T-bet+CD11c+ (of B220+)
0.0383
g.
ABC/GC B ratio
0.031
h.
PB/PCs
% of CD138+B220lo (of splenocytes)
i.
Total IgM
0.015
<0.0001
Total IgG1
0.0001
<0.0001
Total IgG2c
<0.0001
<0.0001
(ng/mL)
j.
anti-Malaria IgM
anti-Malaria IgG1
0.0299
0.0136
anti-Malaria IgG2c
(RU)
k.
anti-PS IgM
0.004
anti-CL IgM
0.0028
l.
CCL5
0.0005
<0.0001
CCL5 (pg/mL)
CCL22
0.0009
<0.0001
CCL22 (pg/mL)
m.
Hemoglobin
0.0071
Hemoglobin (g/dL)
Platelets
0.0084
Platelets (K/μL)
Erythropoiesis (spleen)
0.027
Histological score
U
Day 9
Day 21
n.
WT
CD23-Rock1
Liver
o.
WT
CD23-Rock1
Kidney

Suppl. Fig. 3

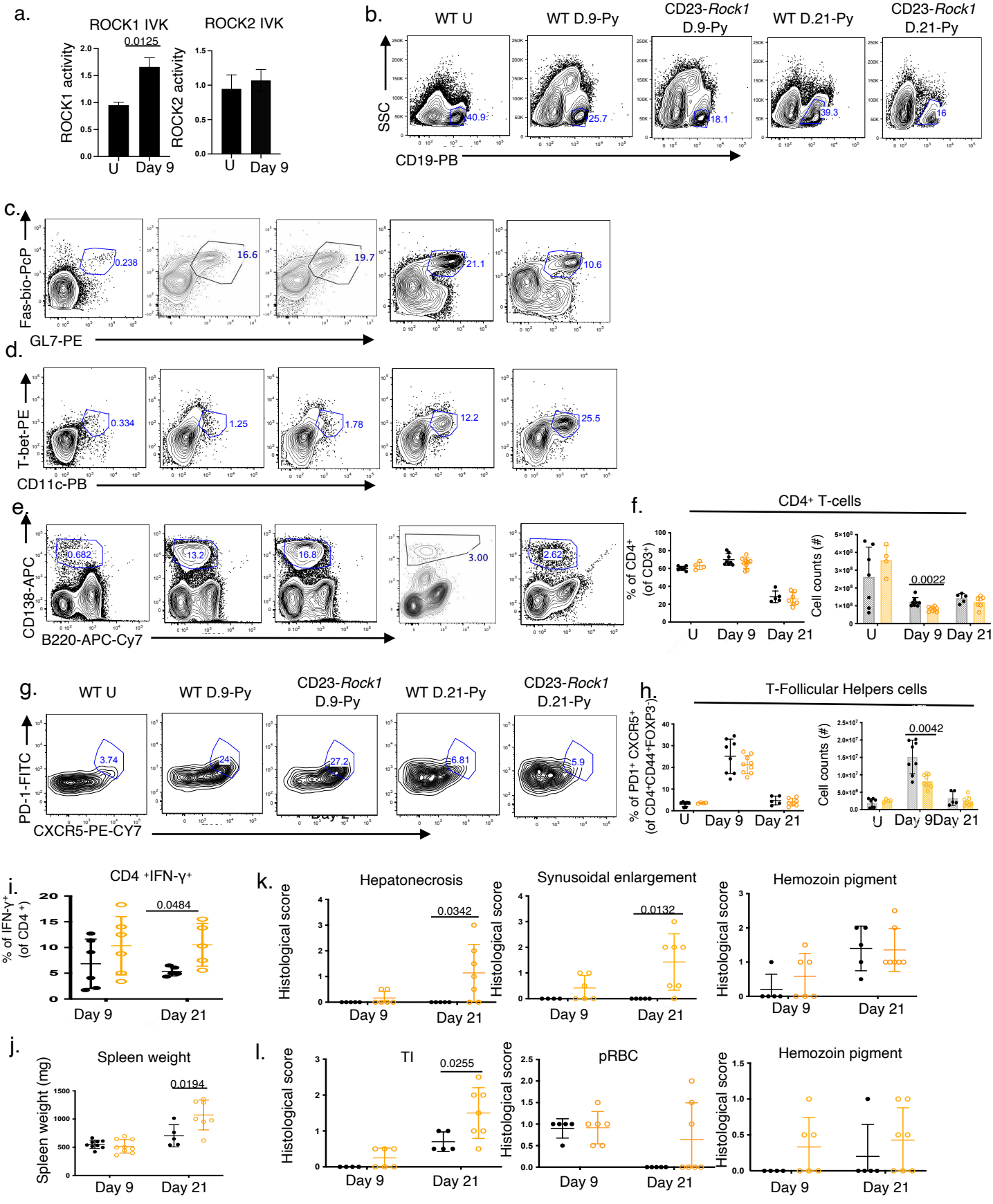
a.
ROCK1 IVK
ROCK2 IVK
0.0125
ROCK1 activity
ROCK2 activity
U
Day 9
b.
WT U
WT D.9-Py
CD23-Rock1 D.9-Py
WT D.21-Py
CD23-Rock1 D.21-Py
SSC
CD19-PB
40.9
25.7
18.1
39.3
16
c.
Fas-bio-PcP
GL7-PE
0.238
16.6
19.7
21.1
10.6
d.
T-bet-PE
CD11c-PB
0.334
1.25
1.78
12.2
25.5
e.
CD138-APC
B220-APC-Cy7
0.682
13.2
16.8
3.00
2.62
f.
CD4⁺ T-cells
% of CD4⁺ (of CD3⁺)
Cell counts (#)
0.0022
U
Day 9
Day 21
g.
WT U
WT D.9-Py
CD23-Rock1 D.9-Py
WT D.21-Py
CD23-Rock1 D.21-Py
PD-1-FITC
CXCR5-PE-CY7
3.74
24
27.2
6.81
5.9
h.
T-Follicular Helpers cells
% of PD1⁺ CXCR5⁺ (of CD4⁺CD44⁺FOXP3⁻)
Cell counts (#)
0.0042
i.
CD4 ⁺IFN-γ⁺
% of IFN-γ⁺ (of CD4 ⁺)
0.0484
Day 9
Day 21
k.
Hepatonecrosis
Synusoidal enlargement
Hemozoin pigment
Histological score
0.0342
0.0132
j.
Spleen weight
Spleen weight (mg)
0.0194
l.
TI
pRBC
Hemozoin pigment
0.0255

Figure 3. ROCK1 controls humoral and pathological responses to malaria infection. (A) WT or CD23-*Rock1* mice were infected with 10^6 *Plasmodium yoelii* 17XNL-infected erythrocytes and ROCK1 (left panel) and ROCK2 (right panel) activity in purified $CD23^+$ splenic B cells was assessed by IVKs at day 9 pi. IVKs were performed by immunoprecipitating ROCK1 or ROCK2 from the extracts and incubating with recombinant MYPT1 as a substrate. Phosphorylated recombinant MYPT1 (p-MYPT1) was detected using an antibody against p-MYPT1. Total ROCK1 and ROCK2 input levels for each sample are shown in the lower panels. (B) WT (black) or CD23-*Rock1* mice (orange) were infected with 10^6 *Plasmodium yoelii* 17XNL-infected erythrocytes and parasitemia quantitated at Day 9 or day 21 pi. (C-H) B-cell populations were assessed by flow cytometry on Day 9 and Day 21 post-infection (pi). Quantification of total splenocyte numbers (C). Quantification plots of frequencies (symbols) and total cell numbers (bars) of splenic B-cells ($CD19^+$) (D), GC B cells ($B220^+GL7^+Fas^+$) (E), ABCs ($B220^+CD11c^+T\text{-}bet^+$) (F), Plasmablasts/Plasma cells ($B220^{int}$ $CD138^+$) (H) from uninfected mice (u) or from infected mice Day 9 or Day 21 pi. (G) Ratio of splenic ABC to GC B cells. Data (for all panels) representative of at least 4 mice per genotype and show mean +/- SEM; p-value by unpaired two-tailed t-tests. (I-K) ELISA data of total IgM, IgG1, and IgG2c levels (I), anti-malaria IgM, IgG1, and IgG2c (J), anti-phosphatidylserine (anti-PS) and anticardiolipin (anti-CL) IgM levels (K), and CCL5 and CCL22 (L) from the sera of uninfected or infected WT or CD23-*Rock1* mice at Day 9 or Day 21 pi. (M) Plots showing blood hemoglobin levels, platelet counts, and splenic red pulp erythropoiesis (as determined by H&E stain). (N-O) Representative histological images of liver (N) and kidney (O) as determined by H&E stain. Scale bars: 50 μm. *n* = at least 4 mice per genotype from 3 independent experiments.

Supplementary Figure 3. (A) Quantifications of p-MYPT1 to input ROCK1 (left panel) or ROCK2 (right panel) protein expression for Fig. 3A (*n* = 3). (B-G) Representative FACS plots of splenic B-cells ($CD19^+$) (B), Germinal Center B-cells ($B220^+GL7^+Fas^+$) (C), ABCs ($B220^+CD11c^+T\text{-}bet^+$) (D), and Plasmablasts/Plasma cells ($B220^{int}CD138^+$) (E) from uninfected or infected mice at Day 9 or Day 21 pi. (F) Quantifications of splenic total $CD4^+$ T-cells ($CD3^+CD4^+$), (G-H) Representative FACS plots and quantification of T-follicular helper cells ($CD3^+CD4^+CD44^+CXCR5^+PD1^+FOXP3^-$) from uninfected or infected mice at Day 9 or Day 21 pi (I) Frequencies of $CD4^+$ $IFN\gamma^+$ T-cells. (J) Spleen weight of WT and CD23-*Rock1* mice at Day 9 or Day 21 pi. (K-L) Scores of histological images of liver (K) and kidney (L) at Day 9 or Day 21 pi.

Figure 4

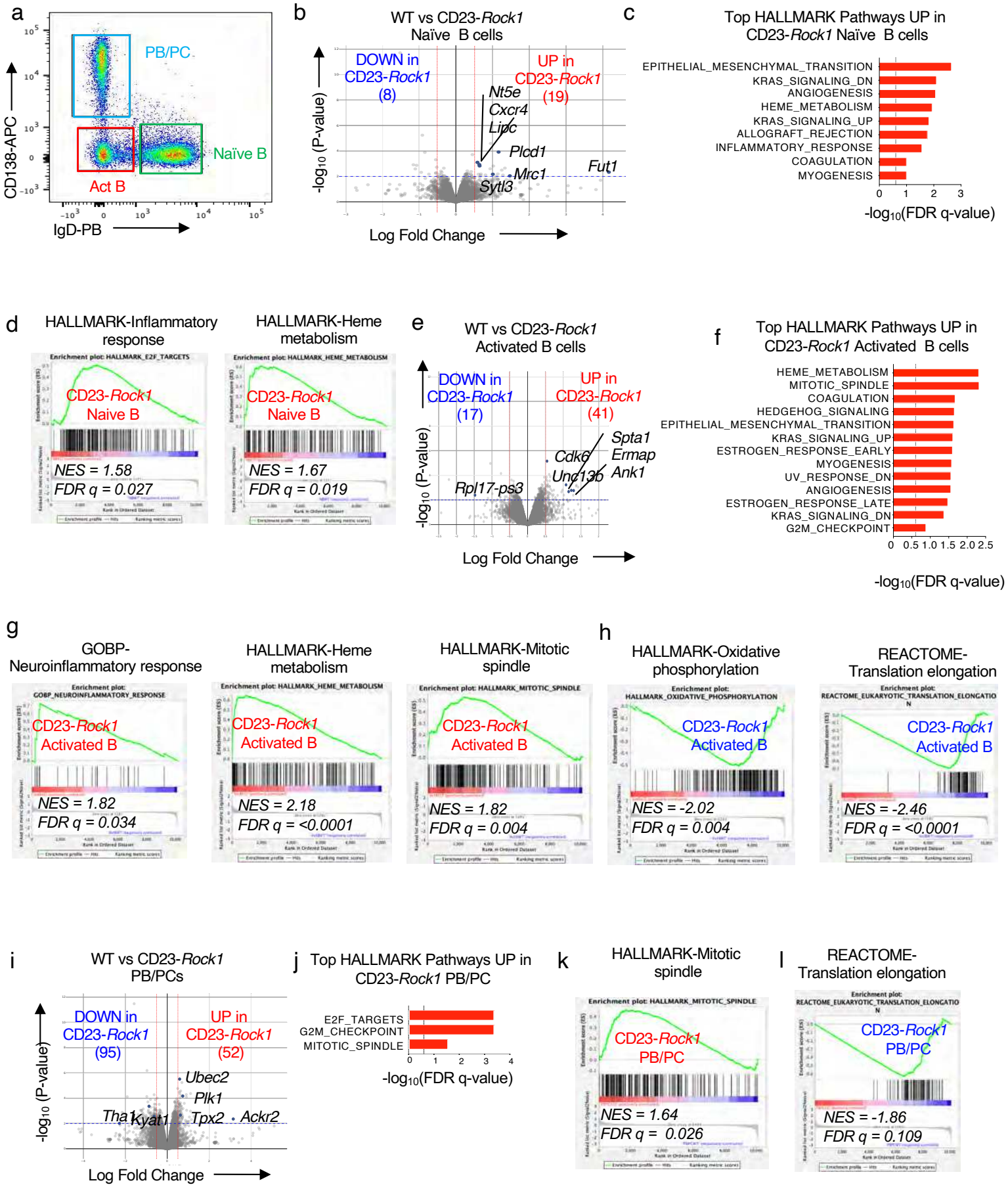
a
PB/PC
Naïve B
Act B
CD138-APC
IgD-PB
b
WT vs CD23-Rock1
Naïve B cells
DOWN in
CD23-Rock1
(8)
UP in
CD23-Rock1
(19)
Nt5e
Cxcr4
Lipc
Plcd1
Mrc1
Sytl3
Fut1
-log10 (P-value)
Log Fold Change
c
Top HALLMARK Pathways UP in
CD23-Rock1 Naïve B cells
EPITHELIAL_MESENCHYMAL_TRANSITION
KRAS_SIGNALING_DN
ANGIOGENESIS
HEME_METABOLISM
KRAS_SIGNALING_UP
ALLOGRAFT_REJECTION
INFLAMMATORY_RESPONSE
COAGULATION
MYOGENESIS
-log10(FDR q-value)
d
HALLMARK-Inflammatory
response
CD23-Rock1
Naive B
NES = 1.58
FDR q = 0.027
HALLMARK-Heme
metabolism
CD23-Rock1
Naive B
NES = 1.67
FDR q = 0.019
e
WT vs CD23-Rock1
Activated B cells
DOWN in
CD23-Rock1
(17)
UP in
CD23-Rock1
(41)
Spta1
Ermap
Ank1
Cdk6
Unc13b
Rpl17-ps3
-log10 (P-value)
Log Fold Change
f
Top HALLMARK Pathways UP in
CD23-Rock1 Activated B cells
HEME_METABOLISM
MITOTIC_SPINDLE
COAGULATION
HEDGEHOG_SIGNALING
EPITHELIAL_MESENCHYMAL_TRANSITION
KRAS_SIGNALING_UP
ESTROGEN_RESPONSE_EARLY
MYOGENESIS
UV_RESPONSE_DN
ANGIOGENESIS
ESTROGEN_RESPONSE_LATE
KRAS_SIGNALING_DN
G2M_CHECKPOINT
-log10(FDR q-value)
g
GOBP-
Neuroinflammatory response
CD23-Rock1
Activated B
NES = 1.82
FDR q = 0.034
HALLMARK-Heme
metabolism
CD23-Rock1
Activated B
NES = 2.18
FDR q = <0.0001
HALLMARK-Mitotic
spindle
CD23-Rock1
Activated B
NES = 1.82
FDR q = 0.004
h
HALLMARK-Oxidative
phosphorylation
CD23-Rock1
Activated B
NES = -2.02
FDR q = 0.004
REACTOME-
Translation elongation
CD23-Rock1
Activated B
NES = -2.46
FDR q = <0.0001
i
WT vs CD23-Rock1
PB/PCs
DOWN in
CD23-Rock1
(95)
UP in
CD23-Rock1
(52)
Ubec2
Plk1
Tha1
Kyat1
Tpx2
Ackr2
-log10 (P-value)
Log Fold Change
j
Top HALLMARK Pathways UP in
CD23-Rock1 PB/PC
E2F_TARGETS
G2M_CHECKPOINT
MITOTIC_SPINDLE
-log10(FDR q-value)
k
HALLMARK-Mitotic
spindle
CD23-Rock1
PB/PC
NES = 1.64
FDR q = 0.026
l
REACTOME-
Translation elongation
CD23-Rock1
PB/PC
NES = -1.86
FDR q = 0.109

Suppl. Fig. 4

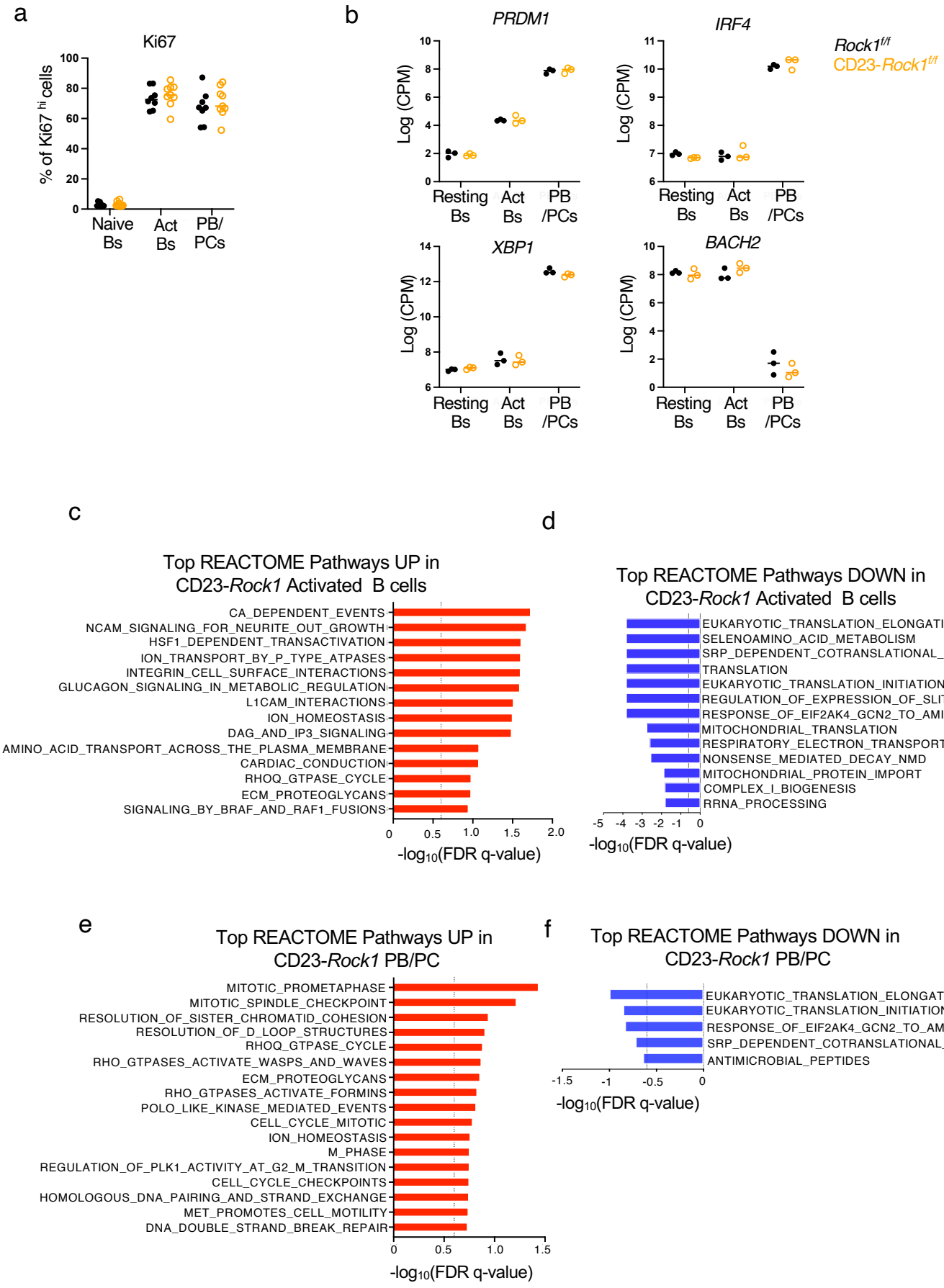
a
Ki67
% of Ki67 hi cells
Naive Bs
Act Bs
PB/ PCs
b
PRDM1
IRF4
XBP1
BACH2
Log (CPM)
Resting Bs
Act Bs
PB /PCs
Rock1f/f
CD23-Rock1f/f
c
Top REACTOME Pathways UP in CD23-Rock1 Activated B cells
CA_DEPENDENT_EVENTS
NCAM_SIGNALING_FOR_NEURITE_OUT_GROWTH
HSF1_DEPENDENT_TRANSACTIVATION
ION_TRANSPORT_BY_P_TYPE_ATPASES
INTEGRIN_CELL_SURFACE_INTERACTIONS
GLUCAGON_SIGNALING_IN_METABOLIC_REGULATION
L1CAM_INTERACTIONS
ION_HOMEOSTASIS
DAG_AND_IP3_SIGNALING
AMINO_ACID_TRANSPORT_ACROSS_THE_PLASMA_MEMBRANE
CARDIAC_CONDUCTION
RHOQ_GTPASE_CYCLE
ECM_PROTEOGLYCANS
SIGNALING_BY_BRAF_AND_RAF1_FUSIONS
-log10(FDR q-value)
d
Top REACTOME Pathways DOWN in CD23-Rock1 Activated B cells
EUKARYOTIC_TRANSLATION_ELONGATION
SELENOAMINO_ACID_METABOLISM
SRP_DEPENDENT_COTRANSLATIONAL_PROTEIN_TARGETING_TO
TRANSLATION
EUKARYOTIC_TRANSLATION_INITIATION
REGULATION_OF_EXPRESSION_OF_SLITS_AND_ROBOS
RESPONSE_OF_EIF2AK4_GCN2_TO_AMINO_ACID_DEFICIENCY
MITOCHONDRIAL_TRANSLATION
RESPIRATORY_ELECTRON_TRANSPORT
NONSENSE_MEDIATED_DECAY_NMD
MITOCHONDRIAL_PROTEIN_IMPORT
COMPLEX_I_BIOGENESIS
RRNA_PROCESSING
-log10(FDR q-value)
e
Top REACTOME Pathways UP in CD23-Rock1 PB/PC
MITOTIC_PROMETAPHASE
MITOTIC_SPINDLE_CHECKPOINT
RESOLUTION_OF_SISTER_CHROMATID_COHESION
RESOLUTION_OF_D_LOOP_STRUCTURES
RHOQ_GTPASE_CYCLE
RHO_GTPASES_ACTIVATE_WASPS_AND_WAVES
ECM_PROTEOGLYCANS
RHO_GTPASES_ACTIVATE_FORMINS
POLO_LIKE_KINASE_MEDIATED_EVENTS
CELL_CYCLE_MITOTIC
ION_HOMEOSTASIS
M_PHASE
REGULATION_OF_PLK1_ACTIVITY_AT_G2_M_TRANSITION
CELL_CYCLE_CHECKPOINTS
HOMOLOGOUS_DNA_PAIRING_AND_STRAND_EXCHANGE
MET_PROMOTES_CELL_MOTILITY
DNA_DOUBLE_STRAND_BREAK_REPAIR
-log10(FDR q-value)
f
Top REACTOME Pathways DOWN in CD23-Rock1 PB/PC
EUKARYOTIC_TRANSLATION_ELONGATION
EUKARYOTIC_TRANSLATION_INITIATION
RESPONSE_OF_EIF2AK4_GCN2_TO_AMINO_ACID_DEFICIENCY
SRP_DEPENDENT_COTRANSLATIONAL_PROTEIN_TARGETING_TC
ANTIMICROBIAL_PEPTIDES
-log10(FDR q-value)

Figure 4. Rock1 controls the transcriptional program of B-cells during malaria infection. Splenic B cell populations were sorted from WT or CD23-*Rock1* mice at Day 9 pi with 10^6 *Plasmodium yoelii* 17XNL-infected erythrocytes and subjected to bulk RNA-Seq analysis. (A) Gating strategy for sorting splenic B cell populations (Naive B cells, IgD^+CD138^-; activated B cells, IgD^-CD138^- and PB/PCs, IgD^-CD138^+) from Day 9 pi. (B, E, I) Volcano plot shows the genes differentially expressed (unadjusted $P < 0.01$, Log Fold change > 0.58) between WT and CD23-*Rock1* Naive B cells (B), activated B cells (E), and PB/PCs (I). (C, F and J) Plot shows the top enriched HALLMARK pathways upregulated in CD23-Rock1 compared with WT for naïve B cells (C), activated B cells (F) and PB/PCs (J). Dotted line indicates significance cutoff at FDR Q = 0.25. (D, G, H, K, L) GSEA enrichment plots representing significantly upregulated or downregulated pathways in CD23-*Rock1* Naive B cells (D), Activated B cells (G-H) and PB/PCs (K-L).

Supplementary Figure 4. (A) Plots showing quantification of the percentage of $Ki67^{hi}$ cells as assessed by flow cytometry in WT (black) and CD23-*Rock1* (orange) mice Day 9 pi. (B) Plots showing the normalized log-transformed counts per millions for the indicated genes from the RNA-seq analysis in Figure 4. (C-F) Plots show the top enriched up and down pathways from REACTOME in CD23-*Rock1* activated B cells (C-D) and PB/PCs (E-F) by GSEA (FDR Q = 0.25)

Figure 5

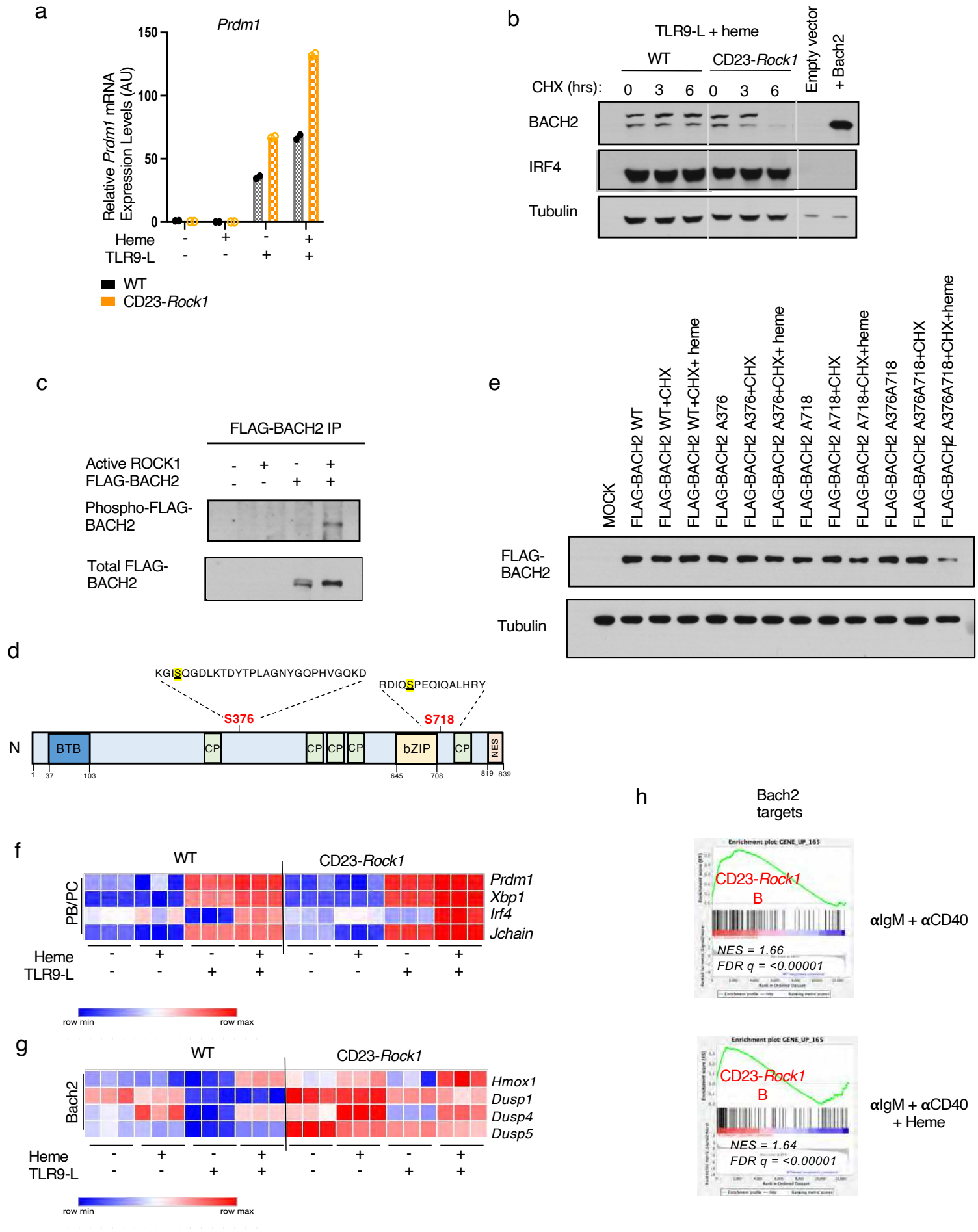
a
Prdm1
Relative Prdm1 mRNA Expression Levels (AU)
150
100
50
0
Heme
TLR9-L
WT
CD23-Rock1
b
TLR9-L + heme
WT
CD23-Rock1
CHX (hrs):
0 3 6 0 3 6
Empty vector
+ Bach2
BACH2
IRF4
Tubulin
c
FLAG-BACH2 IP
Active ROCK1
FLAG-BACH2
Phospho-FLAG-BACH2
Total FLAG-BACH2
d
KGISQGDLKTDYTPLAGNYGQPHVGQKD
RDIQSPEQIQALHRY
S376
S718
N
BTB
CP
bZIP
NES
1 37 103 645 708 819 839
e
MOCK
FLAG-BACH2 WT
FLAG-BACH2 WT+CHX
FLAG-BACH2 WT+CHX+ heme
FLAG-BACH2 A376
FLAG-BACH2 A376+CHX
FLAG-BACH2 A376+CHX+ heme
FLAG-BACH2 A718
FLAG-BACH2 A718+CHX
FLAG-BACH2 A718+CHX+heme
FLAG-BACH2 A376A718
FLAG-BACH2 A376A718+CHX
FLAG-BACH2 A376A718+CHX+heme
FLAG-BACH2
Tubulin
f
WT
CD23-Rock1
PB/PC
Prdm1
Xbp1
Irf4
Jchain
Heme
TLR9-L
row min
row max
g
WT
CD23-Rock1
Bach2
Hmox1
Dusp1
Dusp4
Dusp5
Heme
TLR9-L
row min
row max
h
Bach2 targets
Enrichment plot: GENE_UP_165
CD23-Rock1
B
NES = 1.66
FDR q = <0.00001
αIgM + αCD40
Enrichment plot: GENE_UP_165
CD23-Rock1
B
NES = 1.64
FDR q = <0.00001
αIgM + αCD40 + Heme

Suppl. Fig. 5

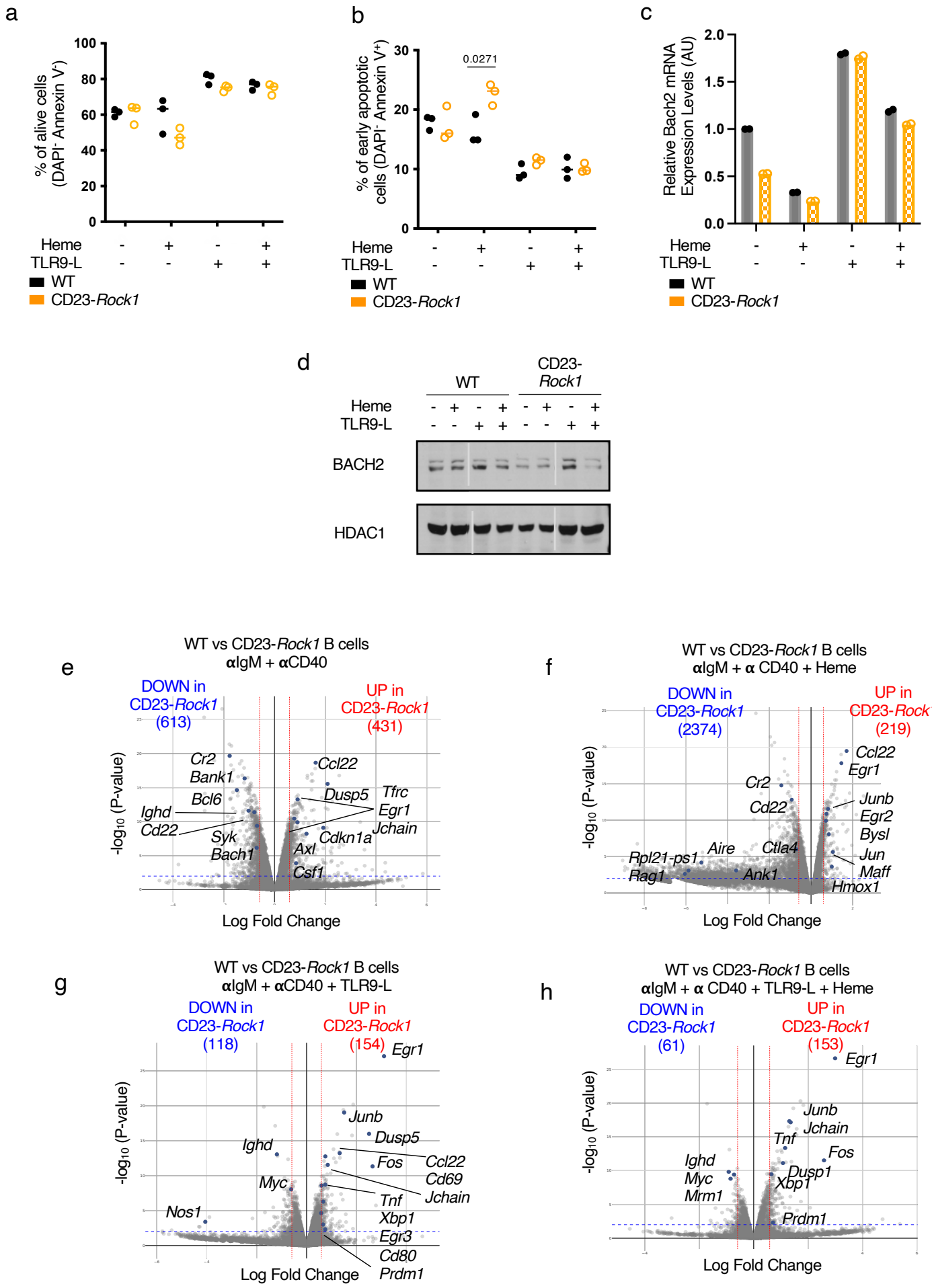
a
% of alive cells (DAPI- Annexin V-)
100
80
60
40
20
0
Heme - + - +
TLR9-L - - + +
WT
CD23-Rock1
b
% of early apoptotic cells (DAPI- Annexin V+)
30
20
10
0
0.0271
Heme - + - +
TLR9-L - - + +
WT
CD23-Rock1
c
Relative Bach2 mRNA Expression Levels (AU)
2.0
1.5
1.0
0.5
0.0
Heme - + - +
TLR9-L - - + +
WT
CD23-Rock1
d
WT
CD23-Rock1
Heme - + - + - + - +
TLR9-L - - + + - - + +
BACH2
HDAC1
e
WT vs CD23-Rock1 B cells
αIgM + αCD40
DOWN in CD23-Rock1 (613)
UP in CD23-Rock1 (431)
-log10 (P-value)
Log Fold Change
Cr2
Bank1
Bcl6
Ighd
Cd22
Syk
Bach1
Ccl22
Dusp5
Tfrc
Egr1
Jchain
Cdkn1a
Axl
Csf1
f
WT vs CD23-Rock1 B cells
αIgM + α CD40 + Heme
DOWN in CD23-Rock1 (2374)
UP in CD23-Rock1 (219)
-log10 (P-value)
Log Fold Change
Ccl22
Egr1
Cr2
Cd22
Junb
Egr2
Bysl
Jun
Maff
Hmox1
Aire
Ctla4
Rpl21-ps1
Rag1
Ank1
g
WT vs CD23-Rock1 B cells
αIgM + αCD40 + TLR9-L
DOWN in CD23-Rock1 (118)
UP in CD23-Rock1 (154)
-log10 (P-value)
Log Fold Change
Egr1
Junb
Dusp5
Ighd
Fos
Ccl22
Cd69
Myc
Jchain
Tnf
Nos1
Xbp1
Egr3
Cd80
Prdm1
h
WT vs CD23-Rock1 B cells
αIgM + α CD40 + TLR9-L + Heme
DOWN in CD23-Rock1 (61)
UP in CD23-Rock1 (153)
-log10 (P-value)
Log Fold Change
Egr1
Junb
Jchain
Tnf
Fos
Ighd
Dusp1
Myc
Xbp1
Mrm1
Prdm1

Figure 5. ROCK1 phosphorylates Bach2 and controls its stability and activity. Purified CD23$^+$ B cells from WT *(black)* and CD23-*Rock1 (orange)* mice were cultured with αIgM (5μg/mL) + αCD40 (5μg/mL), +/- combinations of a TLR9-L (1μg/ml) and Heme (60μM) as indicated for 3d. (A) Representative RT-qPCR showing *Prdm1* expression. Data representative of 3 independent experiments. (B) Representative immunoblot of BACH2 protein levels in the presence of Cycloheximide (CHX) added for 0, 3, or 6 hrs to the αIgM+αCD40+TLR9-L+heme conditions as indicated. (C) BACH2 was immunoprecipitated from 293T cells overexpressing FLAG-tagged BACH2 protein and incubated with recombinant constitutively active ROCK1 protein. Detection of phosphorylated BACH2 was performed by immunoblotting with an anti-phosphoserine antibody that recognizes a consensus site shared by ROCK1 and PKA. Reprobing with an anti-BACH2 Ab is shown in the bottom panel. Data are representative of 3 independent experiments. (D) Schematic diagram (adapted from https://mutagenetix.utsouthwestern.edu/phenotypic/phenotypic_rec.cfm?pk=3232) showing the location of the ROCK phosphorylation sites in the murine BACH2 protein, which were identified by Mass spectrometry. (E) 293T cells were transfected with constructs expressing FLAG-tagged wildtype BACH2 (WT) or mutants of BACH2 (S376A=A376, S718A=A718, or both S376A and S718A=A376A718). The transfectants were treated with or without Cycloheximide (CHX) +/- heme for 7 hrs at day two post transfection as indicated. (F) Heatmap shows the expression (log CPMs) of selected genes involved in PB/PC differentiation in WT and CD23-*Rock1* B cells stimulated *in vitro* as indicated. (G) Heatmap shows the expression (log CPMs) of selected Bach2 targets in WT and CD23-*Rock1* B cells stimulated *in vitro* as indicated. Colors are normalized per row meaning that the max value for each gene is plotted as red and the min as blue. (H) Gene-set enrichment analysis (GSEA) plots show the enrichment of Bach2 targets [31] in CD23-*Rock1* B cells stimulated as indicated.

Supplementary Figure 5. Purified CD23$^+$ B cells from WT *(black)* and CD23-*Rock1 (orange)* mice were cultured with αIgM (5μg/mL) + αCD40 (5μg/mL), +/- combinations of a TLR9-L (1μg/ml) and heme (60μM) as indicated for 3d. (A-B) Flow cytometry analysis of viable (Annexin V$^-$ PI$^-$) (A) or apoptotic (Annexin V$^+$ PI$^-$) cells (B). Data show mean +/- SEM; p-value by unpaired two-tailed t-tests with Welch's correction from 3 independent experiments. (C) Representative RT-qPCR showing *Bach2* expression. Data are representative of 3 independent experiments. (D) Representative immunoblot of BACH2 protein levels from 3 independent experiments. (E-H) Volcano plots shows the genes differentially expressed (unadjusted $P < 0.01$, Log Fold change > 0.58) between WT and CD23-*Rock1* in the αIgM+αCD40 (E), + heme (F), + TLR9-L (G), or + TLR9-L + heme (H) conditions.

Figure 6

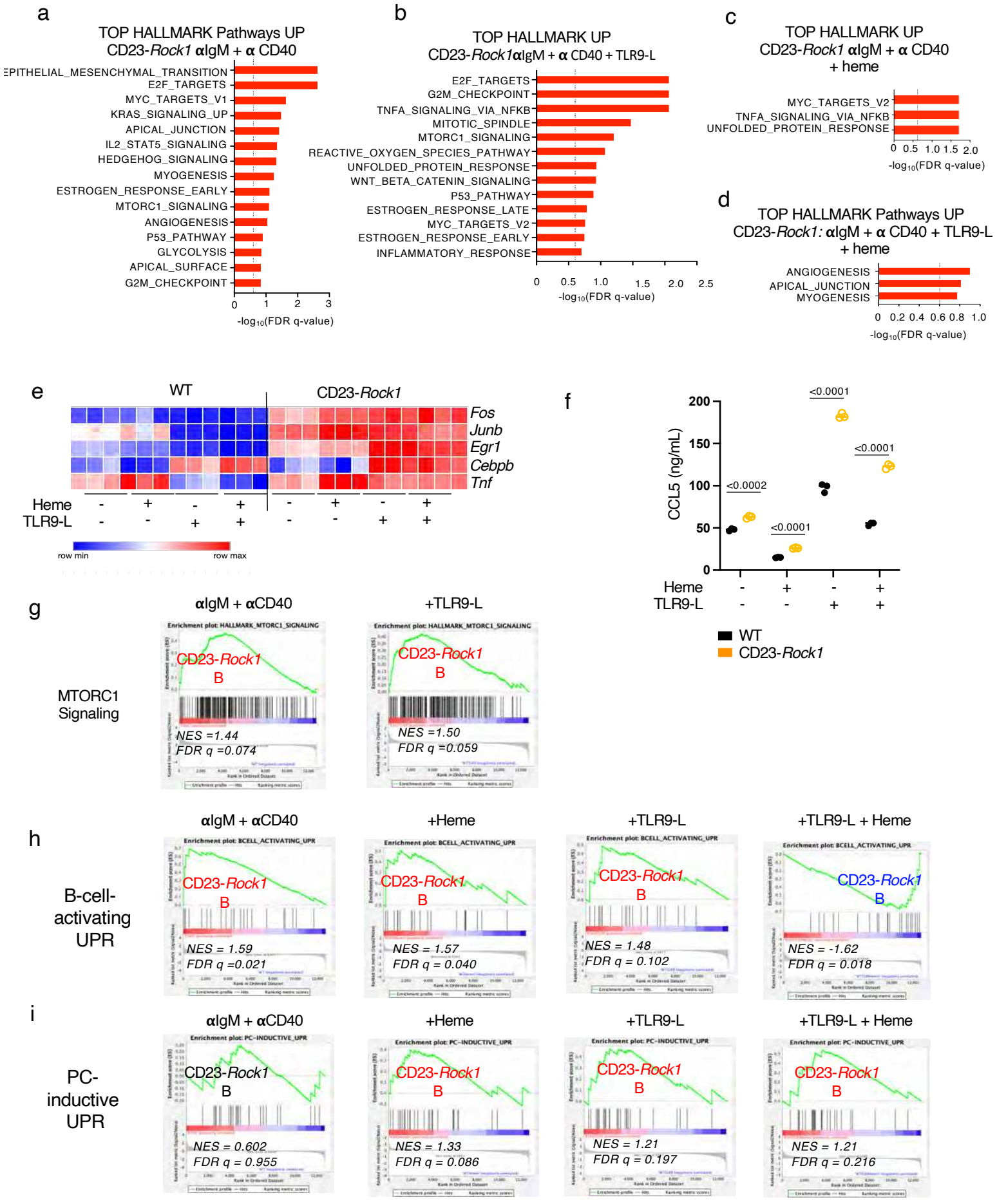
a
TOP HALLMARK Pathways UP
CD23-Rock1 αIgM + α CD40
EPITHELIAL_MESENCHYMAL_TRANSITION
E2F_TARGETS
MYC_TARGETS_V1
KRAS_SIGNALING_UP
APICAL_JUNCTION
IL2_STAT5_SIGNALING
HEDGEHOG_SIGNALING
MYOGENESIS
ESTROGEN_RESPONSE_EARLY
MTORC1_SIGNALING
ANGIOGENESIS
P53_PATHWAY
GLYCOLYSIS
APICAL_SURFACE
G2M_CHECKPOINT
0 1 2 3
-log10(FDR q-value)
b
TOP HALLMARK UP
CD23-Rock1αIgM + α CD40 + TLR9-L
E2F_TARGETS
G2M_CHECKPOINT
TNFA_SIGNALING_VIA_NFKB
MITOTIC_SPINDLE
MTORC1_SIGNALING
REACTIVE_OXYGEN_SPECIES_PATHWAY
UNFOLDED_PROTEIN_RESPONSE
WNT_BETA_CATENIN_SIGNALING
P53_PATHWAY
ESTROGEN_RESPONSE_LATE
MYC_TARGETS_V2
ESTROGEN_RESPONSE_EARLY
INFLAMMATORY_RESPONSE
0 0.5 1.0 1.5 2.0 2.5
-log10(FDR q-value)
c
TOP HALLMARK UP
CD23-Rock1 αIgM + α CD40
+ heme
MYC_TARGETS_V2
TNFA_SIGNALING_VIA_NFKB
UNFOLDED_PROTEIN_RESPONSE
0 0.5 1.0 1.5 2.0
-log10(FDR q-value)
d
TOP HALLMARK Pathways UP
CD23-Rock1: αIgM + α CD40 + TLR9-L
+ heme
ANGIOGENESIS
APICAL_JUNCTION
MYOGENESIS
0 0.2 0.4 0.6 0.8 1.0
-log10(FDR q-value)
e
WT
CD23-Rock1
Fos
Junb
Egr1
Cebpb
Tnf
Heme - + - + - + - +
TLR9-L - - + + - - + +
row min
row max
f
CCL5 (ng/mL)
200
150
100
50
0
<0.0001
<0.0001
<0.0002
<0.0001
Heme - + - +
TLR9-L - - + +
WT
CD23-Rock1
g
αIgM + αCD40
+TLR9-L
MTORC1 Signaling
Enrichment plot: HALLMARK_MTORC1_SIGNALING
CD23-Rock1
B
NES =1.44
FDR q =0.074
NES =1.50
FDR q =0.059
h
αIgM + αCD40
+Heme
+TLR9-L
+TLR9-L + Heme
B-cell-activating UPR
Enrichment plot: BCELL_ACTIVATING_UPR
CD23-Rock1
B
NES = 1.59
FDR q =0.021
NES = 1.57
FDR q = 0.040
NES = 1.48
FDR q = 0.102
NES = -1.62
FDR q = 0.018
i
αIgM + αCD40
+Heme
+TLR9-L
+TLR9-L + Heme
PC-inductive UPR
Enrichment plot: PC-INDUCTIVE_UPR
CD23-Rock1
B
NES = 0.602
FDR q = 0.955
NES = 1.33
FDR q = 0.086
NES = 1.21
FDR q = 0.197
NES = 1.21
FDR q = 0.216

Suppl. Fig. 6

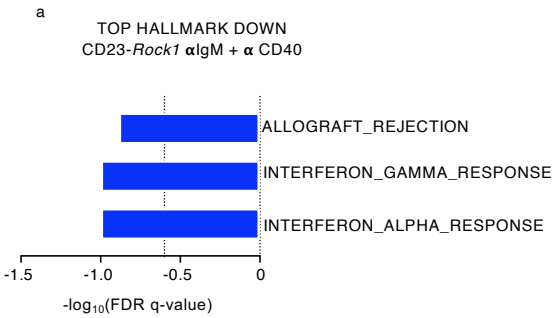
a
TOP HALLMARK DOWN
CD23-*Rock1* αIgM + α CD40
ALLOGRAFT_REJECTION
INTERFERON_GAMMA_RESPONSE
INTERFERON_ALPHA_RESPONSE
-1.5
-1.0
-0.5
0
-log10(FDR q-value)

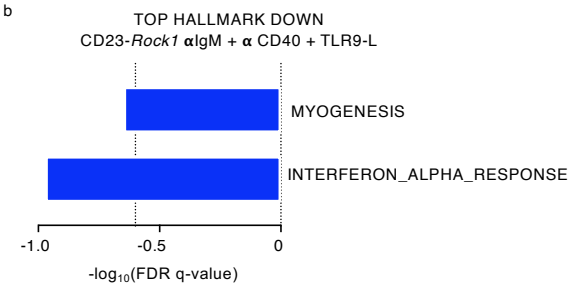
b
TOP HALLMARK DOWN
CD23-*Rock1* αIgM + α CD40 + TLR9-L
MYOGENESIS
INTERFERON_ALPHA_RESPONSE
-1.0
-0.5
0
-log10(FDR q-value)

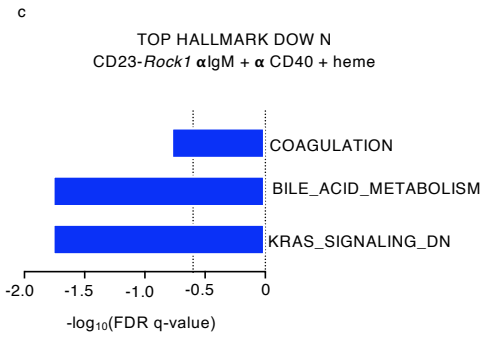
c
TOP HALLMARK DOW N
CD23-*Rock1* αIgM + α CD40 + heme
COAGULATION
BILE_ACID_METABOLISM
KRAS_SIGNALING_DN
-2.0
-1.5
-1.0
-0.5
0
-log10(FDR q-value)

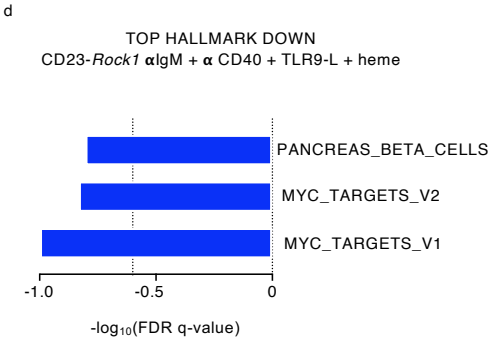
d
TOP HALLMARK DOWN
CD23-*Rock1* αIgM + α CD40 + TLR9-L + heme
PANCREAS_BETA_CELLS
MYC_TARGETS_V2
MYC_TARGETS_V1
-1.0
-0.5
0
-log10(FDR q-value)

Figure 6. *In vitro* activated B cells lacking ROCK1 exhibit an increased proinflammatory profile and dysregulated mTORC1-related signatures. Purified CD23^{+} B cells from WT and CD23-*Rock1* mice were cultured with αIgM (5μg/mL) + αCD40 (5μg/mL), +/- combinations of a TLR9-L (1μg/ml) and heme (60μM) as indicated for 3d. (A-D) Plot shows top enriched HALLMARK pathways upregulated in CD23-Rock1 B cells compared with WT B cells under the indicated stimulatory conditions. Dotted line indicates significance cutoff at FDR Q = 0.25. (E) Heatmap shows the expression (log CPMs) of selected genes involved in inflammation in WT and CD23-*Rock1* B cells stimulated *in vitro* as indicated. Colors are normalized per row meaning that the max value for each gene is plotted as red and the min as blue. (F) CCL5 levels in the supernatants were assessed by ELISA. Data show mean +/- SEM; p-value by unpaired two-tailed t-tests with Welch's correction from 3 independent experiments. (G-I) Gene-set enrichment analysis (GSEA) plots show the enrichment of the HALLMARK_MTORC1_SIGNALING pathway (G), B-cell activating UPR (H), or PC-inductive UPR (I) gene sets [13] in CD23-*Rock1* B cells stimulated as indicated. Significant upregulated enrichment is depicted in red, downregulated enrichment in blue and unaffected in black.

Supplementary Figure 6. Purified CD23^{+} B cells from WT and CD23-*Rock1* mice were cultured with αIgM (5μg/mL) + αCD40 (5μg/mL), +/- combinations of a TLR9-L (1μg/ml) and heme (60μM) as indicated for 3d. (A-D) Plot shows enriched HALLMARK pathways downregulated in CD23-Rock1 B cells compared with WT B cells under the indicated stimulatory conditions. Dotted line indicates significance cutoff at FDR Q = 0.25.

Figure 7

a

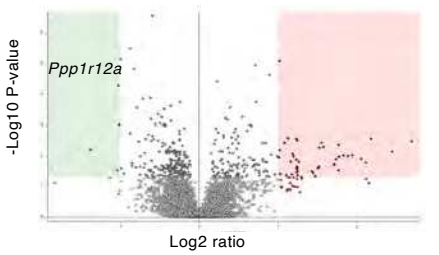

b

Symbol	Site	Fold change	P-value
Alpl	S110	-1.38	0.006277
Akap13	S1503, S856	-1.04	0.029862
Ppp1r12a	S861, S870	-1.02	5.34E-05
Ppp1r12c	S411	-1.01	0.000971

c

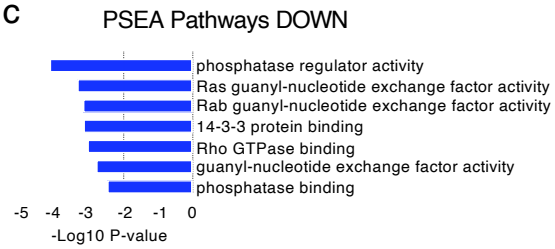

d

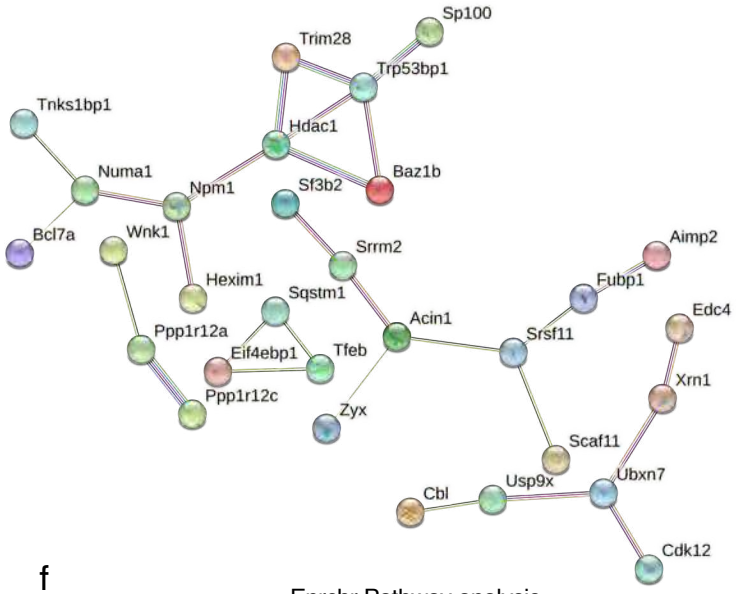

e

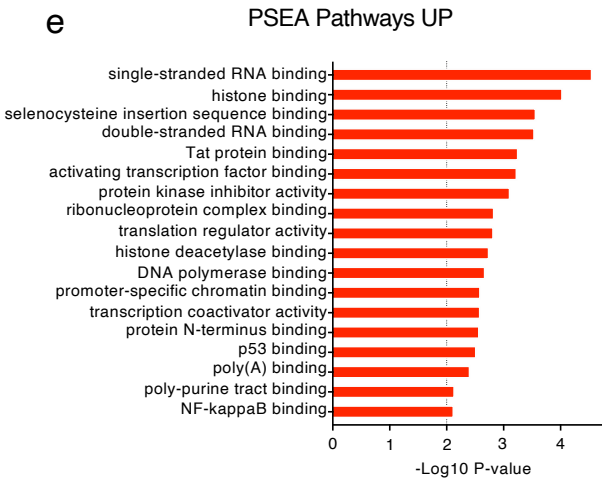

f

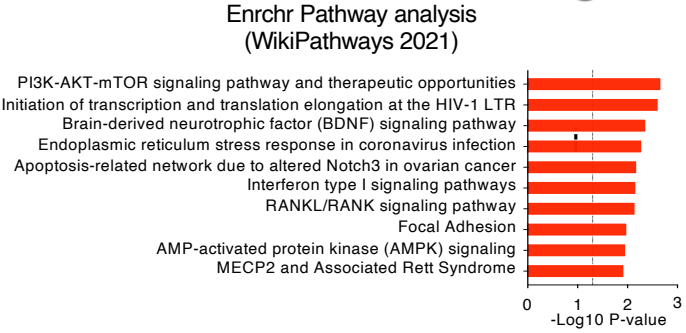

g

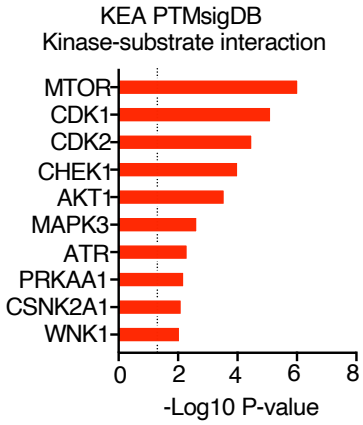

h

mTORC1, RIPK3, TBK1, PLK1	Hdac1 Npm1
mTORC1, RIPK3, TBK1	Sqstm1 Trp53bp1
mTORC1, RIPK3, PLK1	Map4
mTORC1, RIPK3	Akap13 Hexim1 Ubxn7
mTORC1, TBK1	Med19
mTORC1, PLK1	Marcksl1
RIPK3	Crtc2 Son
PLK1	Baz1b

Suppl. Fig. 7

a

Symbol	Modulate site	Fold change	P-value
Ubap2l	S467, S477	1.01	0.011351
Trp53bp1	S298 and S303, S1115	1.01,2.11	8.28E-06, 0.016504
Rassf4	S169, S170	1.02	0.006518
Med19	S226	1.03	0.038293
Baz1b	S345	1.08	0.003771
Son	S319, T320	1.11	0.042263
Usp9x	S590	1.12	0.002624
Sqstm1	S334	1.16	0.015204
Selplg	?	1.18	0.040502
Aimp2	T82	1.19	0.00858
Ubxn7	S395	1.2	0.010171
Numa1	T633	1.23	0.002771
Rplp2	S105	1.23	0.013314
Trim28	Y458	1.24	0.026169
Wnk1	?	1.24	0.003187
Npm1	S70	1.24	0.022411
Scaf11	S752, S755	1.24	0.023313
Cdk12	?	1.24	0.03181
Eif4ebp1	?	1.24	0.03453
Edc4	S773	1.25	0.043652
Hexim1	S103	1.26	0.015491
Map4	S475	1.44	0.036135
Marcksl1	S132, S135	1.47	0.046669
Hdac1	S393	1.51	0.025136
Borcs6	S130	1.52	0.022699
Bcl7a	S157	1.52	0.00537
Acin1	S400	1.55	0.003694
Crtc2	S461, T463	1.57	0.005177
Tfeb	T330	1.77	0.010759
Zyx	S144	1.77	0.004352
Mbp	S112	1.83	0.009694
Fubp1	S629	1.89	0.00997
Srrm2	S1315	1.94	0.009465
Son	S256	2.05	0.012638
Tnks1bp1	S1063	2.18	0.002799
Cast	S290	2.45	0.007393

b

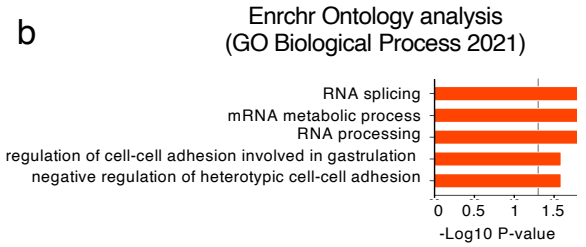

c

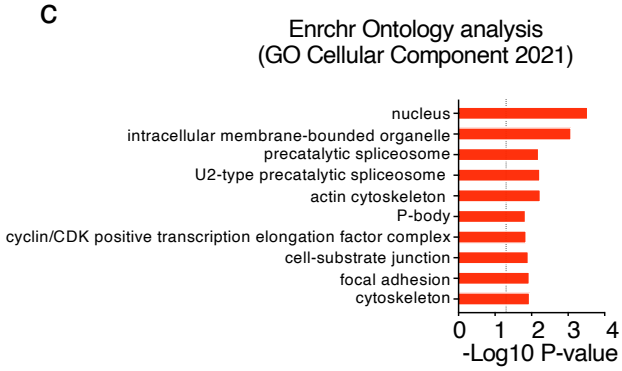

d

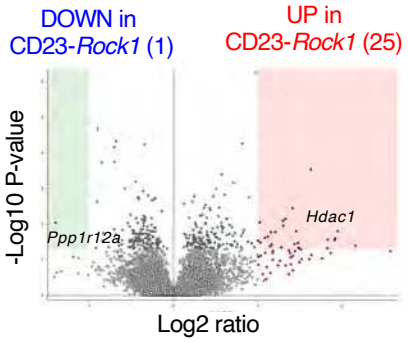

e

Symbol	Site	Fold change	P-value
Xrn1	S1668	1	0.02881467
Srsf11	S499	1.02	0.00880385
Cbl	T613	1.08	0.02368171
Sp100	S190	1.28	0.04449481
Sf3b2	S761	1.48	0.04601716
Cad	T1770	1.91	0.02757363

Figure 7. B-cell ROCK1 controls a unique phosphoproteomic profile. Purified $CD23^+$ B cells from WT and CD23-*Rock1* mice were cultured with αIgM (5μg/mL) + αCD40 (5μg/mL) for 3 d. and submitted for phosphoproteomic analysis using TMT mass spectrometry. (A) Volcano plot shows differentially enriched phosphoproteins in stimulated WT (green square) and CD23-*Rock1* (red square) B cells. Log2FC>1, P <0.05 (B) Table summarizing the key residues whose phosphorylation was significantly downregulated (log2FC>1, P <0.05) in stimulated CD23-*Rock1* compared to WT B cells. (C) Protein Set Enrichment Analysis (PSEA) (P < 0.01) of the phosphoproteins downregulated in stimulated CD23-*Rock1* versus WT B cells based on Gene Ontology (GO) database. (D) STRING analysis of phosphoproteomic targets (https://string-db.org/). (E) Protein Set Enrichment Analysis (PSEA) (P < 0.01) of the phosphoproteins upregulated in stimulated CD23-*Rock1* versus WT B cells based on Gene Ontology (GO) database. (F) Top pathways obtained from the Enrichr Pathway Analysis of the differentially enriched phosphoproteins from stimulated CD23-*Rock1* versus WT B cells (P < 0.05). (G) Top Kinase-substrate interactions from the Kinase enrichment analysis (KEA) of the differentially enriched phosphoproteins from stimulated CD23-*Rock1* versus WT B cells (P < 0.05) (H) Summary of selected proteins whose phosphorylation was upregulated in stimulated CD23-*Rock1* versus WT B cells at sites that are also potential targets of mTOR, RIPK3, PLK1, and TBK1 based on annotated references from PhosphositePlus.

Supplementary Figure 7. (A) Table summarizing the key residues whose phosphorylation was significantly upregulated (log2FC>1, P <0.05) in CD23-*Rock1* as compared to WT B cells stimulated with αIgM+αCD40. (B-C) Top pathways obtained from the Enrichr Ontology analysis of the differentially enriched phosphoproteins from CD23-*Rock1* versus WT B cells stimulated with αIgM+αCD40 using either GO Biological Process 2021 (B) or GO Cellular Component (C) databases (P < 0.05). (D) Volcano plot shows differentially enriched phosphoproteins in WT (green square) and CD23-*Rock1* (red square) B cells stimulated with αIgM+αCD40+TLR9-L (1μg/ml) for 3d. (E) Table summarizing the key residues whose phosphorylation was significantly upregulated (log2FC>1, P <0.05) in CD23-*Rock1* as compared to WT B cells stimulated with αIgM+αCD40 only in the presence of a TLR9 ligand.

FIGURE 8

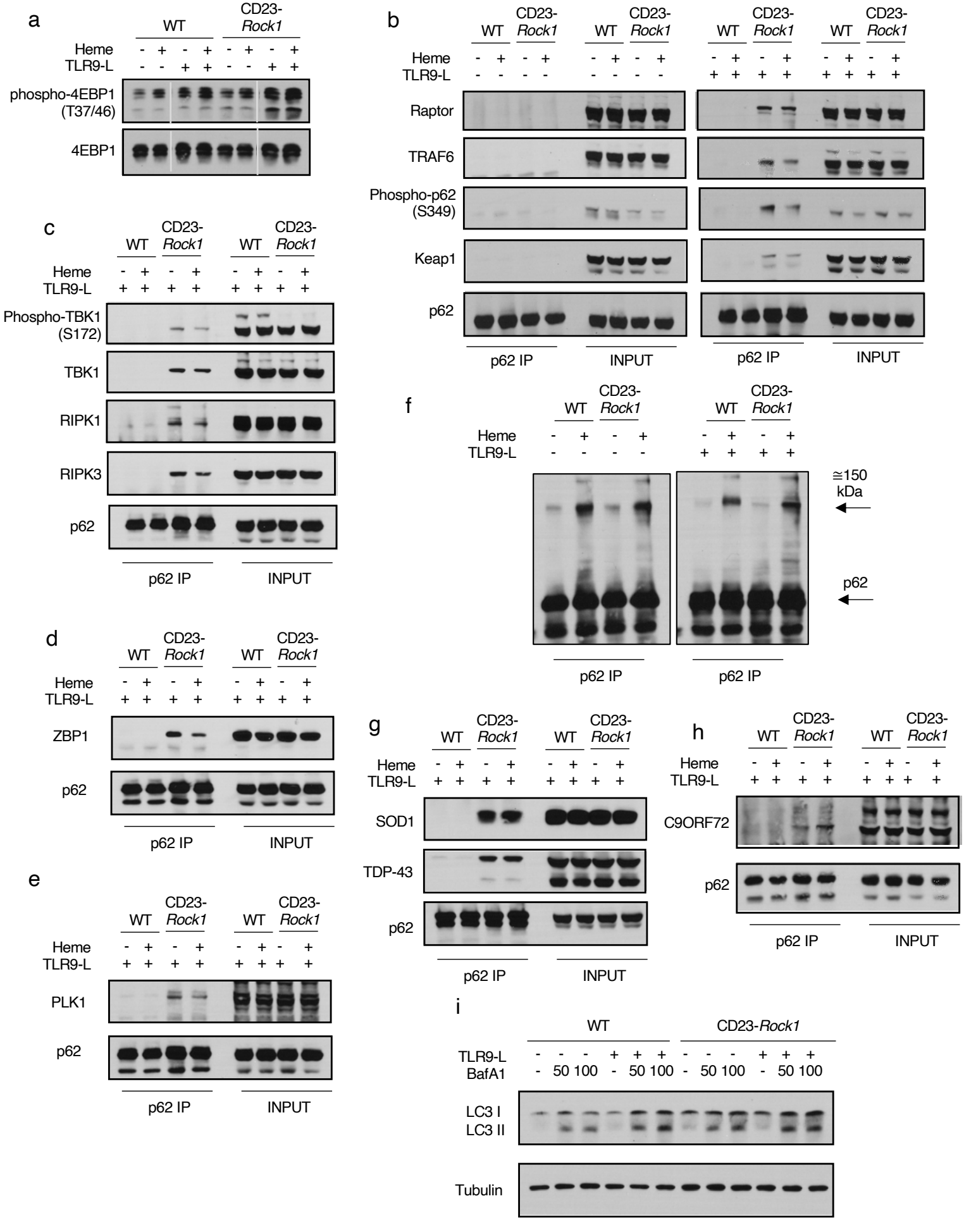
a
WT
CD23-Rock1
Heme
TLR9-L
phospho-4EBP1 (T37/46)
4EBP1
b
Raptor
TRAF6
Phospho-p62 (S349)
Keap1
p62
p62 IP
INPUT
c
Phospho-TBK1 (S172)
TBK1
RIPK1
RIPK3
p62
d
ZBP1
e
PLK1
f
≅150 kDa
g
SOD1
TDP-43
h
C9ORF72
i
BafA1
LC3 I
LC3 II
Tubulin

Suppl Figure 8

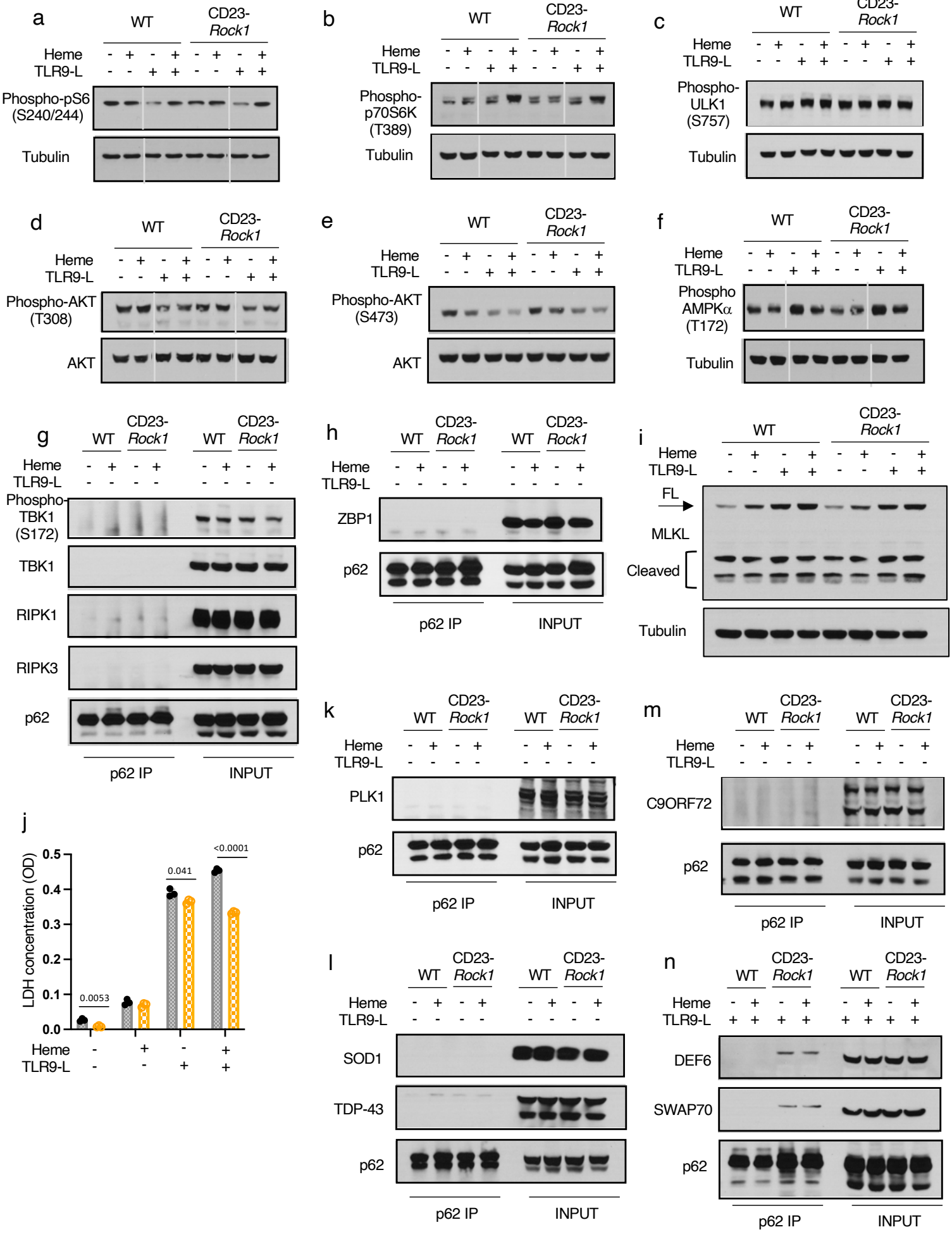

Figure 8. ROCK1 limits the assembly of p62 complexes enriched in mTORC1, PLK1, TBK1, RhIM-domain proteins, and ALS-linked molecules. Purified $CD23^+$ B cells from WT and CD23-*Rock1* mice were cultured with αIgM (5μg/mL) + αCD40 (5μg/mL), +/- combinations of a TLR9-L (1μg/ml) and heme (60μM) as indicated for 3d. (A) Western blotting analysis of the levels of phospho-4EBP1 in cytoplasmic extracts from WT and CD23-*Rock1* B cells stimulated as indicated. (B-G) p62 was immunoprecipitated from cytoplasmic extracts of WT or CD23-*Rock1* B cells stimulated as indicated. The precipitates were probed by Western blotting to assess p62 phosphorylation and the interaction of p62 with raptor, TRAF6, and Keap1 (B); p62 was immunoprecipitated from cytoplasmic extracts of WT or CD23-*Rock1* B cells stimulated as indicated. The immunoprecipitates were probed by Western blotting to assess for the presence of pTBK1, TBK1, RIPK1, and RIPK3 (C); ZBP1 (D); PLK1 (E); SOD1 and TDP-43 (G); and C9ORF72 (H). (F) Western blotting analysis of HMW p62 complexes in WT or CD23-*Rock1* B cells stimulated as indicated. (I) Western blots of LC3-I and LC3-II in extracts from WT and CD23-*Rock1* B cells. Cells were treated for 4 hours with DMSO or bafilomycin A1 (BafA1; 50 nM or 100 nM as indicated). Results are representative of at least 3 independent experiments.

Supplementary Fig. 8. Purified $CD23^+$ B cells from WT and CD23-*Rock1* mice were cultured with αIgM (5μg/mL) + αCD40 (5μg/mL), +/- combinations of a TLR9-L (1μg/ml) and heme (60μM) as indicated for 3d. (A-F) Western blotting analysis of the levels of p-S6 (A), p-70S6K (B), pULK1 (C), pAKT-T308 (D), pAKT-S473 (E), pAMPKα (F) in cytoplasmic extracts from WT and CD23-*Rock1* B cells stimulated as indicated. (G-K) p62 was immunoprecipitated from cytoplasmic extracts of WT or CD23-*Rock1* B cells stimulated as indicated. The immunoprecipitates were probed by Western blotting for the presence of pTBK1, TBK1, RIPK1, and RIPK3 (G); ZBP1 (H); PLK1 (K); (I) Western blotting analysis of FL and cleaved MLKL in cytoplasmic extracts from WT and CD23-*Rock1* B cells stimulated as indicated. (J) LDH levels in the supernatants of WT and CD23-*Rock1* B cells stimulated as indicated as assessed by ELISA. (L-N) p62 was immunoprecipitated from cytoplasmic extracts of WT or CD23-*Rock1* B cells stimulated as indicated. The immunoprecipitates were probed by Western blotting for the presence of SOD1 (L), TDP-43 (L), C9ORF72 (M), DEF6 (N), and SWAP-70 (N).

Figure 9

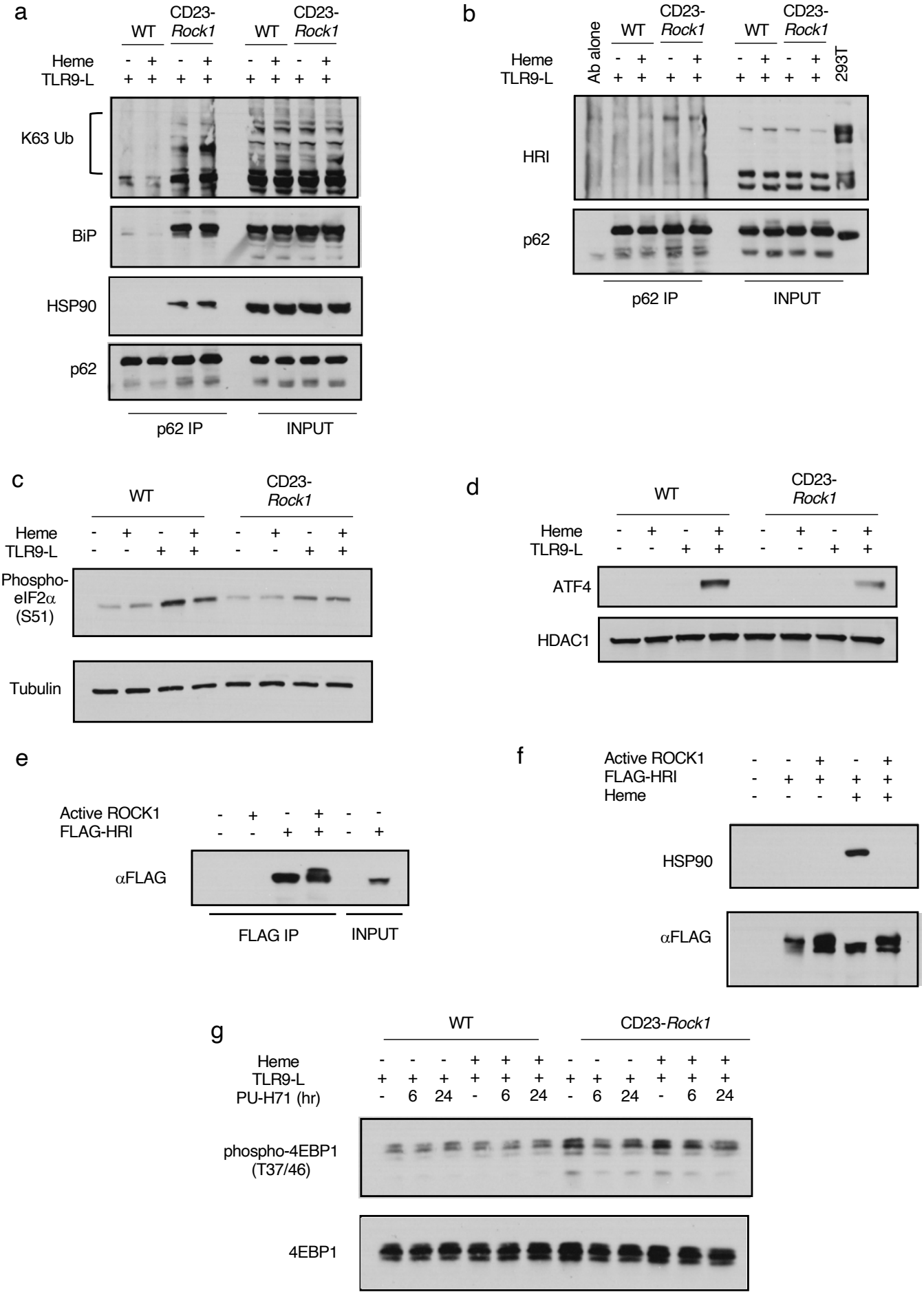
a
WT
CD23-Rock1
WT
CD23-Rock1
Heme
TLR9-L
K63 Ub
BiP
HSP90
p62
p62 IP
INPUT
b
Ab alone
WT
CD23-Rock1
WT
CD23-Rock1
293T
Heme
TLR9-L
HRI
p62
p62 IP
INPUT
c
WT
CD23-Rock1
Heme
TLR9-L
Phospho-eIF2α (S51)
Tubulin
d
WT
CD23-Rock1
Heme
TLR9-L
ATF4
HDAC1
e
Active ROCK1
FLAG-HRI
αFLAG
FLAG IP
INPUT
f
Active ROCK1
FLAG-HRI
Heme
HSP90
αFLAG
g
WT
CD23-Rock1
Heme
TLR9-L
PU-H71 (hr)
phospho-4EBP1 (T37/46)
4EBP1

Suppl Fig. 9

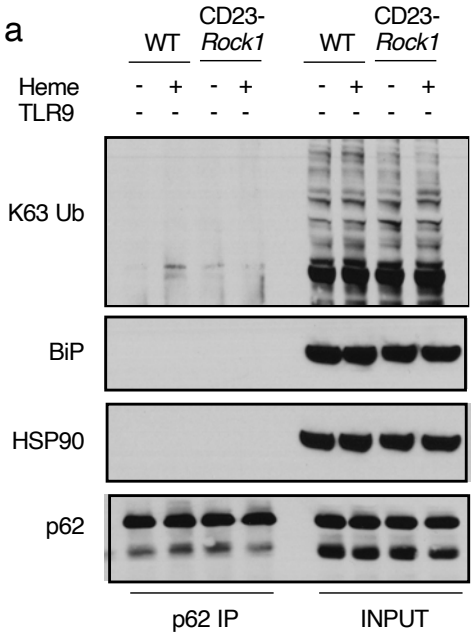
a
WT
CD23-Rock1
WT
CD23-Rock1
Heme
TLR9
- + - + - + - +
- - - - - - - -
K63 Ub
BiP
HSP90
p62
p62 IP
INPUT

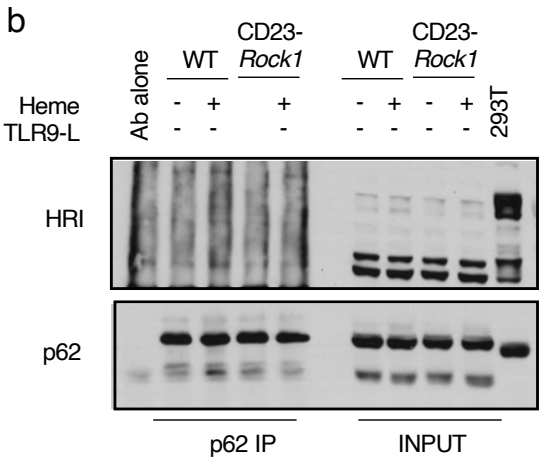
b
Ab alone
WT
CD23-Rock1
WT
CD23-Rock1
293T
Heme
TLR9-L
HRI
p62
p62 IP
INPUT

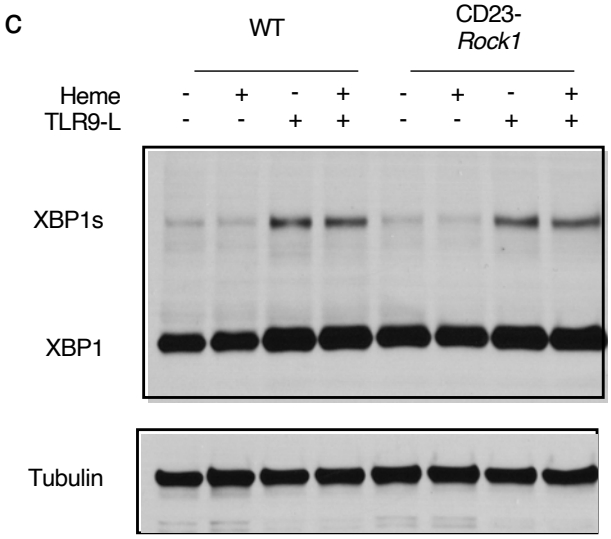
c
WT
CD23-Rock1
Heme
TLR9-L
XBP1s
XBP1
Tubulin

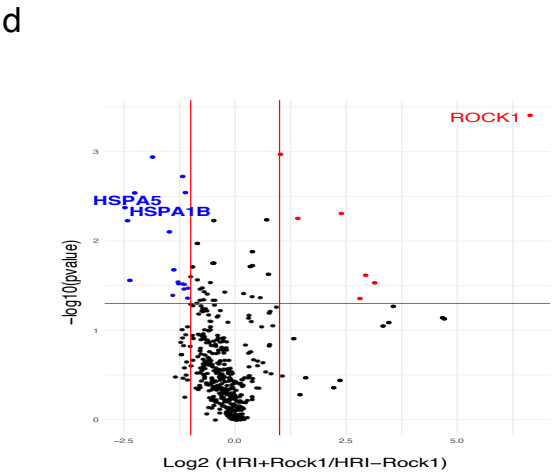
d
ROCK1
HSPA5
HSPA1B
-log10(pvalue)
Log2 (HRI+Rock1/HRI−Rock1)

Figure 9. ROCK1 regulates the heme-regulated inhibitor, HRI. Purified CD23$^+$ B cells from WT and CD23-*Rock1* mice were cultured with αIgM (5μg/mL) + αCD40 (5μg/mL), +/- combinations of a TLR9-L (1μg/ml) and heme (60μM) as indicated for 3d. (A-B) p62 was immunoprecipitated from cytoplasmic extracts of WT or CD23-*Rock1* B cells stimulated as indicated. The immunoprecipitates were probed by Western blotting to assess for the presence of K63-ubiquitinated proteins, BiP, HSP90 (A), and HRI (B). (C-D) Western blotting analysis of the levels of pEIF2α (C) and ATF4 (D) in extracts from WT and CD23-*Rock1* B cells stimulated as indicated. Results are representative of at least 3 independent experiments. (E) Flag-tagged HRI was immunoprecipitated from 293T cells and incubated with constitutively active ROCK1 followed by immunoblotting with an anti-Flag antibody. Results are representative of 3 independent experiments. (F) Flag-tagged HRI was immunoprecipitated from 293T cells stimulated in the presence or absence of heme (60μM for 4 hrs) and incubated with constitutively active ROCK1 followed by immunoblotting with an anti-HSP90 Ab (upper panel) or anti-Flag antibody (lower panel). Results are representative of 3 independent experiments. (G) Western blots of phospho-4EBP1 levels in cytoplasmic extracts from WT and CD23-*Rock1* B cells stimulated in the presence of DMSO or PU-H71 (1μM) for either 6 or 24 hrs as indicated.

Supplementary Fig. 9. Purified CD23$^+$ B cells from WT and CD23-*Rock1* mice were cultured with αIgM (5μg/mL) + αCD40 (5μg/mL), +/- combinations of a TLR9-L (1μg/ml) and heme (60μM) as indicated for 3d. (A-B) p62 was immunoprecipitated from cytoplasmic extracts of WT or CD23-*Rock1* B cells stimulated as indicated. The immunoprecipitates were probed by Western blotting for the presence of K63-ubiquitinated proteins, BiP, HSP90 (A), and HRI (B). (C) Western blotting analysis of the levels of total XBP1 and spliced XBP1 (XBP1s) in cytoplasmic extracts from WT and CD23-*Rock1* B cells stimulated as indicated. Results are representative of at least 3 independent experiments. (D) Volcano plot shows differentially enriched proteins interacting with immunoprecipitated FLAG-tagged HRI in the presence or absence of CA-ROCK1 as assessed by TMT mass spectrometry.